Low-Cost Technologies for Flexible Endoscopy

Design, Control and Autonomy for a Water-Jet Actuated Soft Continuum Endoscope

Simone Calò

Submitted in accordance with the requirements for the degree of

Doctor of Philosophy

in

Electronic and Electrical Engineering

The University of Leeds

School of Electronic and Electrical Engineering
STORM Lab

March, 2021

Leeds, United Kingdom

The candidate confirms that the work submitted is his/her own and that appropriate credit has been given where reference has been made to the work of others.

Acronyms

AER Automated Endoscope Reprocessor.

AI Artificial Intelligence.

CM Continuum Manipulator.

DoF Degree of Freedom.

ECV Eccentric Compression Valve.

EM Electro-Magnetic.

FE Flexible Endoscopy (or Endoscope).

FF Feed-Forward.

FK Forward Kinematics.

FN False Negative.

FoV Field of View.

FP False Positive.

GE Gastro Enterologist.

GI Gastro-Intestinal.

GUI Graphical User Interface.

HJ HydroJet.

IMU Inertial Measurement Unit.

LMIC Low- and Middle-Income Countries.

MIS Minimally Invasive Surgery.

NBI Narrow Band Imaging.

PRM Probabilistic Road Map.

ROS Robot Operating System.

RRT Rapidly-Exploring Random Trees.

SLA StereoLithography Apparatus.

SLAM Simultaneous Localization and Mapping.

SMA Shape Memory Alloy.

TFA Tip Follower Actuation.

TP True Positive.

UGI Upper GI.

Contents

List of Figures

List of Tables

Introduction

Motivation

Despite the outstanding diagnostic performance brought by new technologies in medicine, cancer remains a significant burden worldwide. In addition to prevention strategies, the ability to detect malignancy early is crucial in enabling effective treatment and dramatically increasing the survival rate of patients. In the case of gastric cancer, diagnosis is generally performed using Flexible Endoscopy (or Endoscope) (FE). The FE has been proven to be a powerful, reliable and cost effective tool in the fight against gastric cancer. However, its effectiveness strongly depends on the skills of trained Gastro Enterologists (GE) who perform the procedures. Moreover, accessibility and availability of such tools is often limited to people residing in major cities, while remote and rural areas remain poorly served by their health systems.

The advent of robotics in medicine offers a new solution to these problems. When possible, automating diagnostic procedures or surgical tasks has the potential to deliver reliable, repeatable and cost-effective alternatives to a standard human-in-the-loop procedures. Embedding autonomous capabilities into a machine, optimally designed to execute a specific task, could enable the device to automatically adapt to different conditions and non-skilled personnel to perform the procedure by supervising the actions of the robotic platform. In these scenarios, safety represents a major concern and in the majority of the cases a safe interaction between the robot and the tissues can be guaranteed by building compliant robots made of soft materials. However, if the possibility of using compliant devices offers a number of advantages to the final user or patient, it defines a series of technical challenges that have to be addressed to deliver a stable and reliable control of the platform. Finally, by adopting low-cost designs, single-use solutions can be realised to address the issue and complication of sterilisation.

This dissertation discusses the research effort targeted at the development of a low-cost, disposable gastroscopy platform to offer a safe, cost-effective, fault-

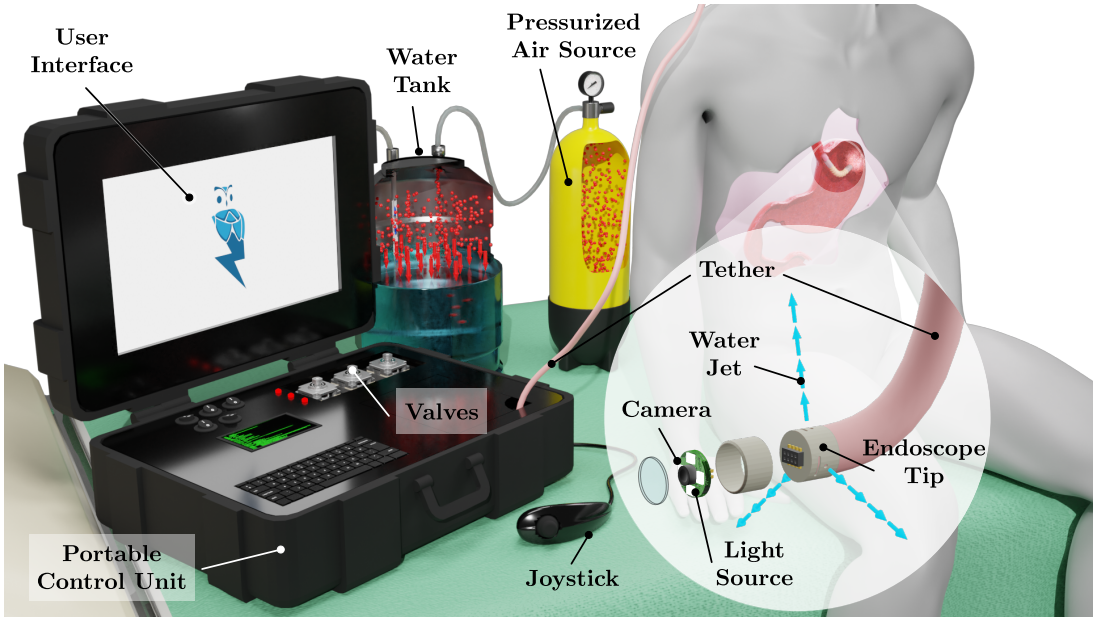

Figure 1: The HydroJet platform

free alternative to standard FE. The research focuses around a low-cost robotic FE platform called HydroJet (HJ), which is conceptualised in Figure 1. Here, the HJ endoscope is represented in action when deployed inside the stomach cavity. The HJ system is pump-less, relying only on a pressurized air tank and a water vessel. The endoscope of the HJ system uses the reaction force generated by the ejection of pressurized water to navigate the gastric cavity. Specifically, water is ejected from three nozzles placed around the capsule body at an even distance of 120°. The generated thrust, coupled with the low stiffness properties of the endoscope's tether, provides two Degree of Freedom (DoF) controllability of the endoscope tip and coverage of a 3D workspace.

To supply the GE (or the general user) with a visual feedback of the esophagus and stomach mucosa during the gastroscopy procedure, the HJ's tip is equipped with a miniaturized camera module and illumination unit. The entire HJ system is designed to take up a minimal amount of space, making it easy to transport and set up in remote areas otherwise unreachable with standard FE equipment. Moreover, the lack of a costly actuation system (e.g. the precisely aligned and tensioned Bowden cables in a traditional FE) allow the HJ to be, at the same time, reliable and cost-effective. In this way, all the indirect costs related to the endoscopic equipment (e.g. maintenance) and its use (e.g. sterilization) are cut by adopting a single-use device.

With the benefits outlined above, the HJ represents a strong candidate for employment in gastric cancer screening programmes. As a purely diagnostic tool, it would be used to visually identify suspicious lesions or abnormalities of the

stomach mucosa and identify for referral the patients in need of urgent medical attention or further inspection (e.g. biopsies).

Contributions

This section details the innovations in the field of water jet actuated soft continuum robots, as the result of the work carried out in collaboration with technical and clinical partners at the Mechanical Engineering Department at Vanderbilt University (STORM Lab US), University College London (UK) and Tianjin University (China).

The research presented in this dissertation inherits the development stages of the HJ platform described in [17] and further improved in [16]. With these designs, the tip of the endoscope can move in free space with two DoF thanks to reaction force produced by the water ejected from miniaturized nozzles. An additional degree of freedom can be added simply adjusting the length of the tether that is inside the stomach. Despite the inherited system demonstrating portability and manual controllability, two areas producing limitations were identified: (1) those associated with the endoscope design and (2) those associated with the external actuation valves and flow regulation.

Comparative trials were performed to evaluate the performance of the inherited HJ system with respect to standard FE. Results showed that the limited range of motion (less than 95 deg bending angle) of the device and the narrow camera Field of View (FoV) (up to 64°) did not allow for a complete retroflexion of the endoscope's tip, required to visualize key landmarks of the stomach mucosa. Therefore, a significant increase in the time needed to complete the inspection procedure was experienced when using the HJ.

The actuation system of the inherited device relied on three pinch valves to guarantee the separation between water and mechanical/electronic components of the system. The disadvantage of using these valves was evident after just a few actuation cycles, when the pinching action caused the plastic deformation of the soft tubing, in this way modifying the input/output characteristic of the valve.

At the development stages described in [16], the HJ was manoeuvred by individually controlling each valve in an open-loop fashion, and no advanced capabilities were presented in terms of automatic control, autonomous or semi-autonomous skills.

Table 1 summarizes the characteristics of the inherited HJ platform, while,

		Inherited HydroJet Platform	Target System Requirements
Design	Dimensions (rigid components)	Diameter: 10 mm Length: 29 mm	Diameter: 8 mm Length: 10 mm
	Workspace	Bending angle: 50° - 95° Camera FoV: 54° - 64° Overall: 77° - 127°	Overall: 180° (retroflexion)
	Portability	Proven in previous HJ versions	
	Actuation	Sanitary Flow-Rate Control Tube Damaging	Sanitary Flow-Rate Control Stable Input/Output Characteristic
Control	Manual Control	Independent valve control or Joystick	
	Automatic Control	None	Trajectory Tracking
Autonomy	Environmental Perception	None	Obstacle Detection
	Exploration	None	Full Stomach Inspection

Table 1: Comparison between the specification of the inherited HJ platform and the desired system requirements.

the contributions of this thesis aimed at improving the system's diagnostic capabilities are listed below.

- **Design**: in the case of the endoscope design, with the aim of widening the manipulator's workspace limits and improve the stability of the endoscope's tip at wide bending angles, the inherited design of the endoscope was advanced to a non-homogeneous stiffness tether. A softer section at the end of the tether was introduced and allowed to confine the deformations generated by the forces acting at the tip, to the distal part of the endoscope. In this way, smaller bending radii and wider bending angles were achieved. On the other hand, these stiffness reducing design modifications generated unwanted oscillatory behaviour of the endoscope's tip after a certain bending angle is reached. On this topic, a comprehensive study was carried out, involving the use of different materials for the soft section of the tether and the geometry of the water lines. The resulting device design allows the bending section of the endoscope to attain larger deformations (wider workspace) while guaranteeing stable positioning of the tip.

  For the external control valves, an extensive research effort has been dedicated in the attempt to optimize the state-of-the-art actuation system, in order to enable smooth and easy to control movements of the endoscope tip. This led to the development of novel flow-rate control apparatus, here-

after referred to as Eccentric Compression Valve (ECV). A first iteration of the valve design was evaluated, then it was fine tuned in order for the device to deliver a linear flow-rate output characteristic and oscillation-free movement of the endoscope. The valve was extensively tested both in standalone scenarios and within the HJ system set-up, to assess its ability to meet the minimum requirements and outperform the previous actuation systems.

Relevant Publications:

- Calò, Simone, James H. Chandler, Federico Campisano, Keith L. Obstein, and Pietro Valdastri. "A Compression Valve for Sanitary Control of Fluid-Driven Actuators." IEEE/ASME Transactions on Mechatronics 25, no. 2 (2019): 1005-1015.

Relevant Patent Application:

- S. Calò, P. Valdastri, J. H. Chandler, "VALVE", Patent Publication Number WO/-2020/065348, Priority Date 28 September 2018.

- **Control**: the ability to accurately and precisely control the position of the tip of the endoscope represents an essential foundation to enable the implementation of more autonomous behaviours. To comply with the inherent ability of the HJ tip to move on a sphere-like surface, a polar coordinate-based task-space control strategy was implemented. The controller only acts on the angular coordinates $[\varphi, \vartheta]$, referred to as the tip azimuth and elevation respectively, while the radial coordinate is fixed and depends on the length of the soft tether section. Furthermore, in spite of the valve's linear output characteristic, its hysteresis loop introduces excessive oscillations, unstable behaviours and delays in the movements of the endoscope's tip. To account for this, a hysteresis compensation module was added to the control system. This resulted in a time-to-completion of the task being drastically reduced, and a system being able to consistently position the tip in portions of the workspace unreachable with a non-compensated closed-loop control approach.

  Relevant Publications:

  - [1]Federico Campisano, Simone Calò, Andria A. Remirez, James H. Chandler, Keith L. Obstein, Robert J. Webster III, Pietro Valdastri, "Closed-loop Control of Soft Continuum Manipulators under Tip Follower Actuation.", International Journal of Robotics Research, 2019.

[1]Differently from this work, the proposed closed-loop control scheme is implemented in a polar coordinates system, considers the non-linearities of the actuation system and does not rely on a kinematic model to compute the tip wrench required to achieve a desired robot configuration.

- **Autonomy**: finally, the need for non-skilled personnel to use the HJ required the device to be able to perform simple tasks autonomously. In this way a non-expert user can deploy the endoscope in the gastric cavity, start the procedure and let the system perform the inspection of the stomach. The main advantage of such an approach is to be able to perform a repeatable and reliable scanning of the stomach mucosa using a structured motion trajectory of the endoscope tip, in this way being sure that the whole environment can be visually analysed.

  In this regard, the previously developed control system has been used to implement a zig-zag trajectory following strategy. Alongside the main motion behaviour, the tip of the endoscope must also be aware of the surroundings in order to recognise collisions with the stomach walls and react accordingly. This is essential if the continuation of the procedure must be guaranteed. An obstacle detection algorithm thus developed for these purposes and relies on comparison between measurement and estimation of the pose of the tip provided by a sensor and a kinematic model of the soft bending section, respectively. Since the resulting pose generated by the Forward Kinematics (FK) is not influenced by external disturbances (such as the collision with an obstacle), the comparison between this information and the actual measure of the pose can be used as an indicator of a collision.

  Inevitably, the presence of the obstacles and the lack of a-priori knowledge about their shape leaves part of the workspace unexplored. To avoid this problem, a combination of mapping and planning strategies have been developed. When the endoscope tip moves, a 2D $[\varphi, \vartheta]$ map of the obstacle-free space is built. At the end of the scan (e.g. ϑ reached a maximum value), the map is evaluated and unexplored areas are located. Then a route from the current pose to the unexplored area is evaluated by applying a path planning algorithm on the free-space map. The system continues with the scanning and map evaluation tasks until the procedure is complete (i.e. all accessible space has been explored).

  Relevant Publications:

  - Campisano, Federico, Andria A. Remirez, Simone Calò, James H. Chandler, Keith L. Obstein, Robert J. Webster, and Pietro Valdastri. "Online Disturbance Estimation for Improving Kinematic Accuracy in Continuum Manipulators." IEEE Robotics and Automation Letters 5, no. 2 (2020): 2642-2649.

- [1]Campisano, Federico, Andria A. Remirez, Claire A. Landewee, Simone Calò, Keith L. Obstein, Robert J. Webster III, and Pietro Valdastri. "Teleoperation and Contact Detection of a Waterjet-Actuated Soft Continuum Manipulator for Low-Cost Gastroscopy." IEEE Robotics and Automation Letters 5, no. 4 (2020): 6427-6434.

Thesis Structure

The body of work of this thesis is organized into 6 chapters, with Chapter 2 to 5 highlighting the main technical contributions and Chapter 1 and Chapter 6 introducing the topic and discussing the results and conclusions of the work respectively.

- **Chapter 1**: an in depth literature analysis of the state-of-the-art in the field of gastroscopy is introduced, highlighting the potential for a low-cost alternative for gastric cancer screening as a solution to known disadvantages of standard flexible endoscopy. Then, a number of commercially available and research platforms are introduced. The key advantages of adopting a low-cost alternative to flexible endoscopy as a tool to perform population based gastric cancer screening programmes are presented.

- **Chapter 2**: the HJ endoscopic platform is described in detail, starting from its first prototyping phase up to its latest stage of development. The identified limitations of the original platform form the research focus of this thesis.

  In this chapter specifically, the steps that led to the development of a intrinsically stable and miniaturized water-jet actuated soft endoscope are presented, starting with the design and fabrication process of the device. Considering the technical requirements, each design choice and iteration is presented and discussed, then the fabrication and assembly techniques are described. The results of the extensive testing of multiple design variables are finally shown to prove the effectiveness of the mechanical improvements in the final device.

- **Chapter 3**: in this chapter, an optimized solution to the HJ actuation problem is presented. The flow-rate control devices (valves) used in the

[1]The proposed obstacle detection approach is based on thresholds applied to trigger signals, as it happens in this article and in the related literature. However, the custom trigger signals and the threshold values tuning procedure guarantee reliability and a higher responsiveness of the system with respect to the results presented in this article.

inherited HJ platform are described, alongside the advantages and disadvantages they bring to this particular application. A novel approach to controlling the water flow-rate, based on tube compression in between an eccentric mechanism and a custom shaped profile, is subsequently presented and referred to as ECV. A first prototype of the valve is characterized in terms of its principle of operation, input-output flow-rate characteristics and induced tubing plastic deformation. Consequently, a valve shape optimization aimed at obtaining a linear input-output valve characteristic is performed. Finally, the ECV was comprehensively tested both in a standalone configuration and within the HJ hydraulic system in the attempt to asses its augmented performance in controlling a fluid flow-rate or finely position the HJ tip.

- **Chapter 4**: a control system architecture is presented in this chapter. The HJ endoscope tip is controlled in a closed-loop fashion using a polar coordinate system $[\varphi, \vartheta]$. A first position control strategy acting on the water jet forces is implemented assuming a perfect linear valve input-output characteristic. The results show that the intrinsic hysteresis of the HJ actuation system generates unwanted behaviours of the plant, leading to tip instability in specific configurations. Using a hysteresis model, the hysteretic loop was then taken into consideration, leading to improved tip positioning performances and a more responsive system.

- **Chapter 5**: in this final technical chapter, the HJ platform is equipped with intelligent capabilities. These mainly consist of the ability to perform a full inspection of the environment autonomously or with minimal intervention of the user. In order to fully inspect the gastric mucosa, a coverage technique that takes advantage of the control strategy introduced in the previous chapter is described. Then, an obstacle detection algorithm that makes the manipulator aware of interaction with the surroundings is presented and tested. At this point the HJ endoscope is able to move and react to collisions but cannot guarantee that the environment has been completely inspected (e.g. the endoscope tip remains trapped in between two obstacles). To overcome the problem, a real-time mapping of the workspace is introduced and coupled with active path planning to allow tip repositioning and scanning of unexplored regions. Results of the autonomous capabilities of the HJ in different environment configurations are here presented.

- **Chapter 6**: the findings of the work are summarized and discussed in this chapter, together with the limitations of the proposed approach and possible future solutions.

Chapter 1

State of the Art in Gastro-Intestinal Endoscopy: a Review

In this chapter, current technologies for the assessment of the Gastro-Intestinal (GI) tract are reviewed. In particular, procedures based on standard FE and alternative approaches are introduced. Commercially available devices and research platforms providing a low-cost option for endoscopy in Low- and Middle-Income Countries (LMIC) are also presented.

1.1 Global Impact of Cancer

Cancer is the leading cause of death worldwide being responsible for 8.2 million deaths in 2012 [20], 8.8 million in 2015 and 9.6 in 2018 [1, 19].

The GLOBOCAN Project[1] aims to estimate and provide data about inci-

[1]GLOBOCAN Project is an initiative of the International Agency for Research on Cancer or IARC. The project aims to provide everyone is interested in cancer research, with the most

Cancer site	New Cases
Lung	2,090,000
Breast	2,090,000
Colorectal	1,800,000
Prostate	1,280,000
Skin cancer	1,040,000
Stomach	1,030,000

Cancer site	Deaths
Lung	1,760,000
Colorectal	862,000
Stomach	783,000
Liver	782,000
Breast	627,000

Table 1.1: Most common cancer types and top 5 causes of cancer related deaths for both sexes worldwide, 2018. (Adapted from [19])

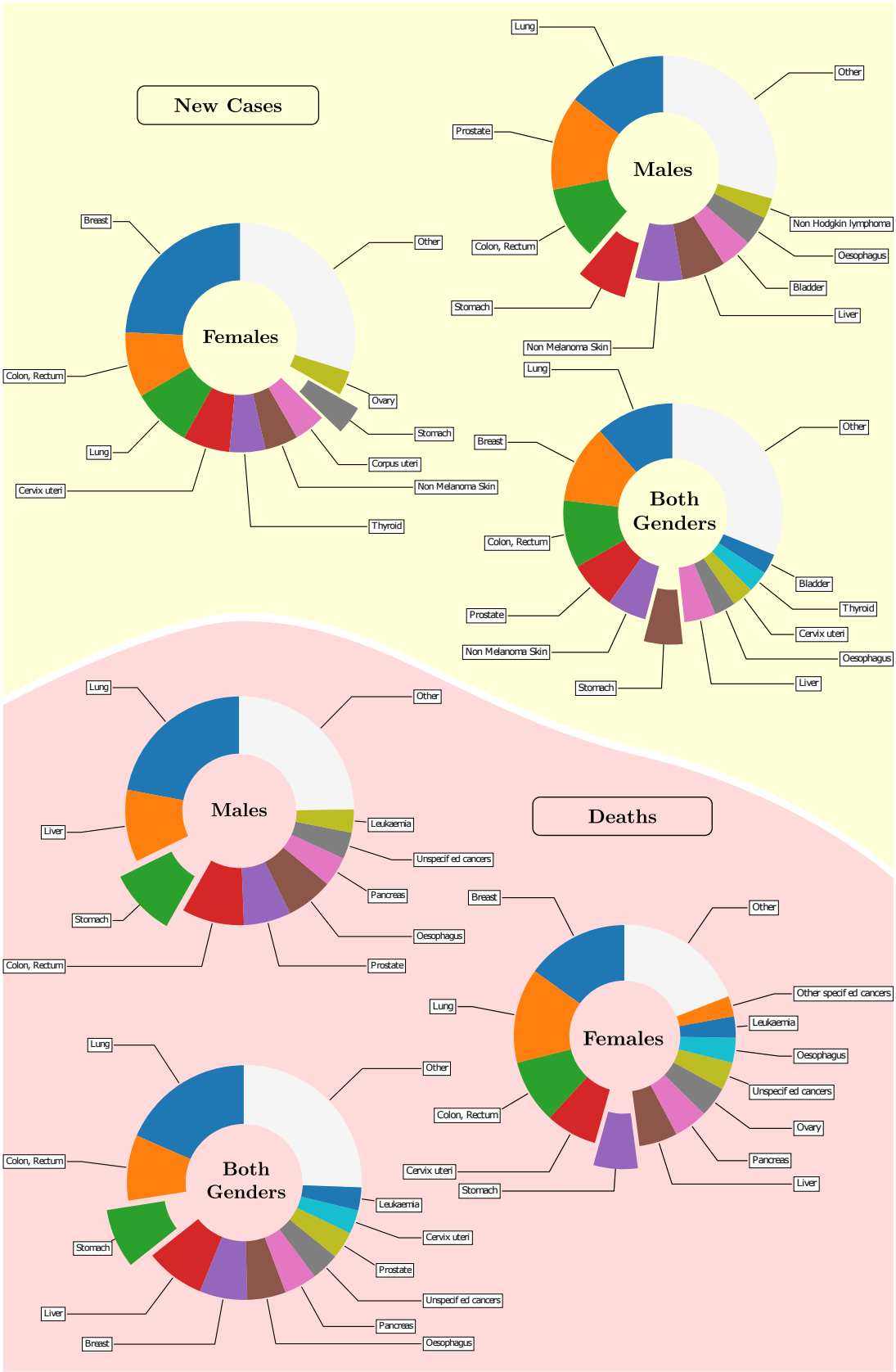

Figure 1.1: Estimated incidence and mortality of the most common types of cancer, worldwide. Adapted from [1].

Cancer site	New cases	%	Deaths	%
World	951,600	100	723,000	100
Less Developed Countries	677,100	71.1	548,400	75.8
Asia	700,000	73.5	527,100	72.9
Eastern Asia	552,900	58.1	394,600	54.5

Table 1.2: Estimated number of new cases and deaths due to gastric cancer. (Adapted from [20])

dence, mortality and prevalence, for the major types of cancer in 184 participant countries [21].

As shown in Figure 1.1 and Table 1.1, gastric cancer is the sixth most common type of cancer worldwide while, in terms of deaths, it ranks third after lung and colorectal cancer, accounting for more than 8% of the total deaths attributable to cancer.

The distribution of gastric cancer varies greatly across geographical regions [20]. Considering developed and LMIC separately, the rank in Table 1.1 changes considerably; in more developed regions breast cancer becomes the most common type of cancer, followed by prostate, lung, colorectal and stomach cancer. In less developed areas, stomach cancer occurs more frequently, becoming the third most common type of cancer.

Furthermore, analysing the data in terms of geographical area, it is essential to note that a large proportion of new cancer cases (29.4%) and deaths (33.36%) occur in Eastern Asia. When only data related to stomach cancer are considered, 70% of new cases are located in developing countries. Of these, almost 60% are located in Eastern Asia, with the highest peak registered in China. Similar considerations apply for deaths caused by stomach cancer: 76% of the total occurs in less developed countries, specifically in Eastern Asia where a 54% death rate was estimated (Table 1.2) [20].

1.2 Gastric Cancer

1.2.1 UGI Tract Anatomy

The GI tract extends from the mouth to the anus and is conventionally divided into three parts: upper, middle and lower. The upper part of the GI tract (UGI) includes esophagus, stomach and duodenum (Figure 1.2a).

recent and reliable data and statistics about the major types of cancer and previsions for the future.

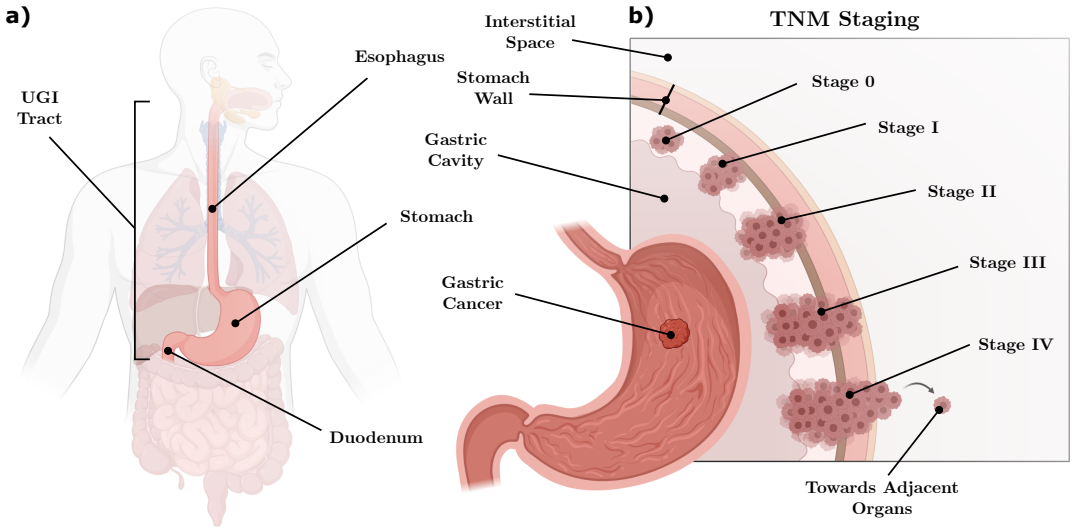

Figure 1.2: Upper Gastrointestinal Tract anatomy (a) and gastric cancer development stages (b) according to the TNM classification (depth of tumor infiltration). Created with BioRender.com

- The esophagus is a 25 - 26 cm long, muscular tube, 2 - 3 cm in diameter, normally collapsed at rest. It runs from the throat to the stomach to which is attached through the esophagogastric junction or cardia. The basic propulsive movement that allows the bolus to reach the stomach is the involuntary muscular process known as peristalsis. This is a common feature in smooth muscular tubes and it consists in a local contraction ring (internal lumen reduction) that progressively spreads along the tube, from the pharynx towards the lower part of the esophagus, forcing the bolus to reach the stomach [22].

- The stomach is a dilated section of the alimentary canal placed between the esophagus and the intestine. This organ shows variable dimensions depending on the age and sex. On average the volume is about 1,200 ml, the overall length measures 29 - 30 cm and a cross-sectional diameter increases in the range of 5 - 10 cm when passing from the distal to the proximal regions [22].

- The duodenum is the first section of the small intestine. Approximately, it is a 30 cm long, C shaped tube, 47 mm in diameter [22].

1.2.2 Classification

Conventionally, gastric cancer is classified into two broad groups as proposed by Lauren [23]: intestinal and diffuse type. The first is typical in older subjects,

and it is strongly associated with the presence of Helicobacter Pylori (H. Pylori) infections [24]. Conversely, the diffuse type is mainly diagnosed in young individuals and it does not show the same strong correlation with H. Pylori infection. A different classification approach, called TNM, considers three factors, such as the tumor infiltration (T), nodes involvement (N) and the presence of metastases (M), to identify the cancer development stage ad assign it to a severity level from 0 to IV, with IV being the most severe stage (Figure 1.2b).

Since gastric cancer is silent during its early stages of development, the associated lack of symptoms often results in a late dignosis. Even though treatments for advanced stage gastric cancer have improved in recent years, late diagnosis results in a poor prognosis with a five-years survival rate lower than 20% [25]. Early diagnosis has the potential to stop the spreading of the disease before it reaches deeper layers of the tissues, in this way resulting in a increased survival rate up to 90% [26].

Generally, gastric cancer incidence is higher in less developed countries. In these geographical regions, lower and middle classes are more affected by this disease mainly because they are more exposed to potential sources of H. Pylori infections. Despite worldwide gastric cancer incidence decreasing in recent decades, it still remains a significant problem in terms of number of deaths per year for countries such as China; characterized by two-thirds of the population living in rural areas. Here, the incidence rate has not seen the same significant reduction in the last years [27].

1.2.3 Risk Factors

There are a number of factors influencing the risk of developing gastric cancer, classified by IARC in groups from 1 to 4 (low to high risk) according to scientific evidence about their carcinogenic effect on humans (Table 1.3):

- First of all, infection caused by of H. Pylori. This infectious agent has been classified as carcinogenic to humans (group 1) and ,of the 2,200,000 gastric cancer cases attributable to infective agents, H. Pylori ranks first and is responsible for 770,000 (35.4%) new cases [28].

- Tobacco smoking and alcohol consumption are also related to an increased risk of gastric cancer. In particular smoking tobacco has been found to increase the risk of 2.5 factor if compared with non smokers [29].

- Dietary habits such as low vitamin C and excessive salt intake have also been shown to be associated with an higher risk [29].

Cancer site	Sufficient evidence	Group	Limited evidence	Group
Stomach	Helicobacter Pylori	1	Asbestos	1
	Rubber production industry	1	Lead compounds	2A
	Tobacco smoking	1	Salted fish, Chinese-style	1
	X/Gamma-radiation	1	Processed meat	1

Table 1.3: List of Classifications by cancer sites with sufficient or limited evidence in humans. Adapted from: IARC

- The incidence of the two different types of gastric cancer, topographically defined as cardia and non-cardia, changes according to the ethnicity of the subjects. It has been shown that cardia gastric cancer is more common in white people whereas Hispanics and Asians tend to develop non-cardia cancer [30].

- Age and sex are also important in determining the risk to develop gastric cancer. In particular, the risk increases with age and men have an higher risk to develop the disease [30].

1.2.4 Methods for Upper Gastric Cancer Detection

To date, several different types of tests have been considered and their performance analysed with the aim of determining which one owns the best diagnostic capabilities in terms of early detection of gastric cancer, patient acceptance, cost-effectiveness, sensitivity and specificity. The most common type of diagnosis methods are the following:

- SEROLOGY: the simplest and less invasive method consist in testing the presence of H. Pylori antibody or checking levels of Pepsinogen (PG) I and II as they are correlated to the functional status of the gastric mucosa. The test consists in an easy to perform and cost-effective blood test [31] that evaluates the ratio PG I/II and compares it to a predefined cut-off value. Some studies proved that this test has a relatively high sensitivity and specificity and can lead to a reduced gastric cancer mortality. Since these results are not strong enough and standard guidelines for determining the cut-off threshold do not exist, serology methods are not being widely used for screening purposes, rather only to identify and shortlist high risk subjects. The selected patients are then screened with a different and more reliable method [30].

- *X-RAY:* this test is based on the ingestion of a barium meal to obtain a good contrast on the resulting image. This procedure was introduced

as a standard method in the first Japanese screening programme thanks to evidences showing a reduction of gastric cancer mortality (40% - 60%) [30, 31]. Despite proofs of effectiveness exist, x-ray based methods present some limitations influencing the level of participation in screening study such as: fear of the consequences of radiations, unappealing barium meal, constipation after the procedure. Moreover, very often, an additional endoscopy is required to confirm the diagnosis [31].

- *ENDOSCOPY:* over the years, endoscopy has become the gold-standard for gastric cancer diagnosis. This trend is supported by a high detection rate, especially for early stage gastric cancer (more than twice if compared with x-ray based tests), some new, even if weak, evidence of reduced mortality as a result of screening by endoscopy, and the possibility of performing biopsy during the procedure [32, 33, 34, 35]. The possibility to visualize the stomach mucosa allows to localize the abnormalities and define the tumor development stage, while tissue samples collection enables histological confirmation of the diagnosis and tumor staging. Some limitations exist and prevent the effective use of this device in large scale screening programmes. Experienced and skilled physicians are essential to maximize the detection rate, the cost per procedure is generally high because of the mandatory sterilization of the equipment at the end of the endoscopy, and the overall capital cost required to purchase the equipment is generally high, in this way limiting the number of available units. Moreover, adverse effects and patient discomfort are more frequent when compared with an x-ray based method [31].

1.2.5 Prevention

The battle against cancer can be carried out through different approaches, such as prevention and treatment, with strong evidences proving prevention as the most appropriate choice thanks to the higher survival rate and cost associated to the patient assessment and follow up. Two types of prevention can be identified: primary and secondary [36].

Primary prevention involves the set of actions whose principal goal is to prevent the carcinogenic agent to come into contact with the subject (smoking, dietary habits, etc). The IARC H. Pylori working group concluded that H. Pylori eradication, as a primary prevention method, is effective in reducing gastric cancer incidence and recommends the eradication of the carcinogenic agent as standard practice to be adopted in control programmes [37].

On the other hand, secondary prevention consists in detecting pre-malignant lesions in order to be able to treat the disease in its early stages, before symptoms onset. This prevention method is carried out through check-ups and screening programmes and includes diagnostic techniques such as endoscopy, x-ray, etc (see Section 1.2.4).

Even though primary prevention is considered to be more effective than secondary, its use is not as widespread as one expects. One of the reasons lie in the complexity of recognizing the actual contribution brought by the prevention programme, consequently generating inconclusive proofs of effectiveness. Therefore, secondary prevention has become the standard practice in the majority of gastric cancer control programmes and its performances were largely analysed by several research groups. Results from a Scopus data analysis, using "*gastric cancer screening*" keywords, are shown in Figure 1.3. A continuously increasing interest in the field of gastric cancer is highlighted by the data in Figure 1.3a, where the number of published scientific articles concerning research in the field of gastric cancer each year, are shown. As previously mentioned, Eastern Asia countries show the highest risk of gastric cancer worldwide and for this reason countries such as China, Japan and Korea are the most interested in controlling the burden of this disease (Figure 1.3b).

Despite this increasing interest in gastric cancer, only a few high-risk countries have developed gastric cancer screening programmes in the attempt to control the spread of the disease [29]. In Eastern Asia, only Japan and Korea promoted mass-screening programmes supported by well defined national guidelines to properly realize them in a standardized form. A similar situation can be found in low-incidence areas such as Europe and USA where opportunistic and individual screening strategies have been adopted [38]. The reasons for this lack of control programmes in other high-risk countries are to be found in the absence of a widely accepted method for gastric cancer screening and the cost-effectiveness of the programmes. The latter explains the choice to not implement control programmes in intermediate and low-risk countries [39].

In Japan, interest in gastric cancer screening started in 1960 [40] with a small screening programme implemented in only one prefecture. Then, in 1983, the programme was extended to provide annual screening for residents aged 40 or older by x-ray based methods [30]. In 2005, the first version of Japanese guidelines for gastric cancer screening appeared and recommended photofluorography as a standard method for population based and opportunistic screening. This strategy was based on evidence showing that screening using photofluorography was connected to a reduced mortality. Endoscopy was thus excluded from the list

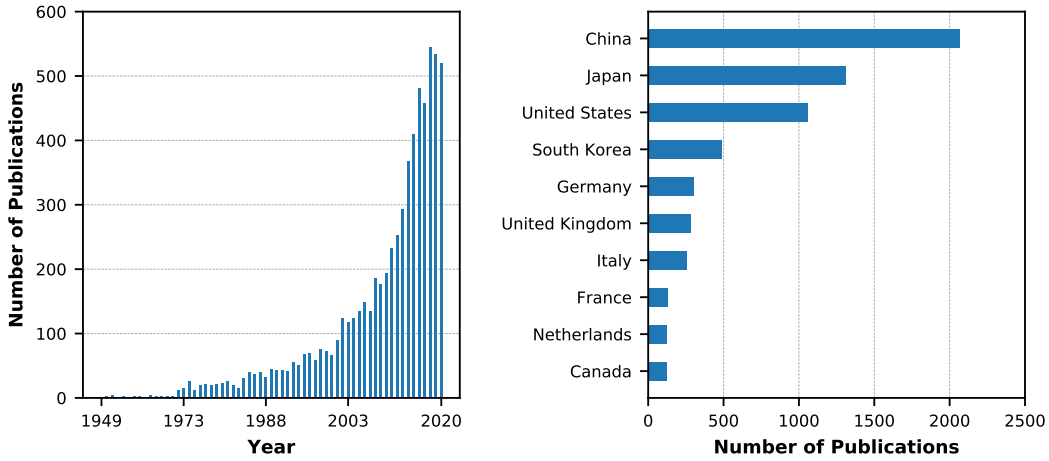

Figure 1.3: Number of documents matching the keywords "*gastric cancer screening*" a) published over the past 70 years and b) sorted by country of publication since 1949. Adapted from: Scopus

of recommended screening methods due to insufficient evidence of efficacy [41]. In 2015, guidelines have been revised and thanks to new, even if weak, evidence endoscopy was re-introduced in the recommended screening practice [34].

In Korea, a national cancer screening programme was launched in 1999. A few years later guidelines were introduced recommending endoscopy or x-ray methods with a two years screening interval as a standard approach for gastric cancer diagnosis [42, 43]. A revised version of guidelines, in 2015, recommended endoscopy as the only method for gastric cancer screening in Korea, primarily because of the cost-effectiveness of the procedure.

In China no gastric cancer screening programmes have been implemented [38]. The attention and efforts are focused on the eradication of H. Pylori [31]. The results of these trial studies are not promising, in part due to an high re-infection rate [44].

Despite the above mentioned countries trying to reduce the incidence and mortality related to gastric cancer through different methods, the difficulty in covering the entire national territory still represents a problem. The lack of experienced personnel, the scarcity of equipment and the economic efforts, make the examination available only for a restricted part of the original target group defined by the guidelines [45]. Rural areas remain the most disadvantaged regions, mainly because of the absence of screening equipment or the distance from state-of-the-art medical facilities; commonly located in big cities [29].

1.3 Endoscopy

Nowadays, endoscopy represents the standard and the most widespread approach for gastric cancer diagnosis [46]. The procedure relies on the endoscope: a flexible tube with a steerable tip. Its design allows the physician (GE) to inspect parts of the body otherwise unreachable with different, non-invasive approaches. Over the past few years there has been an increasing interest in the development of new devices that guarantee performance similar to that exhibited by FE and, at the same time, improve patients' acceptance, reduce the cost related to the equipment and the procedure, etc.

1.3.1 Standard Practice

As previously mentioned, a FE consists of three main sections: the user handle, a flexible cylindrical body and a steerable section at the distal end (Figure 1.4a and b). The actuation mechanism relies on the pulling action of cables (Bowden cables) organized in an antagonistic fashion and connected to knobs on the control handle and, distally, to the endoscope tip. Given this cable arrangement, turning a knob on the handle results in a motion (bending) of the distal section of the flexible tube. In this way, inspection of a certain region of the human body is possible by directing the camera module located at the tip of the endoscope.

Besides control wires, the body of the endoscope generally contains a tool channel, additional lumen for suction/injection of air or water, optic fibers carrying white or R, G and B light and electrical connections for the CCD/CMOS sensor. All of the above mentioned components are included in a 0.925 - 1.1 m long flexible tube with diameter in the range 4.9 - 12.8 mm (standard upper endoscopes diameter ranges from 8 to 10 mm, devices with a smaller diameter exist but are considered a non-standard equipment). The standard resolution of the image sensor varies from 100,000 to 400,000 pixels but, in some recent versions, it reaches HD quality (850,000 to more than 1,000,000 pixels) [47].

The endoscope is manoeuvred by the physician via the handle. On the control handle, the two knobs connected to Bowden cables allow the endoscopist to move the tip up and down (maximum values of 210° and 90° respectively) or left and right (maximum values of 100° and 100° respectively [48]) as shown in Figure 1.4c. Moreover, a tool channel allows for a tool, such as biopsy forceps or an aspiration needle, to be inserted and used during the procedure. Finally, additional switches are reserved for water or air injection and for suction.

In addition to the well established features, some improvement in vision tech-

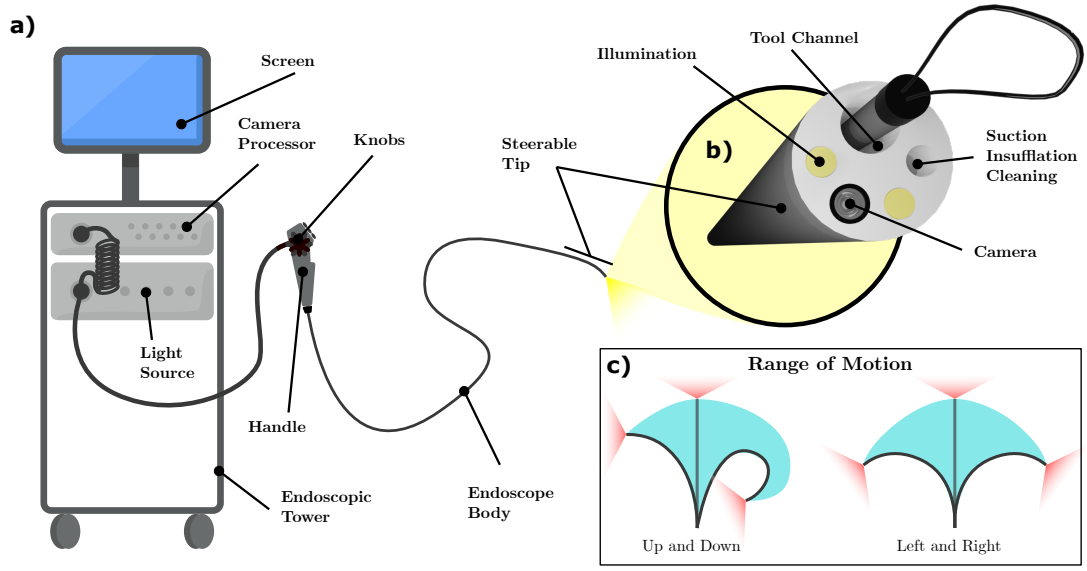

Figure 1.4: Flexible endoscope: a) overall system, b) steerable tip design features and c) range of motion

nologies have helped endoscopy becoming the gold-standard method for gastric cancer diagnosis [47]. First of all, the introduction of HD sensors enhanced the detection of small, early stage mucosal lesions, otherwise invisible with Standard Definition (SD) devices. Dye-based chromoendoscopy consist in the use of dyes that, once applied on the mucosa, react with the tissue highlighting particular structures (lesions or abnormalities). Finally, optical chromoendoscopy, also known as Narrow Band Imaging (NBI), emphasize capillary structure and mucosal surface thanks to the filtration of the red component of the light. All these functionalities are often combined and are responsible for an increased detection rate, sensitivity and specificity of the endoscope.

Despite the development of such features, FE design remained widely unchanged over the years, and some major problems are still limiting its full potential. First of all, direct cost related to the acquisition of the equipment, can easily exceed 80,000 USD. Indirect costs must also be taken into account, including, for example, the reprocessing of the device after each procedure. This can be performed in a number of different ways, resulting in a different level of effectiveness in the sterilization of the device. Funk et al. compared manual and automated endoscope reprocessing methods: manual sterilization consist in several steps that have to be followed meticulously by the operator to obtain a safe-to-use endoscope, while an automated method relies on an Automated Endoscope Reprocessor (AER) [49]. Improper reprocessing can leave infective agents on the endoscope and this can cause the diffusion of pathogens in healthy patients [50]. For these reasons, manual reprocessing, even if executed in ac-

Figure 1.5: Cleaning facilities in two Chinese Hospitals in (red) Tianjin suburbs (Xianshuigu Hospital) and (green) Tianjin city center (Tianjin Medical University General Hospital)

cordance with the guidelines has been linked to sub-optimal sterilization results and it is also responsible for a lack of efficiency in terms of reprocessing time [51, 52, 53].

AERs, on the other hand, are the recommended standard for endoscopes cleaning (World Gastroenterology Organization, WGO) because a reproducible set of cleaning steps and conditions can be guaranteed. AERs have also the potential to reduce the risk of damaging the endoscope, in this way reducing the economical impact of repairing (an average of 5,833 USD per device [54]) and preventing procedures to be cancelled due to the unavailability of the devices. The problem that arises form the use of AERs is mainly financial and is represented by the high cost related to purchasing the equipment [54]: its high upfront capital cost makes AERs accessible only by facilities in high resource settings.

An on-field experience in Tianjin (China) confirms the disparity between high resource settings and rural areas in China (figure 1.5), in terms of available facilities for endoscopes sterilization. In particular, in rural areas manual reprocessing represents the standard practice, whereas, in the main hospital of the city, the automated approach has been adopted. It must be highlighted that, in this particular case, AERs had just been purchased by the hospital; this means that manual reprocessing has been the standard approach also in this premises.

The usability of FE represents another limiting factor. The actuation approach that characterizes FE requires a highly skilled user to guarantee proper deployment of the device and to carry out the procedure reliably and in a short time. As the ability to control the device and the experience to identify suspicious lesions is essential, an extensive training is required for the physician to

feel confident with the equipment and to optimize the outcome of the inspection. The compulsory training represents another item of cost and inevitably reduces the number of users that can perform the procedure, in this way limiting the effectiveness and advancement of screening programmes.

Finally, classical endoscopes are characterized by limited portability due to the size of the endoscopic tower (Figure 1.4), the need of electric power and reprocessing facilities; consequently, remote rural areas can not be easily reached with such an equipment.

1.4 Robotics in Medicine

The need for a simpler, more precise and repeatable way to perform medical operations or, more specifically, endoscopy procedures, led to the introduction of robotics in medicine. The automation brought by robotics addresses the need for an intermediate layer in between the user and the tool. The commitment of robotics is to enable more intuitive, precise and dexterous movements and, as a direct consequence, a lower time-to-completion of a general medical procedure [55]. Moreover, on an even higher abstraction level, the user could be partially or completely replaced by the Artificial Intelligence (AI), in this way implementing semi- or fully-autonomous systems [56].

1.4.1 Capsule Robots

Wireless capsule endoscopy represent a valuable alternative to classic FE even if it is affected by several limitations that prevent this class of medical devices to completely replace FE.

The first capsule was presented in 2000 by Given Diagnostic Imaging. The capsule, called M2A and then renamed PillCam, consisted of an optical dome, lens, LEDs, a CMOS image sensor, batteries and an antenna. All the components were contained in a 11 by 26 mm cylindrical shell. Other companies estabilished a research branch in this field, developing products such as EndoCapsule (Olympus, Tokyo, Japan), OMOM (Jinshan Science and Technology Company, Chongqing, China), Mirocam (IntroMedic, Seoul, Korea) and CapsoCam (Capsovision, Saratoga, CA, USA). These capsules are characterized by similar up-to-standard features in terms of camera FoV, battery life, size and, above all, the promise for a less invasive procedure. By contrast, their passive form of actuation (mainly peristalsis) and the lack of a tether introduce a number of drawbacks concerning the controllability, tissue sample capabilities and

full visualization of large hollow organs (e.g. stomach) [57, 58].

To achieve active control of the capsule motion, a number of approaches has been explored and they can be divided into two groups according to the nature of the locomotive force: internal and external actuation.

When the locomotion is internal, the actuation system is embedded in the capsule body making the miniaturization of the device challenging and power consumption non negligible. Shape Memory Alloys (SMA) provide a self-contained form of actuation but they are difficult to control, they can generate low forces and they are not efficient in terms of power consumption. For this reason DC motors are more often used as a main propulsion system.

A common internal form of locomotion is a legged system. This kind of solution shows several advantages: it can move forward in the environment (e.g. colon) passing over injuries without touching the critical area, it can adapt to environments characterized by different dimensions (lumen adaptation), no insufflation is needed thanks to the interaction between the organ's walls and the capsule's legs that expands the lumen providing an appropriate view of the environment [59]. Several attempts have been carried out at Scuola Superiore Sant'Anna in Pisa trying to develop a robotic legged capsule: a first prototype was equipped with two sets of three legs [60], then a second version with four legs [61] and a prototype with two sets of six legs [2]. The increased number of legs allows the contact force with the walls to be distributed on more contact points optimizing the motion and reducing the risk of damaging the wall.

Such an approach well adapts to tube-like organs but the same does not apply to more challenging environment such as the stomach where a three-dimensional movement is required. Here, a common approach consists of distending the stomach using water and then performing the endoscopy using a swimming capsule. An example was described by De Falco et al.: a capsule equipped a vision system and a real time transmission module was developed. In addition, a set of propellers was added to provide the required thrust to move in the environment[3].

With an external locomotion approach, battery consumption can be drastically decreased, capsule dimension can be significantly reduced or more features can be added to the capsule. Magnetic actuation is surely the most prolific actuation method [62, 63, 64]. It is based on the magnetic coupling between an external and an internal magnetic field. The internal magnetic field is generally produced by a permanent magnet (or a set of permanent magnets) placed inside the capsule body. For the external magnetic field, several methods have been investigated. The hand-held magnetic manipulation represent the simplest approach to implement. A modified version of a magnetic capsule (MiroCam,

IntroMedic) was used by Kim et al. to monitor the gastric motility [65]. The patient swallows the capsule, equipped with permanent magnets, and an external magnet is used to drive the capsule in the desired position in the stomach cavity. Once the capsule is in position, the external magnet is fixed on a belt placed on the patient's abdomen. In this way a certain region of the stomach can be monitored for a relatively long period. Manoeuvering the capsule by manually moving the external magnet results in an inaccurate capsule actuation because the physician can only rely on the visual feedback provided by the camera and the mapping between the movement of the external and internal magnets is often counter-intuitive. A robotic manipulation of the external magnetic field has been shown to be more effective in terms of precision of the movements. A permanent magnet mounted on the end effector of a 6-DoF robotic arm was used by Ciuti et al. to steer a capsule device inside the colon [66]. A set of nine electromagnets was used by Son et al. in order to create an external magnetic field able to both move a capsule inside the stomach and deploy a needle to perform a biopsy [4]. A similar approach was adopted in [67]: in this case a static magnetic field gradient and a dynamic uniform field were used to selectively control individual members of a swarm of identical robots. MRI scanners have also been used for driving capsules. For example in [6] a miniature swimming capsule equipped with three elastic beams was developed. On each elastic beam, two coils create a magnetic field that, interacting with MRI magnetic field, produce vibration of the elastic structure in this way generating thrust. This capsule can be used for stomach inspection, but to allow the device to move, the stomach has to be filled with water.

A joint collaboration between Olympus Medical Systems Corporation and Siemens Healthcare led to the development of a magnetically guided capsule for the inspection of the gastric cavity [5]. The system consists of a capsule (Olympus) equipped with two image sensors, a permanent magnet and an external guidance magnet (Siemens). The external magnetic field is produced by a modified MRI scanner able to generate a weaker field (100 mT) if compared with standard MRI scanners. Before the procedure, the patient drinks 1.3 L of water in order to expand the stomach, then a single-use capsule is introduced in the stomach through the mouth. Finally, the external magnetic field is able to manipulate the capsule in the stomach with 5-DoF.

In a first feasibility study, Rey et al. were able to successfully visualize typical gastric landmarks in the distal stomach, with a lower percentage of success for landmarks in the proximal region because of the collapsed conditions of this part of the stomach [68]. In the follow-up trial Rey et al. used both a mag-

netically actuated capsule and a standard gastroscope to inspect the stomach cavity in order to compare the performances of the two systems [69]. Firstly, an high definition gastroscopy and then a capsule endoscopy have been performed. The visualization of the stomach landmarks was successful, including Fundus and Cardia which are located in the proximal region of the stomach. The capsule succeeded in identifying 31 lesions, not detected by the gastroscope. This result has been probably caused by the longer examination time needed for the capsule (17.4 minutes) if compared with the standard endoscopy (5.3 minutes). Moreover, minor lesions produced by the gastroscope have been recognized as abnormalities by the capsule.

A similar platform has been developed by ANKON Technologies and tested on 34 patients [70]. A C-arm robot, holding a permanent magnet, is able to move the magnetic capsule previously swallowed by the patient. In order to distend the stomach, the patient ingests both 1L of water and 6 g of air-producing powder. During the trial, the gastric landmarks have been successfully recognized but with an average examination time of 43.8 minutes.

The ability to collect tissue samples is also an essential feature for diagnosis. The absence of a tether makes the procedure complicated for wireless capsules, but several solutions have been developed to guarantee the possibility of collecting samples. Kong et al. proposed a capsule equipped with a rotational tissue-cutting razor [71]. Initially, the sharp edge of the razor is hidden inside the capsule body and it is pre-loaded using a torsional spring and kept in position using a paraffin trigger. When a tissue sample has to be collected, a heater melts the paraffin block, the razor rotates eccentrically and protrudes outside the capsule body cutting the tissue. Magnetic actuation has also been used for biopsy in [4] to perform a fine-needle aspiration procedure and in [72] where a capsule with a cylindrical rotating razor has been proposed. The capsule contains two cylindrical magnet, a fixed and a rotating one, the latter connected to a razor. At rest, the two cylindrical magnet are aligned and the razor is closed; when a strong magnetic field is applied externally, the razor rotates exposing a hole in the capsule shell. Pressing the capsule against the lumen wall, thanks to the external magnetic field, allows the tissue to penetrate inside the hole, then removing the external magnet, makes the razor rotate again to the rest position, in this way cutting the tissue.

A less invasive method for tissue analysis is the so called *optical biopsy*. It allows *in-situ* tissue evaluation using the properties of light. Some of the techniques the use such an approach are: fluorescence endoscopy, optical coherence tomography, confocal micro-endoscopy and molecular imaging [73]. Zhang et al.

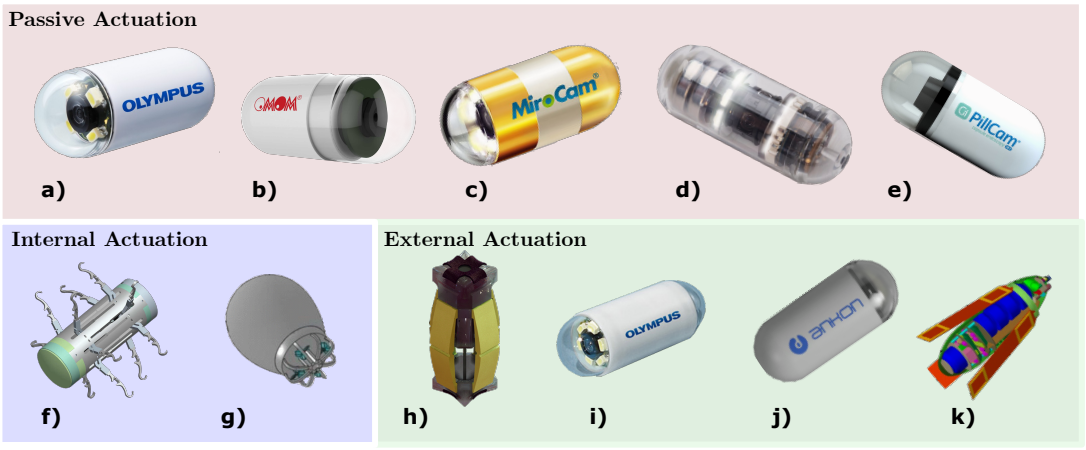

Figure 1.6: Design examples for wireless capsule endoscopy grouped by actuation approach. Passive actuation: a) Endocapsule (© Olympus), b) Omom (© JINSHAN Science and Technology) , c) MiroCam (© IntroMedic), d) CapsoCam (© CapsoVision) and e) PillCam (© Medtronic). Internal actuation: f) six-legged capsule (©2009 IEEE) [2] and g) swimming capsule (©2014 IEEE) [3]. External actuation: h) magnetically actuated capsule for fine-needle biopsy (©2020 Mary Ann Liebert, Inc., Publishers) [4], i) magnetically actuated capsule endoscope (©2012 IEEE) [5], j) ANKON Navicam magnetic capsule (© ANKON) and k) MRI driven swimming capsule (©2011 Springer Science) [6].

demonstrated the feasibility of biochromoendoscopy-based optical biopsy and the method has shown to be able to discriminate between malignant adenomas and benign lesions [74].

Power management is a challenging topic in capsule endoscopy. Batteries are the main power source in capsules and they have to provide energy to the system for a relatively long time allowing it to accomplish the endoscopic procedure. The energy stored inside battery is often not enough to guarantee so, especially in the case of internally actuated or multi purpose capsules. Moreover, batteries are often bulky and occupy the majority of the space available inside the capsule. For this reason, different approaches such as externally rechargeable batteries or battery free devices have been proposed. Jia et al [75] developed a wireless power transmission system based on an external transmitting coil and an internal three-dimensional coil included in the capsule. The system is able to transmit up to 500 mW of power even though the transmission efficiency remains quite low (4.08%).

1.4.2 Continuum Robots

As proposed in [76], a continuum manipulator (CM) *is an actuatable structure whose constitutive material forms curves with continuous tangent vectors.* This definition clearly highlights how such manipulators do not consist of links and joints, as seen in classic rigid robots, but rather involve a continuously bending

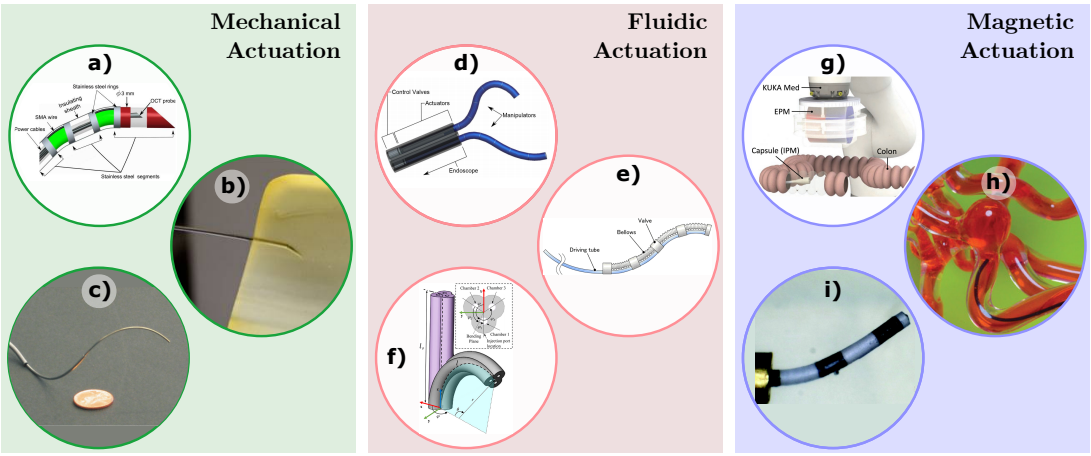

Figure 1.7: Actuation of CMs. Mechanical actuation: a) SMA (©2013 SAGE Publications) [7], b) bevel tip steerable needle (©2006 SAGE Publications) [8] and c) concentric tubes robot (©2006 IEEE) [9]. Fluidic actuation: d) McKibben muscles (©2012 ASME) [10], e) hydraulic soft catheter (©2006 IEEE) [11] and f) pneumatic soft robot [12]. Magnetic actuation: g) coupling between an internal and an external permanent magnet (©2019 IEEE) [13], h) ferromagnetic particles [14] and i) multiple permanent magnets (©2019 Sungwoong Jeon) [15].

elastic structure whose shape is dictated by the forces and torques acting on the structure. The theoretically infinite number of DoF offered by these structures makes them perfect for applications requiring high dexterity. In contrast with rigid tools with a dexterous wrist, CM have the ability to boost medical procedures. When a direct straight path to the target is not feasible, the ability of CM to adapt to the surrounding environment represent a solution with the potential to minimize tissue trauma and accelerate the recovery time.

At the same time, CMs have the capacity to overcome the major problems exhibited by wireless capsule endoscopy. The tether can contain wires for direct power transmission and real-time data streaming, a tool channel can be embedded for biopsy and sample collection. Furthermore, the presence of the tether offers an anchoring point that facilitates the movements in hollow organs. Such robotic platforms can be divided into three groups, according to the nature of the actuation system: mechanical, fluidic or magnetic as proposed in [55] and shown in Figure 1.7.

In a mechanically actuated CM, actuators such as SMAs, tendons or the robot's geometric characteristics are used to generate a wrench or distributed load that, consequently, produces a movement of the manipulator. The FE belongs to this group of CMs.

Single and antagonistic SMA tendons were used by Crews et al. [77]. Whereas a multi segment approach has been used by Ayvali et al in order to independently actuate each joint of the manipulator [7]. In [8], the geometric characteristic of the tip of a flexible needle is used to steer towards the target wile being inserted.

The needle's bevel tip, when in contact with a tissue, generates an asymmetrical force that redirects the needle along a curvilinear path. A combination of insertion and axial rotation generates complex needle paths allowing obstacle avoidance. In [9] pre-curved, concentric, super-elastic tubes are rotated and translated with respect to each other to reach a target position. With such an actuation approach, based on solid mechanisms, mechanically actuated CMs are often stiff and their interaction with human tissue could be cause harm.

CMs equipped with fluidic actuators proceed beyond classic pneumatic or hydraulic pistons and take advantage of the properties of flexible actuators that well adapt to the elastic and compliant nature of a CM. Actuators such as McKibben muscles, together with PAM (Pneumatic Artificial Muscles) are well known and have been widely used in the field of CM [10]. The increasing interest in the field of soft robotics led the way to the development of novel, fully-soft fluidic actuators. These actuators rely entirely on their own geometric characteristic to produce a predefined type of movement, such as bending, elongation or twisting.

Ikuta et al. developed a multi joint, bellows-based actuation [11]. The catheter consists in a driving central tube filled with saline solution and a set of joints each controlled by an asymmetrical bellow and a 3-stage valve. The valves allow to control each joint independently and simultaneously using a single pressurized line, thanks to a different opening/closing pressure of each valve [78]. In [79] a soft robot implements an inchworm-like locomotion approach to explore the colon by adopting two expandable structure placed at each extremity of a cylindrical structure and used as anchoring points. A central linear soft actuator allows the robot to axially shrink and expand. The concurrent use of these soft structures allow the robot to proceed forwards or backwards in the colon.

In the field of medical robotics, the compliance of the CM represents an advantage in terms of robot's dexterity, but it is not enough to guarantee a safe interaction between the manipulator and the tissues. Soft CMs deal with this limitation by using highly compliant hyper-elastic polymers as main constituent materials (e.g. silicone). To this end, a big effort has heen made, not only towards the development of soft CMs and soft actuators, but also in favour of soft control system (e.g. valves). An example is the soft electric valve developed in [80] or the mechanical one described in [81], both designed to be directly embedded in the CM's body.

A pneumatically actuated system for colonoscopy has been proposed by Chen et al. [82]. This continuum robot is based on three pneumatic chambers embedded in a 17 mm diameter, silicone rubber, cylindrical body that resembles a compliant Stewart platform. By inflating or deflating each chamber, the manip-

ulator is able to deflect up to an angle of 120°. A similar concept is proposed in [12] where a miniaturized (10 mm diameter) parallel manipulator is described. The geometry of the internal channels, the constituent material and the fabrication process guarantee a significant range of motion (> 180°) and, at the same time, reduce the risk of rupture.

In a magnetically actuated CM, the actuation of the robot mainly relies on the ability to manipulate an external magnetic field. In this way, the onboard actuation system of the CM becomes as simple as a permanent magnet, facilitating the miniaturization of the device or the introduction of additional features.

A magnetic field based approach for painless colonoscopy has been developed by Valdastri et al.: a tethered capsule equipped with a permanent magnet is pulled along the colon taking advantage of the magnetic interaction established between the capsule and an external permanent magnet held by a robotic arm [83]. Additional capabilities were then added, culminating with the implementation of magnetic manipulation of an ultrasound probe [84], capsule levitation [13] and autonomous control [85]. The feasibility of miniaturization offered by magnetic manipulation was further exploited in [86] and in [14] where a submillimeter soft CM was presented.

1.4.3 Low-Cost Devices

Being cost, portability, reprocessing and repairing considerable issues related to FE in LMIC, the use of a disposable low-cost device actuated using simple mechanisms could represent a viable alternative for gastric cancer screening in these areas (Table 1.4). This class of device needs minimal or no reprocessing and can be easily transported to rural areas due to their actuation systems relying on manual actuation or a minimum amount of energy; deliverable by a self contained battery. In addition to this, the inconveniences introduced by planned or extraordinary FE maintenance are minimized.

In order to develop a low-cost device of this nature, critical aspects have to be taken into account [87]:

- Materials: cost, reliability and bio-compatibility of the constituent material;
- Manufacture: the fabrication process must be as simple as possible, in terms of production and assembly time;

Flexible Endoscope		Clinical Need
Average repair cost 5,833 USD Reprocessing cost from 114 to 280 USD	Cost	Less than 10 GBP per procedure for disposables
1% - 10% breakage rate	Maintenance	None
Essetial to avoid cross-contamination Requires proper equipment to minimize the risk (AER)	Reprocessing	None
Designed to be used in hospitals	Portability	Self-Contained and designed to be portable
Limited by the numer of available devices and the time required for reparing and reprocessing	Availability	Only limited by the numer of available devices

Table 1.4: Standard endoscopy vs. low-cost endoscopy comparison

- Functionality: diagnostic capabilities similar to FE to guarantee comparable effectiveness.

Several companies recognized the need and the value of investing in the development of low-cost systems for medical application. XENOCOR released the first inexpensive single-use laparoscope, the Xenoscope [88]. The idea is to provide developing countries with the same minimally invasive surgical tool used in modern settings, but at a lower cost. The plug-and-play laparoscopic device can be directly connected to exiting visualization equipment (laparoscopic tower monitors) and costs less than 100 USD.

The same objective has been pursued by EVOTECH [89]. The company tried to develop an affordable laparoscopic platform to help African and Indian women affected by physical disability and incontinence as a result of pregnancy complications. The device is called EvoCam and it costs 2500 USD.

In the field of FE, the PRIMESIGHT System [90] attempts to solve the sterilization problem by covering the endoscope with a sterile protective barrier (EndoSheath), in this way avoiding the need for high level disinfection. IntroMedic EG-Scan [91] and Ambu aScope [92], on the other hand, represent a fully-disposable solution for esophagus and bronchi inspection respectively, with new devices dedicated to UGI tract announced for 2021.

Besides commercially available devices, research in this field remains dynamic, with a number of different solutions released every year and addressing a particular need.

A significant example of device for UGI tract inspection is represented by the Bellowscope, a pneumatically actuated endoscope for unsedated assessment of UGI tract developed by Garbin et al [93]. The device consists of a multi-lumen catheter ending in an actuated tip. The tip includes three main parts: a fixed base connected to the tether, a three bellows actuation system and a steerable distal element. Pressurizing air inside the bellows generates a bending of the distal part of the endoscope.

The control system consists of a continuum joystick structurally supported by a flexible central rod and three Nitinol wires placed around it and spaced 120° from each other. The Nitinol wires connect to the plunger of three syringes so that, when the user bends the joystick, the resulting displacement of the wires is transmitted to the plungers in this way pressurizing (or de-pressurizing) the air inside the syringes. The three syringes are connected to the multi-lumen catheter so that the pressurized fluid produces a change in length of the bellows.

The system was extensively tested in a stomach phantom and an in-vivo trial including both expert and non-expert users, with the aim to prove the intuitiveness of controlling the device and to compare the performance of the proposed solution with respecto to FE [94, 95]. Results showed that the Bellowscope was easy to manoeuvre resulting in a lower physical and mental demand when in comparison with FE.

1.5 Background Summary

Thanks to its diagnostic capabilities, conventional FE represents the gold-standard for the inspection of UGI tract. Nevertheless, some limitations exist and restrict the use of this technology, especially in LMIC where gastric cancer represents the leading cause of cancer related deaths. The portability of the platform, the cost associated with the equipment and the sterilization of the device preclude an effective use of standard FE in mass screening programmes.

Alternatives to FE exist and one of them is represented by capsule endoscopy. It has become increasingly attractive since its first use in 2000, but the passive movement of the capsule inside the GI tract does not provide the same diagnostic reliability of FE. For this reason, internally and externally actuated capsules have been developed. As internal actuation presents some limitations related to the limited on-board space, external actuation systems represent the most promising approach. Magnetically guided capsules have been largely explored to this end, however, they are still reliant on bulky and expensive equipment.

CMs have also been proposed as a solution to the problems related to wireless capsules such as the limited power provided by the battery. Given their intrinsic compliant nature they represent a safe alternative to the rigid robotics approach but, at the same time, they present a series of challenges still not completely addressed (e.g. manufacture, modelling and control).

The increasing interest in limiting the incidence of cancer in high-risk countries such as Japan, China and Korea or in rural areas, has led to an growing attention towards low-cost devices. The promise for a quality of diagnosis comparable to the one offered by FE, while remarkably reducing the cost of the procedure, represents the main driving force encouraging research in the field.

Chapter 2

A Water-Jet Actuated Continuum Manipulator for Ultra-Low-Cost Gastroscopy

Since its first appearance, the HJ low-cost gastroscopy platform underwent significant iterative development to attain a more capable and clinically appropriate design. In this chapter a detailed description of the HJ endoscope is presented. The chapter is organized into three main sections. Section 2.1 provide a comprehensive picture of the HJ platform state-of-the-art, describing the principle of operation and the characteristics of two design iterations of the endoscope. This section represents an introduction to the original work that this thesis describes, and aims at highlighting the limitations of the previously presented designs, with emphasis on the limited manoeuvrability of the HJ. Starting from the identified problems, Section 2.2 introduces a number of improvements in terms of design innovations, fabrication techniques and sensor equipment, finalized at enhancing the mobility of the endoscope and its range of motion. Ultimately, an extensive experimental evaluation of the proposed improvements is presented in Section 2.3, demonstrating the effectiveness of the adopted solutions.

2.1 The HydroJet: an Overview

The first prototype (HJ_{v1}, Figure 2.2a) of the HJ platform, introduced in [17], consists of a plastic capsule attached at the end of a flexible tether; with the tether connected to an external hydraulic control system.

The platform has, as essential features, a disposable capsule equipped with four nozzles spaced 90 deg apart around its body. These vent ports allow the

capsule to move as soon as pressurized water, flowing from the main hydraulic system, is ejected from them. With such a design, the nozzles behave as water powered thrusters, in this way allowing the capsule to move in the environment with two DoF in response to the generated reaction force. As in a standard FE, an additional degree of freedom is intrinsic in the system design and consists of adjusting the length of the tether that is inside the stomach by manually advancing or retracting it. Two supplementary ports on the capsule's body allow the operator to remove the excess of water from the stomach (suction lines). The disposable part of the system, consisting of the tether and the distal tip, contains the camera (64° FoV) and illumination modules. These components are sealed inside the capsule's outer shell and they do not come into contact with any contaminant fluid. As a result, the camera module and light source, representing the main items of cost, can be retrieved at the end of the gastroscopy procedure and reused without the need for sterilization. The capsule is attached to a multi channel tether. Each channel is an independent flexible tube that carries water from the main water tank to the capsule or from the capsule to an exhaust vessel in the case of suction lines. One last tube contains wires for the camera and LEDs. Each tube supplying water to the nozzles is connected to a solenoid valve that controls the amount of ejected water, this represents the fundamental control approach that grants the manipulability of the tether's tip. The hydraulic system, providing pressurized water to the capsule, includes a water tank, a pump, a flow-meter and a manifold. The pump collects water from the tank and pressurizes it in a high pressure hydraulic line. The pressurized water flows throughout a flow-meter and than it reaches the manifold which splits the main water flow into four streams. At this level, the valve control system modulates the flow-rate of the fluid reaching the nozzles. Using a joystick, and by relying on the camera feedback, the operator can control the valve opening levels, consequently controlling the capsule position in an open-loop fashion.

The proposed design was motivated by a number of technical, medical and safety requirements listed below:

- Size: the dimension of the device is crucial for two main reasons: (1) the insertion of the device through the esophagus (dimensions in Section 1.2.1) must be easy to perform and not cause discomfort to the patient; and (2) considering the worst case scenario, where the capsule detaches from the tether, its overall dimensions must allow the capsule to pass throughout the lower GI tract and to be expelled.

- Pressure: water pressure, measured at the exhaust port, must remain below

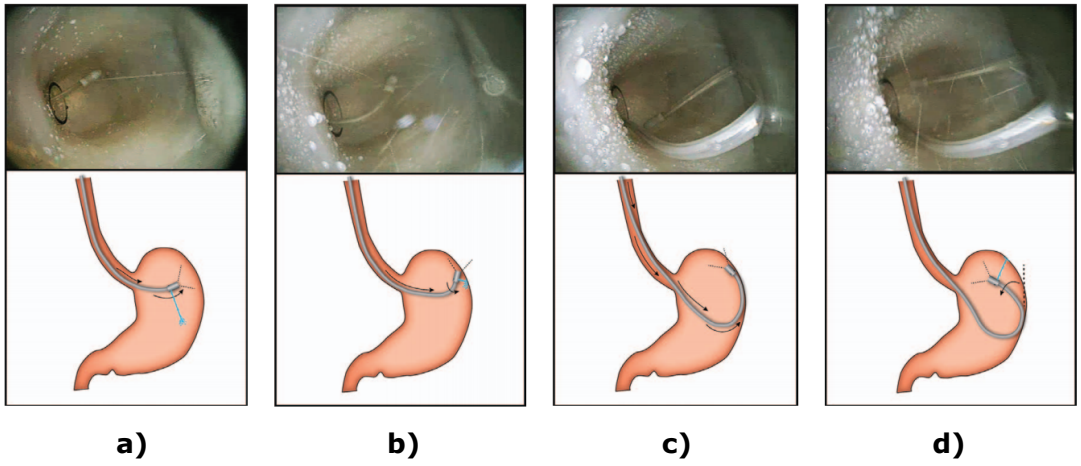

Figure 2.1: Push-to-Retroflex technique to achieve a full retroflexion of the endoscope's tip. The procedure consists of a) powering one of the water jets to achieve an initial bending of the tether, b) inserting the tether until the tip touches the stomach wall, c) continue pushing the tether to pivot the capsule and in d) a full retroflexion is accomplished. (©2017 IEEE) [16]

43.5 psi to avoid damage of the stomach mucosa, as identified in [96].

- Fluid volume: maximum amount of water in the stomach must remain below 1.3 L, in line with the practice adopted in [5].
- Cost per procedure: minimized by reusing electronic components (camera, LEDs).

Relying on these specifications, a 12 mm diameter, 28 mm long capsule was designed and attached to a 1.1 m long tether. The maximum achievable bending angle was less then 95 deg in an open-loop controlled experiment with a usable bending tether length of approximately 90 mm. To compensate for this lack of range of motion, the gastroscopy procedure, simulated in a explanted pig stomach, relied on the simultaneous tether introduction and capsule pivoting on the mucosal wall to visualize portions of the stomach that require a full retroflexion of the tether (Figure 2.1). The overall estimated cost of the platform was 6,000 USD with a cost per procedure in the range 2 - 5 USD.

In a second prototype of the HJ (HJ_{v2}) [16], a capsule with a smaller diameter (10 mm x 29 mm) was designed and the four nozzles were reduced to three, spaced 120 deg from each other (Figure 2.2b). Three nozzles represent the minimum number of actuators needed to maintain the same 2 DoF mobility of the endoscope and, at the same time, avoid the need for managing the action of two pairs of antagonistic jets. Moreover, the six, single channel, tubes were replaced with a more compact and easy to assemble multi-lumen tether.

The multi-lumen tether consists of seven channels, with six of them equally

spaced around the seventh central lumen. Three channels are used to carry pressurized water to the capsule, additional three are used for suction and the remaining one for wiring. This lumen arrangement guarantees an axial-symmetrical tether, in this way avoiding anisotropic bending behaviours.

The HJ control unit was adapted accordingly. The pump-based system was replaced in favour of a more reliable and stable pressurizing system: a compressed air tank that pressurizes the water tank. With this solution, no mechanically moving parts are required, resulting in a more fault-robust system. Finally, solenoid valves were replaced by pinch valves in order to prevent direct contact between water and the actuators, thus avoiding cross-contamination or corrosion.

Bench-top and stomach phantom trials showed a maximum bending angle of the endoscope tip of approximately 50 deg, using a tether length of 120 mm and an actuators pressure of 80 psi. During comparative trials with standard FE performed in a stomach phantom the lack of retroflexion capabilities reflected into a significant increase in the time-to-completion of the task. The full HJ system (excluding water and air tanks) was fit in a carry-on size suitcase, in this way proving its portability.

2.1.1 Limitations

In [17] and [16], preliminary version of a water jet powered low-cost endoscope were presented. Despite the characterization of the actuation system and a few design optimizations (e.g. multi-lumen tether, valve system), these platform versions presented a few limitations and missing features. Each of them is discussed below and summarized in Table 2.1. The table groups each issue/feature in three different areas (design, control and autonomy), in this way guiding through the development steps that, starting from the inherited platform described above, led to the current improved HJ system (HJ_{v4}).

From a design point of view, the main issue presented by HJ_{v1} and HJ_{v2} is related to their limited workspace. Such a constraint generates a number of disadvantages that prevent the HJ to reach the minimum requirements needed to be considered a valuable device from a gastric cancer diagnosis point of view. If on one side the introduction of the multi-lumen catheter allows for easier assembly and cheaper mass production, it is accountable for the difference in mobility seen between the first [17] and the second HJ prototype [16]. The ability of loose tubings to rearrange themselves to minimize the cross-sectional area, drastically reduces the stiffness of the tether and allows for wider tip bending angles using shorter tether length. In both the prototypes, the limited range of

motion, coupled with a limited FoV of the camera module, does not allow for a full retroflexion of the endoscope's tip nor for a full 180 deg range of view. Alternative solutions that compensate for these limitations are required.

As mentioned above, one of these alternatives consists of making use of the combined action of the water jets, insertion and the stomach wall to pivot the capsule and generate a retroflexion. This helps in expanding the range of motion but, at the same time, introduces different obstacles such as a longer time-to-completion of the task and the need for a skilled user and/or even experienced users to learn and adopt a new skills.

The instability observed in [17] at wide bending angle was not addressed and must also be taken into account when trying to widen the workspace.

An additional problem, sometimes a direct cause of instabilities, is to be found in the water flow-rate modulation method: wet solenoid valves, used in the first design revision, do not guarantee the retention of the valve's hygienic conditions after the procedure (e.g. back-flow of contaminated fluids); in the latest HJ prototype the problem is solved by using dry pinch valves: thanks to the physical separation between the mechanical/electrical components of the valve and the controlled fluid, contamination and corrosion can be avoided and at the end of the procedure the used tube can be easily removed and replaced with a new sterile one. In contrast, the mechanical design of such valve introduces some distinctive problems: the pinching action of the valve's gate damages the tube, often resulting in a permanent deformation or in a cut on the tube wall, both detrimental to the success of the gastroscopy. Finally, even if a successful insertion of the HJ endoscope was performed, a further miniaturization of the hard plastic components of the HJ could eliminate the need for an over-tube, decrease the patient discomfort and give the HJ more room to manoeuvre within the stomach.

Moreover, a wide FoV (above 100°), high resolution, small form-factor camera module would provide the physician with an image comparable to the one produced by FE and would expand the range of view of the device. A method for cleaning the camera lens or preventing water drops from obscuring the view is necessary when the endoscope is not operated underwater. In both a submerged and non-submerged scenario a suction line is required to remove the excess of water from the stomach.

As far as automatic control is concerned, to date (HJ_{v2}) none has been implemented and the endoscope's tip has been manually controlled by the user by directly acting on the valves. The implementation of open- or closed-loop automatic control schemes has the potential to make the endoscopic procedure as

simple as using a joystick. Furthermore, such an approach could pave the way to more advanced features such as the ability of the endoscope's tip to follow a user defined trajectory or an image based positioning system to intuitively move towards an abnormality identified on the mucosa. Closed-loop control approaches requires, as a minimum requirement, a measure of the controlled variable in order to be able to minimize the error between its current and desired value. A measure of the endoscope's tip position is thus needed, while taking into account other design constraints of size and cost.

A reliable design and robust control strategy still require the presence of a human-in-the-loop to issue high level commands. The introduction of autonomous or semi-autonomous behaviours represents the final step towards a device accessible to skilled and non-skilled users alike. Automatic inspection and abnormalities detection would require the user to be involved only during insertion or retrieval of the endoscope, thus achieving fully autonomous system capabilities. Automatic methods for the inspection of the GI tract have been proposed and rely on a vaiety of approaches allowing the endoscopic devices to safely and reliably navigate inside organs such as the stomach or colon [85, 97]. Moreover, it has been proven that the increased autonomy provided by these approaches not only allows for a decreased procedural time, but also for an improved user experience [85]. Automatically performing image-based diagnosis has the potential to move towards fully autonomous endoscopic procedures. AI based systems have shown high sensitivity and specificity in identifying and categorize precancerous (e.g. H. Pylori infections) or cancerous lesions using conventional imaging [98, 99, 100, 101]. Both real-time or off-line methods have demonstrated performances similar to the expert user while allowing for a faster detection rate [102, 103].

Below, the solutions adopted to mitigate the identified limitations of previous HJ versions (HJ_{v1} and HJ_{v2}), are described and experimentally tested to prove their effectiveness.

2.2 The HydroJet: an Improved System

In Figure 2.2 a timeline of the HJ design iterations is shown. The first two slots (a) anb b)) refer to the HJ prototypes developed in [17] and [16] respectively and extensively described in the previous section. The work described in this thesis starts after HJ_{v2}, when, taking into account the endoscope's drawbacks in matter of design features, a new prototype was created (HJ_{v3}). The main novelty, that

		Inherited HydroJet Platform	Target System Requirements
Design	Dimensions (rigid components)	Diameter: 10 mm Length: 29 mm	Diameter: 8 mm Length: 10 mm
	Workspace	Bending angle: 50° - 95° Camera FoV: 54° - 64° Overall: 77° - 127°	Overall: 180° (retroflexion)
	Portability	Proven in HJv1 and HJv2	
	Actuation	Sanitary Flow-Rate Control Tube Damaging	Sanitary Flow-Rate Control Stable Input/Output Characteristic
Control	Manual Control	Independent valve control or Joystick	
	Automatic Control	None	Trajectory Tracking
Autonomy	Environmental Perception	None	Obstacle Detection
	Exploration	None	Full Stomach Inspection

Table 2.1: Current system (HJ_{v1} and HJ_{v2}) vs. system requirements comparison.

distinguishes this implementation of the HJ endoscope from the previous ones, is the result of a new attention towards the continuum nature of the HJ. The focus moved from the endoscope's tip towards its tether, whose characteristics are responsible for the limited capabilities of the device. Starting from these well known problems, this section describes all the design and fabrication steps taken towards the goal of widening the HJ workspace and improve its stability.

2.2.1 Design

2.2.1.1 HJ_{v3}

The need for a lower bending stiffness and a narrower bending radius contrast with the necessity of a relatively high stiffness tether for insertion purposes. A new prototype was thus fabricated, implementing a non homogeneous ensoscope stiffness along its main longitudinal axis (Figure 2.2c). The tether consists of two principal sections: a multi-lumen catheter and a steerable segment. The multi-lumen tube represents the proximal part of the tether and connects the endoscope to the external control system. The steerable segment connects to the multi-lumen catheter on one end and to the capsule on the other. The hydraulic connection in between the two segments is achieved using a rigid plastic base connector fabricated by rapid prototyping (Clear V4 on Form 2, FormLabs, Somerville, MA, USA). The connector is equipped with barbed fittings to withstand the hydraulic pressure generated while operating the device. The

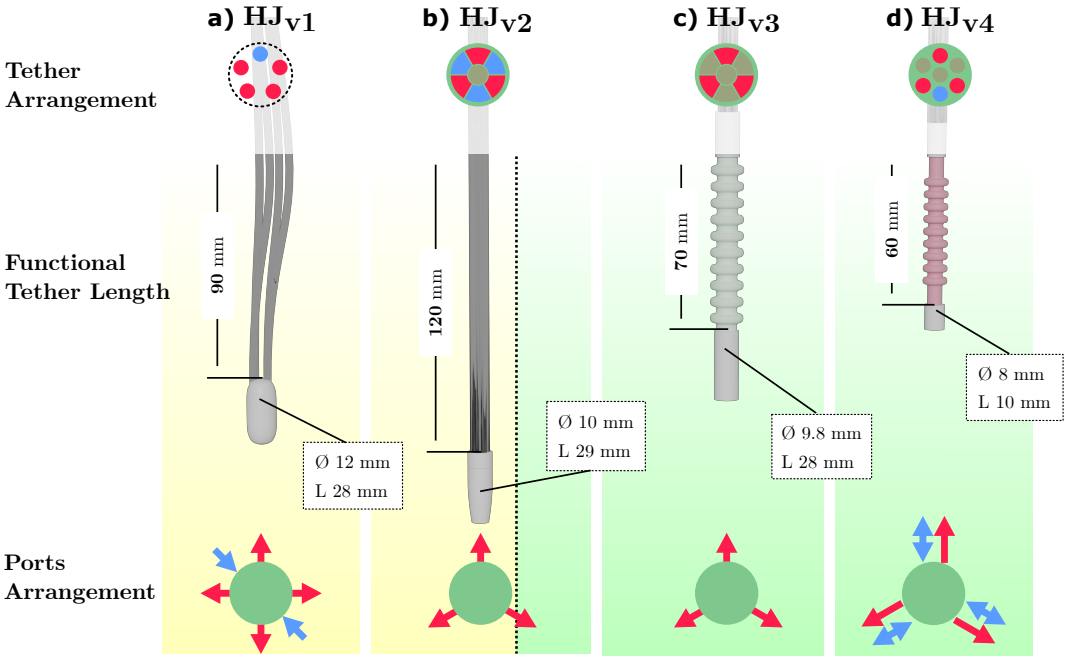

Figure 2.2: HydroJet design history: a) HJ_{v1} [17], b) HJ_{v2} [16], c) HJ_{v3} [18], d) HJ_{v4} current design. The dashed line in b) marks the starting point of the work described in this manuscript. Hydraulic and pneumatic (suction/insufflation) lines are color-coded using red and blue respectively.

steerable segment consists of two main components: three tubes carrying water from the multi-lumen tether to the tip, and an external protective sleeve. To meet the bending stiffness requirements, thin-walled tubings (35D Pebax 6fr - 0.008" wall, Apollo Medical Extrusions) were selected. Their constituent material allows them to withstand a relatively high pressure while their thin walls generate a minimal resistance to bending. An external corrugated custom sleeve (Ecoflex 00-30, Smooth-On, USA) protects the internal tubings and limits their relative movement while bending. This HJ revision, introduced for the first time in [18], was characterized by a 70 mm long steerable segment and a tip with an overall diameter and length of 9.8 mm and 28 mm respectively. The endoscope's distal section featured only one orientation sensor at the tip and one at the base, both for localization purposes; no camera, illumination modules or suction/insufflation ports where present.

2.2.1.2 HJ_{v4}

The improved design of HJ_{v3} and the promising results of the closed-loop control scheme presented in [18] led to an in-vivo trial on a porcine model (Yorkshire-Landrace pig) performed by an experienced GE. The trial highlighted how the combination of the very low-stiffness segment at the distal end of the tether

and the overall diameter of the endoscope cause difficulties during the insertion process. The GE was not able to reach the gastric cavity, also when an esophageal overtube was employed to ease the insertion procedure.

The need for further optimization led to the implementation of the final design revision (HJ_{v4}, Figure 2.2d) which includes the full set of functionalities embedded in the previous designs in a miniaturized capsule measuring 8 mm diameter by 10 mm in length and a 60 mm long steerable segment. The multi-lumen tether section of devices HJ_{v2} and HJ_{v3} was changed in favour of a more standard and reliable arrangement consisting of cylindrical channels and resulting in an overall 6.6 mm diameter tube (Nusil MED-4050, Della Medical Innovations, Dallas, TX, USA). The three nozzles, characterized by a diameter of 0.85 mm, are aligned with three suction/insufflation ports located in between the nozzles and the distal tip (Figure 2.4). When the gastroscopy is not performed underwater, the geometry and position of such ports generates an "air-shield" that prevent water droplets from depositing in front of the camera, thus obstructing the view.

The schematic of the overall updated system is shown in Figure 2.3. The pressurized water distribution system remains unchanged, with an air tank pressurizing a water vessel. The main hydraulic tube divides into three smaller lines, each of them passing through an ultrasonic flowmeter (Atrato Ultrasonic Flowmeter Model 760, Titan Flowmeters, UK) first, and an ECV (see Section 3 for details) after. Finally, the three lines connect to the multi-lumen tether. Electric wires powering the on-board electronics, run from the tip along the full endoscope length reaching the sensor hub (BeagleBoneBlack, BeagleBoard.org Foundation, MI, USA) and camera processor (Fujikura, Tokyo, Japan). An additional tether channel is used as suction/insufflation line while the central lumen is dedicated to optional sensor equipment such as a magnetic tracker probe. A ROS-based network architecture connects all the above mentioned components to the main controller where a user interface is executed.

2.2.2 Sensing

In Figure 2.4 a close-up of the steerable segment is shown. The capsule contains a miniaturized camera module (CameraCubeChip, OmniVision, USA) measuring 1 x 1 x 3 mm with a resolution of 400 x 400 pixels and a FoV of 120°. A custom 4 LEDs illumination unit (LXZ2-2790-3, Lumileds, Netherlands) provide the necessary light to the scene. LEDs and the camera module are soldered on the same custom, 7 mm in diameter, PCB. This arrangement makes necessary for the CMOS sensor to be "shielded" from the radiations coming from the LEDs

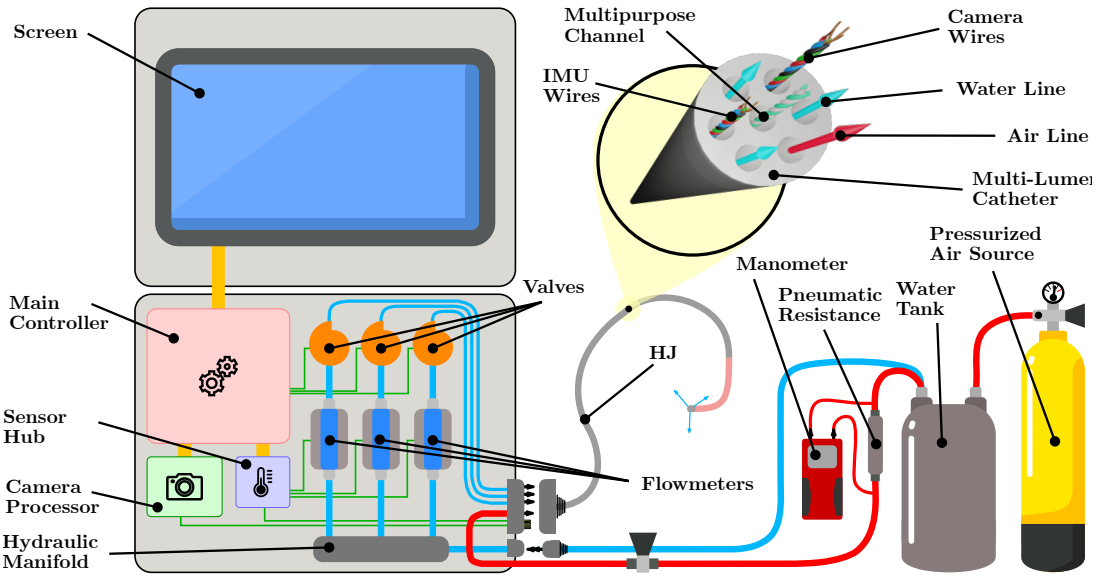

Figure 2.3: Schematic of the HydroJet system including the control system fitted in a carry-on size suitcase, the endoscope, the pneumatic (red) and hydraulic (blue) lines and a section of the multi-lumen tether.

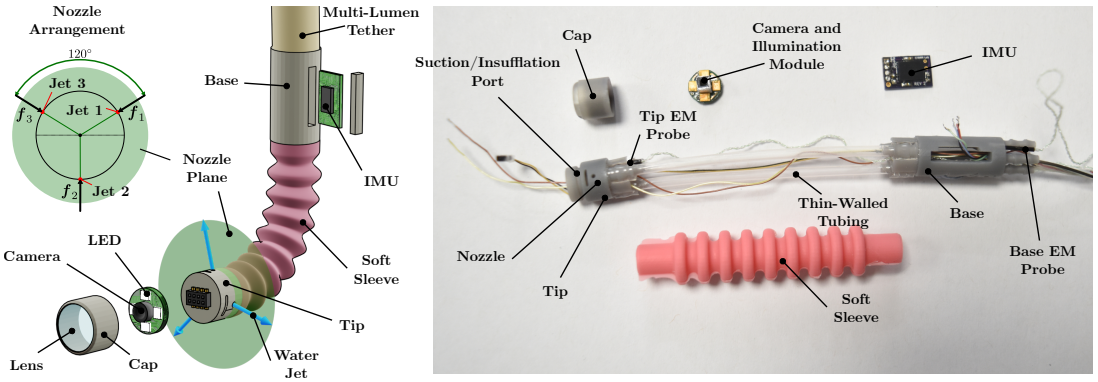

Figure 2.4: The HydroJet steerable segment exploded views, revealing the thin-walled tubes arrangement, sensors equipment, water and air ports disposition.

nearby, in this way preventing glare on the resulting image feedback. This is accomplished by enclosing the camera module in a thin layer of reflective material, such as aluminium tape (Tesa 60630, Tesa, Germany). The base connector at the interface between the multi-lumen tether and the steerable segment contains a custom inertial measurement unit (BNO-055, Bosch Sensortec, Germany) module, running a proprietary sensor fusion algorithm and providing the absolute orientation of the base, or its orientation with respect to the gravity vector. Accessory sensory equipment includes two 6-DoF electromagnetic probes (Aurora Electromagnetic Tracking System, Northern Digital Incorporated, Canada), one at the tip and one at the base, used as ground truth for testing and validation purposes.

2.2.3 Fabrication

Excluding off-the-shelf components (e.g. thin-walled tubing) and custom made parts outsourced to specialized companies (e.g. multi-lumen extrusion), the remaining components are produced using rapid prototyping techniques. All the hard plastic components (e.g. base connector and tip module) are fabricated using a stereolitography 3D printing method (Grey V4 on Form 2, FormLabs, Somerville, MA, USA) generating, at the same time, well defined features (e.g. circular nozzles) and internal channels free from obstructions. The soft external sleeve is fabricated using injection molding techniques, allowing for a virtually infinite number of copies of the same object to be generated inexpensivelly and always with constant geometric characteristics. Figure 2.5 describe the fabrication process in its most important steps. The mold consists of two 3D printed mirrored parts (Grey V4 on Form 2, FormLabs, Somerville, MA, USA), reproducing the external geometry of the sleeve, and a third component (here referred to as insert) which allows creation of the hollow structure. Before the mold is assembled, a preparation step involves the deposition of a thin coating layer of lacquer that will prevent the mold to come into contact with the liquid polymer causing the inhibition of the curing process [55]. The mold is then assembled: the insert aligns to the mold using two aligning discs while the alignment of the two halves is guaranteed by a series of corresponding pins/holes. The two halves are clamped together and the liquid polymer, previously mixed and degassed in a vacuum mixer (ARV-310 Planetary Centrifugal Vacuum Mixer, Thinky, Tokyo, Japan), is injected using a disposable syringe, filling the cavities from the bottom to the top of the mold in order to avoid the creation of air pockets. The injection ends when the polymer gets ejected from the venting port and fills the reservoir. The reservoir at the top of the mold allows for the excess of liquid polymer to replace potential air bubbles trapped inside the mold and released over time. The finishing steps involve a de-molding process where the part is removed from the cavities, a cleaning process aimed at eliminating the sprue and a peeling process that removes the insert thus returning the hollow sleeve. The final sleeve produced with this method is shown in Figure 2.4

2.3 Evaluation

A device, featuring the above mentioned design characteristics (Section 2.2), was tested with the specific goal of assessing the enhanced mobility of the HJ. A successful outcome includes a wide bending angle positioning (e.g. 120 deg)

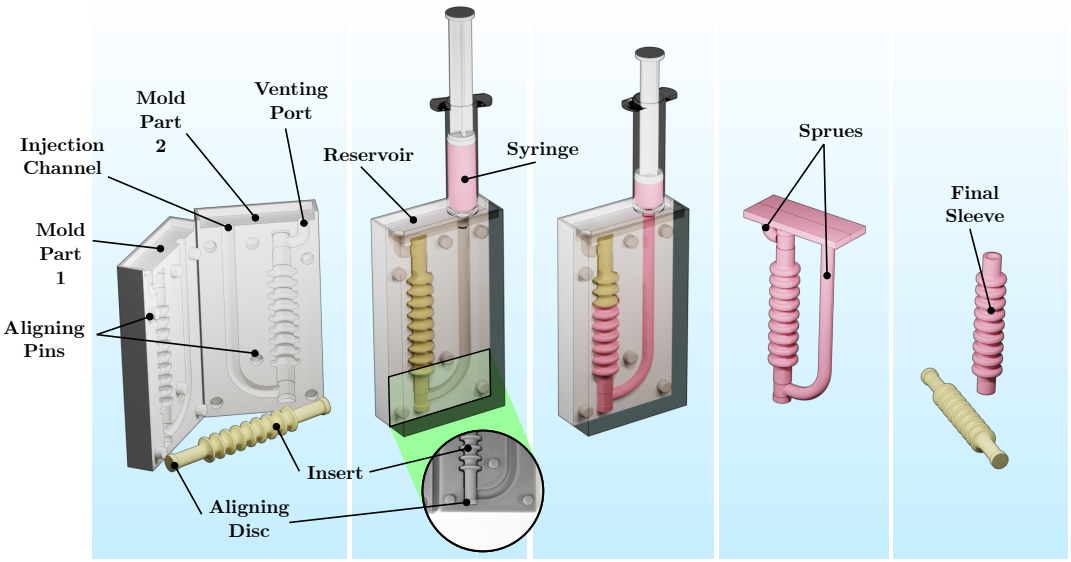

Figure 2.5: The HydroJet soft sleeve fabrication process through injection molding.

of the endoscope's tip while avoiding instabilities or oscillations thus achieving a steady visualization of hypothetical abnormalities on the stomach wall.

2.3.1 Force Estimation

Jet forces were evaluated by mounting the HJ tip rigidly onto a cantilever structure. A load-cell (ATI Nano 17, ATI Industrial Automation, NC, USA) was rigidly connected to the base of the cantilever to allow measurement of the produced jet force. The cantilever was constructed from an aluminium rod and was aligned along the force sensor's z-axis for the experiment. Such as arrangement, allows to move the sensing unit away from the jets of water, and at the same time, amplifies the measurement quality by relying on torque data instead of direct force measurement. The HJ tip was attached to the free end of the cantilever with the main longitudinal axis parallel to the aluminium rod and one of the nozzle radially facing. The load-cell is connected to a CompactDAQ (National Instruments Corp., Austin, Texas, USA) running a custom LabVIEW program: the sensor was calibrated and possible offsets removed before starting the registration. The test consisted of a single jet actuation: the corresponding valve was completely opened and then fully closed, while torque and flow-rate data were registered. Three different nozzle geometries were tested to understand which design would allow the maximum generated thrust. All the tested nozzles had a circular shape with diameter increasing from 0.70 mm, as in [18], to 1 mm using 150 μm steps. The chosen step size is a direct consequence of the resolution provided by the fabrication process: even if the minimum printable layer

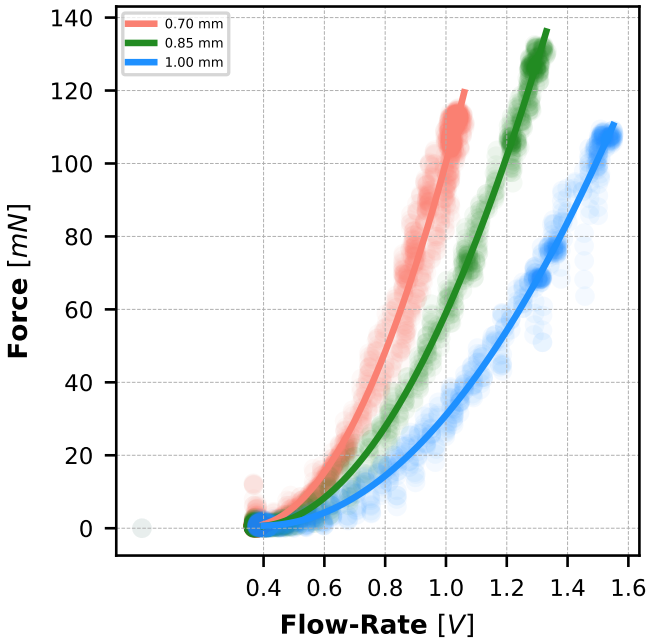

Figure 2.6: Flow-rate vs. generated force characteristics corresponding to three nozzle geometries with diameters 0.7 mm, 0.85 mm and 1.00 mm. The graph shows a 2^{nd} order polynomial regression model (solid line) that fits the experimental data (shaded points) for each nozzle geometry.

thickness measures 25 μm, the laser spot of the available SLA (StereoLithography Apparatus) printer has an overall diameter of about 140 μm that dictates the minimum achievable feature size. The jet thrust is thus evaluated using the torque sensor readings and the tip distance from the load-cell along its z-axis (cantilever arm, 339 mm). Results are shown in Figure 2.6.

The measured force output is shown as a function of the flow-rate and the raw data are fit with a second order polynomial function. Flow-rate values are expressed in voltage representing the raw flowmeter's output proportional to the flow-rate and offset by approximately 400mV (0.4 V = 0 L/min). The graph clearly shows that, at a given pressure, the 0.85 mm diameter nozzle outperforms the other two geometries in terms of maximum achievable thrust even if at a higher flow-rate regime with respect to the 0.70 mm diameter nozzle. For safety purposes, the pressure generated by the nozzles was also estimated: the maximum generated force was 0.1160, 0.1326 and 0.1095 N for 0.70, 0.85 and 1 mm respectively, resulting in a maximum pressure of 3.01, 2.33 and 1.17 bar. For these reasons the 0.85 mm nozzle diameter was selected and used for the following tests.

The need for an pneumatic line to reach the HJ tip for suction/insufflation and shielding purposes, introduces a new design variable: how does the air reach the

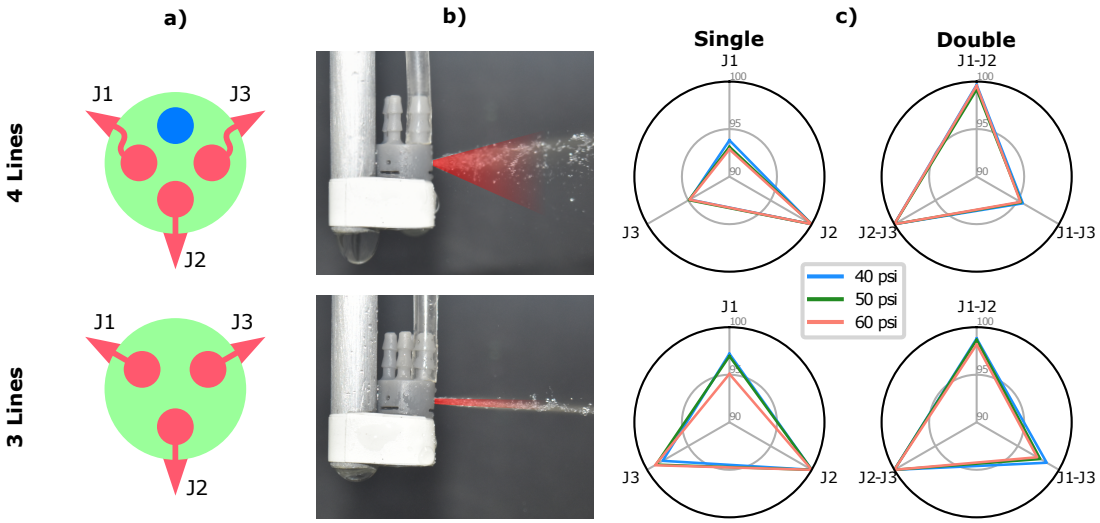

Figure 2.7: Jets output evaluation: a) barbed fittings and nozzles relative arrangement, b) water-jet shape and c) achieved output expressed as the ratio between the i-*th* jet flow-rate and the maximum registered flow-rate.

tip of the endoscope? Two possible solution were explored: adding an additional thin-walled tube to the three already used to carry pressurized water (4L) and make use of the soft sleeve to convey air throughout the steerable segment (3L). Both the solutions have advantages and disadvantages, however, in this section, their performance is evaluated exclusively in terms of jet's output (e.g. flow-rate or force).

When an additional pneumatic line is introduced, the capsule design requires a number of updates aimed at accommodating a fourth barbed fitting. This, in turns, means spacing the four barbed fittings 90 deg from each other (instead of 120 deg) and redirect the path of, at least, two channels to account for the 120 deg spacing of the nozzles (Figure 2.7a). On the other hand, the second option does not require major design changes, but only the ability of the soft sleeve to withstand the air pressure and to achieve an airtight fit with the tip and base bodies.

The response of the two designs to the actuation of one jet (single jet) and two coupled jets (double jet) was investigated, measuring the maximum flow-rate at three different system pressures: 40, 50 and 60 psi. The results are shown in Figure 2.7. From a first visual assessment it is clear how in 4L the new twisted channels (J_1 and J_3 in Figure 2.7a and b) introduce flow recirculation leading to an unfocused jet shape. This does not happen for J_2 and for all the jets in the 3L configuration, where the jet stream remains coherent. The consequences of an incoherent jet are visible in Figure 2.7c. In 4L the maximum flow-rate generated by J_1 and J_3 reaches about 93% of the maximum output generated

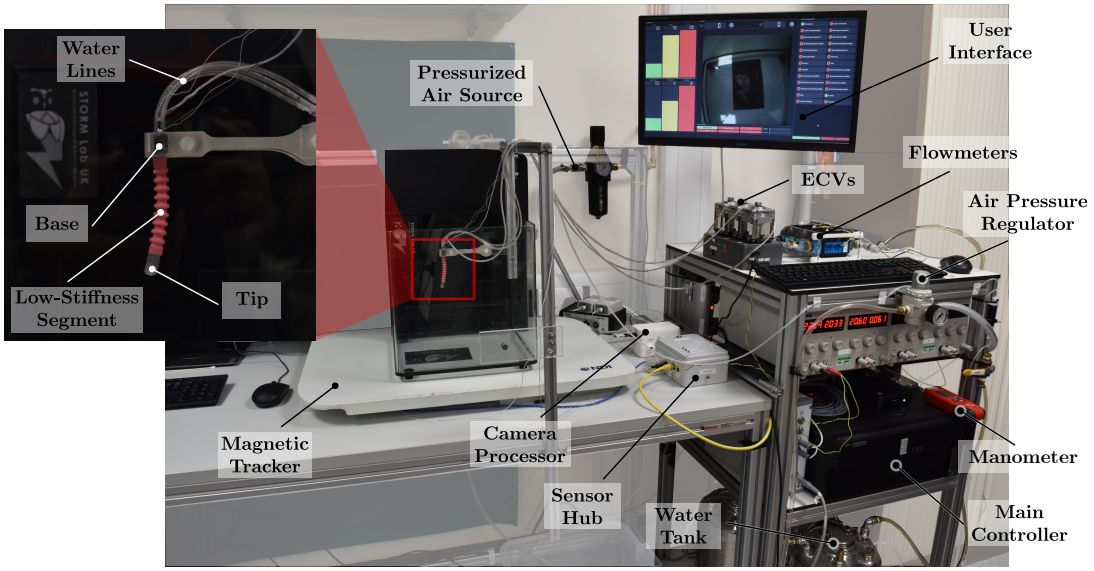

Figure 2.8: Laboratory HydroJet set-up.

by J_2. Moreover, the conical shaped water stream produces thrust components parallel to the capsule longitudinal axis, unable to generate a displacement of the tip. A more homogeneous output for all the jets was achieved in 3L. The output drop seen only for J_1, that also affects $J_1 J_x$, can be attributable to the channels shape in the base connector: here, a non-straight path of the internal channels is required to make room for the Inertial Measurement Unit (IMU) module.

2.3.2 Workspace Evaluation

To prove the enhanced mobility of the HJ tip provided by the introduction of the steerable segment, an experiment was performed including multiple design factors: the overall amount of pneumatic/hydraulic lines (3L or 4L), the geometric properties of two different types of tubing (0.005" and 0.008" wall thickness, referred to as 5WT and 8WT respectively) and the activation status of the pneumatic line (ON or OFF). The experimental set-up used for this experiment is presented in Figure 2.8. The test rig, which includes the aforementioned equipment (Section 2.2), features a pressurized air line connected to the HJ endoscope. The air flow is kept constant across all the repetitions thanks to a user-operated valve and a digital manometer reading the pressure drop across a constant pneumatic resistance.

The experiment aims at identifying the HJ design choices that maximize the bending angle, while guaranteeing stable positioning of the tip. A single and double jet propulsion test was performed starting from the HJ rest position (base and tip longitudinal axis aligned with the gravity vector) and using the

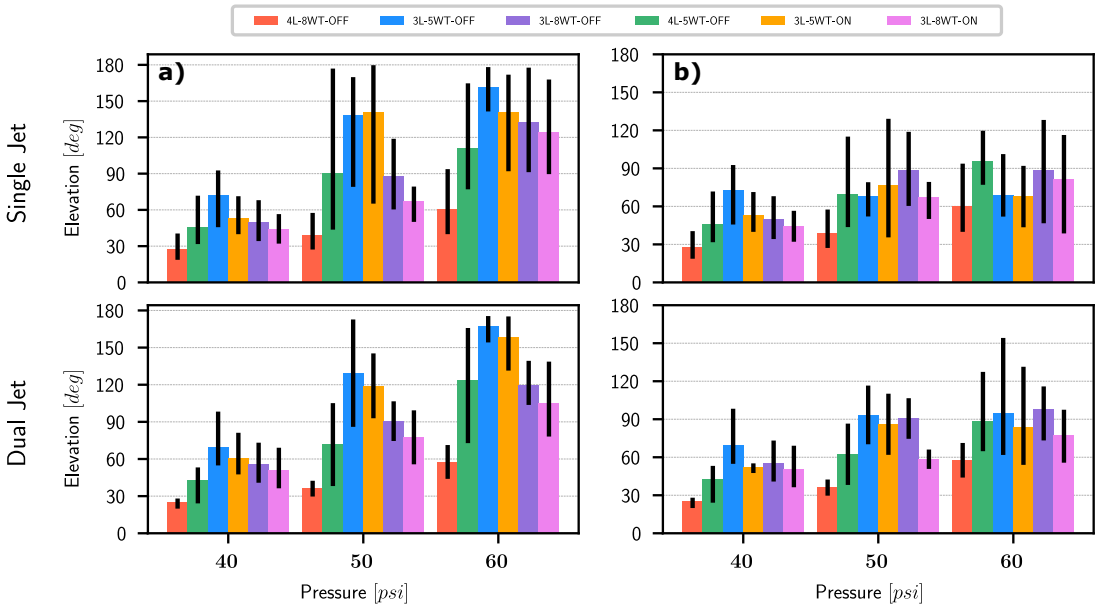

Figure 2.9: Single- and double-jet driven bending test showing the tip a) maximum achievable elevation and b) maximum stable elevation before the kinking event occurs. The coloured bars indicate the average elevation, while the black bars refers to the maximum and minimum ϑ registered during the test.

actuation series $J_1 \Rightarrow J_2 \Rightarrow J_3 \Rightarrow J_1J_2 \Rightarrow J_2J_3 \Rightarrow J_1J_3$, each time activating the corresponding valves with an ascending and descending ramp signal. Six different HJ devices were fabricated, varying the aforementioned design variables, and each of them was tested at 40, 50 and 60 psi. The soft sleeve was fabricated using a silicone compound (Ecoflex 00-30, Smooth-On, USA) and its radial deformation, due to compressed air, was constrained using metallic rings placed in the sleeve's creases. The results are shown in Figure 2.9 and summarized in Table 2.2.

A minimum acceptable bending value of 120 deg was identified considering that, combined with half of the camera FoV, it provides a 180° range of view. The pose of the tip and base were measured using the Electro-Magnetic (EM) probe and the elevation of the tip ϑ was evaluated as the angle measured between the base and the tip longitudinal axis, so that $\vartheta = 0$ at rest. Figure 2.9a shows that, predictably, lower stiffness devices (e.g. 3L-5WT) reach, on average, the 120 deg threshold, even at a pressure of 50 psi, while stiffer devices (e.g. 4L-8WT) remain below it. In Figure 2.9b, the same results are shown in terms of maximum stable elevation, intended as the maximum value of ϑ before the onset of an unstable behaviour of the tip. This is identified in the elevation data as a spike in the signal $\Delta\vartheta/\Delta t$. When the stability factor is considered, all the devices remain below the acceptable elevation threshold.

The causes of such an unstable behaviour, that occurs after a certain elevation

		Maximum Elevation [deg]			Maximum Stable Elevation [deg]		
		40	50	60	40	50	60
Single Jet	4L-8WT-OFF	27 (36 - 14)	38 (50 - 20)	60 (81 - 27)	27 (36 - 14)	38 (50 - 20)	60 (81 - 27)
	4L-5WT-OFF	45 (60 - 19)	90 (137 - 4)	111 (145 - 57)	45 (60 - 19)	69 (96 - 24)	96 (115 - 72)
	3L-5WT-OFF	72 (99 - 52)	138 (198 - 107)	161 (182 - 145)	72 (99 - 52)	68 (84 - 57)	69 (86 - 37)
	3L-5WT-ON	53 (66 - 34)	141 (216 - 102)	141 (190 - 110)	53 (66 - 34)	76 (117 - 24)	67 (92 - 43)
	3L-8WT-OFF	49 (64 - 31)	88 (116 - 57)	132 (173 - 87)	49 (64 - 31)	88 (116 - 57)	88 (130 - 49)
	3L-8WT-ON	44 (56 - 31)	67 (85 - 55)	124 (159 - 81)	44 (56 - 31)	67 (85 - 55)	81 (124 - 46)
Dual Jet	4L-8WT-OFF	25 (30 - 22)	36 (42 - 31)	57 (71 - 43)	25 (30 - 22)	36 (42 - 31)	57 (71 - 43)
	4L-5WT-OFF	42 (61 - 32)	71 (105 - 45)	123 (175 - 82)	42 (61 - 32)	62 (86 - 46)	88 (111 - 49)
	3L-5WT-OFF	69 (84 - 40)	129 (172 - 83)	166 (179 - 158)	69 (84 - 40)	93 (116 - 62)	95 (128 - 35)
	3L-5WT-ON	60 (73 - 40)	119 (145 - 70)	158 (185 - 141)	52 (56 - 48)	86 (110 - 43)	84 (114 - 36)
	3L-8WT-OFF	55 (70 - 38)	90 (106 - 66)	119 (135 - 99)	55 (70 - 38)	90 (106 - 66)	97 (121 - 79)
	3L-8WT-ON	50 (64 - 32)	77 (99 - 47)	104 (131 - 70)	50 (64 - 32)	58 (66 - 48)	77 (98 - 56)

Table 2.2: Single- and double-jet driven bending test results indicating the average (maximum - minimum) achieved elevation ϑ registered during the tests performed at 40, 50 and 60 psi.

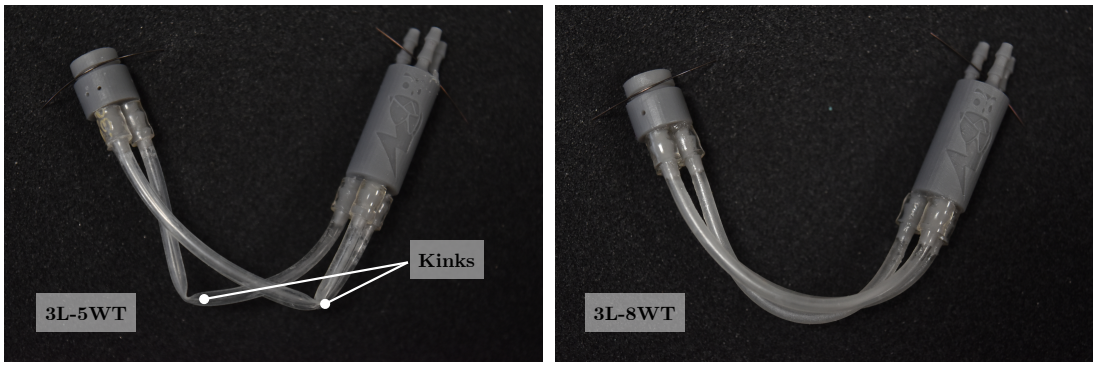

Figure 2.10: Tubes kinking for two of the fabricated devices 3L-5WT and 3L-8WT

angle, are ascribable to a tube kinking event (Figure 2.10). When one or multiple tubes kink, an instantaneous drop in the tether stiffness is experienced. This causes a dramatic increase in the bending angle at first. Then, the kink restricts the water flow-rate causing a drop in the generated jet force, which brings the tip back to lower elevation angles. If, at this point, the flow-rate is not restricted by the valve, a self-sustaining oscillation results with the tip moving in between these two states.

The experiments clarify how the compressed air inside the soft sleeve stiffens the structure, thinner-walled tubing allow to reach elevation in the desired range eventually leading to instability and, finally, thicker-walled tubing guarantee stability at elevations below the desired minimum value.

The high elevations reached by 3L-5WT-X devices were identified as the most promising in terms of range of motion in spite of the limiting factor represented by the kinking. For this reason, in the attempt to test the possibility of "masking" the kinking event in 3L-5WT-X, one additional device was fabricated using a soft sleeve made of a stiffer (A-30) constituent material (S-30, Polycraft, MB

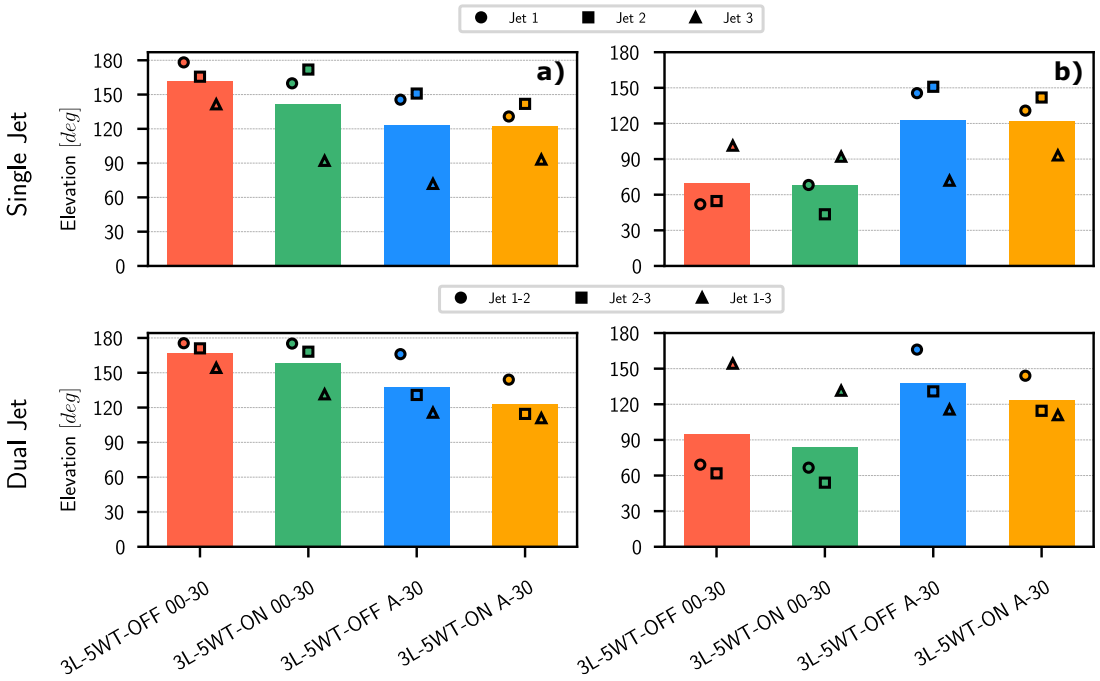

Figure 2.11: Single- and double-jet driven bending test showing the tip a) maximum achievable elevation and b) maximum stable elevation before the kinking event occurs. The coloured bars indicate the average elevation, while the coloured markers refers to the maximum ϑ registered for each jet or combination of jets.

Fiberglass, UK). The founding idea is for the outer sleeve to be the predominant factor determining the shape of the bending section, in this way reducing the effect of possible kinking of the internal tubing. The testing procedure remains unchanged and the results, shown in Figure 2.11 and summarized in Table 2.3, are compared with the ones collected for 3L-5WT-X.

The bars show that, despite the increased stiffness restricting the maximum achievable elevation, 3L-5WT-x-A30 is capable of stable positioning at elevations higher than the predetermined threshold. The stiffer sleeve is able to mask the kinking event, in this way avoiding discontinuities in the tether curvature, while

		Maximum Elevation [deg]	Maximum Stable Elevation [deg]
Single Jet	3L-5WT-OFF 00-30	161 (141 - 178)	69 (51 - 101)
	3L-5WT-ON 00-30	141 (91 - 171)	67 (43 - 91)
	3L-5WT-OFF A-30	122 (71 - 150)	122 (71 - 150)
	3L-5WT-ON A-30	121 (93 - 141)	121 (93 - 141)
Dual Jet	3L-5WT-OFF 00-30	166 (158 - 179)	95 (35 - 128)
	3L-5WT-ON 00-30	158 (141 - 185)	84 (36 - 114)
	3L-5WT-OFF A-30	137 (108 - 159)	137 (108 - 159)
	3L-5WT-ON A-30	123 (102 - 135)	123 (102 - 135)

Table 2.3: Single- and double-jet driven bending test results indicating the average (maximum - minimum) achieved elevation ϑ registered during the tests.

easily withstanding the air pressure without any major deformation or the need for restraining rings.

2.4 Discussion

The augmented HJ tip mobility, as a direct result of the introduction of a low-stiffness steerable segment at the distal end of the HJ tether, and the enhanced tip stability brought by a corrugated soft sleeve, represent the main achievements described in this chapter. The design of the HJ restricts the deformation of tether exclusively to the bending section. Its self-contained longitudinal dimension, compared to previous HJ devices, results in a reduced bending radius and, as a direct consequence, in an increased clearance when operated in a confined space such as the gastric cavity. A lower stiffness of the steerable segment was achieved using a minimum number of loose thin-walled tubes, while maintaining the suction/insufflation capabilities without adding complexity to the system. The selection of a stiffer constituent material for the outer protective sleeve guaranteed a stable positioning of the endoscope tip above the desired elevation of 120 deg. The amplified range of motion, coupled with a wider FoV of the camera module, generate an overall range of view of more than 180°, in this way enabling the visualization of landmarks such as Fundus and Cardia, without the need to actuate the third DoF. A nozzle gauge of 0.85 mm was selected as the most advantageous in terms of generated thrust and safety of the jet.

2.5 Conclusions

A novel design for a water-jet actuated continuum endoscopic device has been presented and fabricated. With respect to previously published works, the presented device overcomes the obstacles represented by its dimensions, limited workspace and tip instability, while maintaining the distinctive characteristics of a single-use and low-cost device. The introduction of a soft bending segment allowed for an unprecedented range of motion of the endoscope's tip (up to 74% and 232% increase with respect to HJ_{v1} and HJ_{v2} respectively), even if regions of tip instability have been identified. The kinking of the internal thin-walled tubing has been identified has the main cause of such unstable behaviour, and it has been mitigated by exploiting different constituent materials for the fabrication of the outer soft sleeve. Extensive testing of the possible combinations of tubes geometry and sleeve stiffness resulted in a device that meets the predefined range

of motion and stability requirements (stable positioning at a maximum bending angle of 137 deg). The implementation of such augmented capabilities represents a milestone for the HJ endoscopic system and its employment in screening programmes as valuable and reliable equipment.

Chapter 3

Sanitary Control of Fluid Driven Actuators Using an Eccentric Compression Valve

Supplementary material at https://doi.org/10.1109/TMECH.2019.2960308

3.1 Introduction

The concepts of precision and accuracy are central in the field of robotics. The ability of a robot to generate reproducible and exact motions depends on the performance of its actuators; whether electromechanical, pneumatic or hydraulic in nature. In these latter cases, precise introduction of pressurized fluid is fundamental in facilitating reliable high resolution actuator control for many applications. For example, soft robotic systems based on the construct of pressure driven hyper-elastic materials (e.g. silicone) generate a kinetic response that depends directly on fluid control coupled with the robot's geometry and material properties [105]. Research into soft robot based applications for augmenting the capabilities of traditional robots [106] and for environmental exploration [107, 108, 109] is common, however, one of the most prevalent areas of interest for soft robotics is within medical applications [76]. Devices have been developed for Minimally Invasive Surgery (MIS) [110], endoscopy [16], heart assistance [111] and rehabilitation [112].

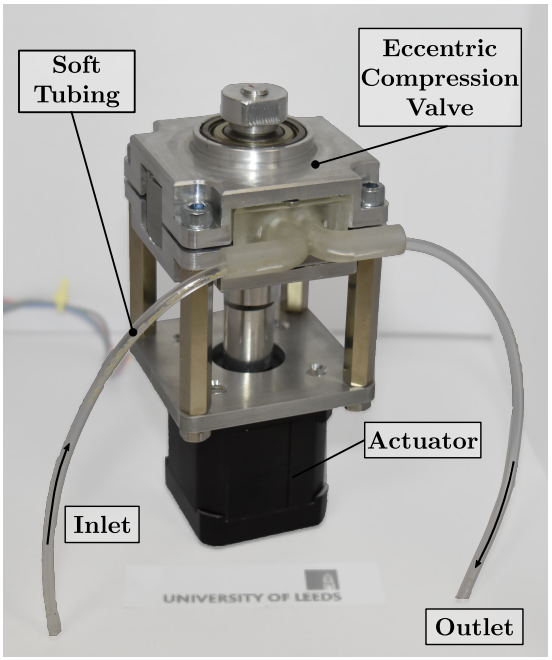

Figure 3.1: Assembled eccentric compression valve showing the sanitary valve inlet and outlet, the soft tubing, the valve core and actuator. ©2020 IEEE

For medical use cases, such as those exampled, consideration of patient safety during interaction with the device materials and drive system is crucial. Although regulation of fluids through in-line valve systems (e.g. gate valves, needle valves, etc) can offer technically effective solutions, they require direct interaction with the working fluid. This adds to contamination risks either from the valve directly (i.e. corrosion), or cross-contamination of patients (i.e. back-flow). Therefore, such in-line systems must be disposable or be subject to reprocessing protocols that increase the cost and downtime of the device [113].

Pressure or flow regulation devices that are physically separate from the transmission fluid offer a more appropriate solution for medical applications. Examples include pinch valves [114, 115] and peristaltic pumps [116] used for sanitary applications such as dosage regulation and blood analysis or infusion. Pinch valves work by applying a load normally to pre-pressurized tubing through a "pinch-point" plunger; thus reducing the cross-sectional area of the tube locally and consequently the flow-rate. This flow regulation approach generates a high level of stress on the soft tubing leading damage and ultimately altering the flow characteristics of the system over time [116]. Peristaltic pumps induce pressure in the line through successive simultaneous squeezing and shearing actions. In this case, the output flow generated by the pump is highly pulsatile, which is undesirable if a fine control of the pressure/flow needs to be achieved. This behaviour can be attenuated by introducing an inline pulsation damper [117], al-

though this adds complexity and cost to the system. These issues, when coupled with poor resolution in flow-rate control and hysteresis, make them unsuitable for applications such as medical actuators that require great precision. Therefore, there is a need for sanitary pressure and flow regulation devices that deliver safe and precise flow control.

This chapter presents a novel sanitary Eccentric Compression Valve (ECV) that allows indirect precise flow regulation in pre-pressurized systems. The ECV, presented in Figure 3.1, uses an eccentric mechanism to compress the tubing over a wider contact area against a tunable spiral shaped profile, thereby minimizing local stresses and the associated tube damage. An optimization step is presented that allows for the geometry of the device to be easily adapted to suit the components and constraints of a wide range of applications. The method applies to the mechanical design of the valve rather than on its electronic controller to produce improved resolution and linearity with respect to commercially available sanitary solutions.

The presented work evaluates our novel ECV performance against standard pinch valves in terms of volumetric flow-rate characteristics over repeated actuation cycles. For the purpose of this manuscript, the valve efficacy was demonstrated by using an optimized ECV to control the HJ medical device. Comparison of the ECV relative to pinch and solenoid valves under cyclic actuation of the HJ is presented and highlights improved flow-rate tracking and reduced flow-rate fluctuation.

3.2 Principle of Operation

The proposed valve adopts a combination of custom components to deliver a gradually increasing distributed load onto standard flexible tubing carrying a pressurized fluid. The design is comprised of two main parts, as shown in Figure 3.2a: (1) a passive compression component (valve housing) that includes a spiral compression profile encoded into its wall; and (2) an active compression component with eccentric geometry (eccentric drive shaft and compression bearing). Flexible tubing sits between these two components and is compressed between the bearing and the compression profile. Through the use of a bearing, shear forces induced by the relative motion between the rotating drive shaft and the flexible tube are minimized ensuring compressive forces remain normal to the tubing cross-section. Relative motion between the active and passive components therefore, results in varied occlusion of the flexible tubing and hence

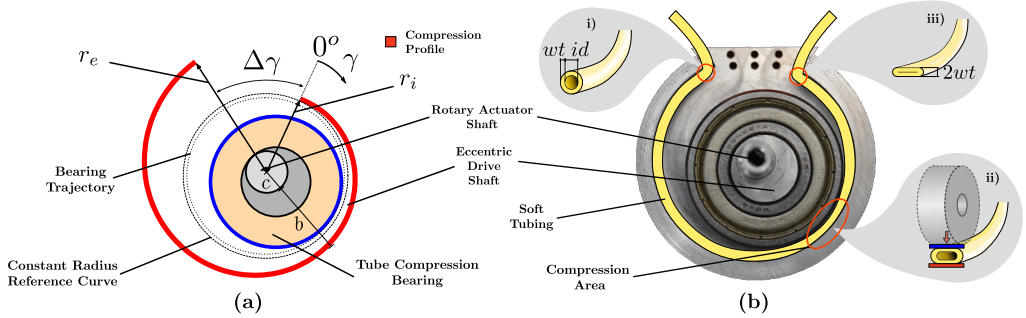

Figure 3.2: Example compression profile: showing (a) a design with a linearly varying compression profile (exaggerated for clarity), and (b) a schematic representation of tube compression at three locations along the profile, with: i) no occlusion - maximum flow, (ii) moderate occlusion - intermediate flow, and (iii) completely occluded - no flow. ©2020 IEEE

alters the volumetric flow-rate of the fluid (Figure 3.2b). The level of compression depends on the rotation angle of the rotary actuator shaft with respect to the tube housing. In the general case, the compression profile radius r may be expressed as a function of an angle γ, evaluated across an angular range, γ_i to γ_e, as:

$$r(\gamma) \quad \{\gamma \,|\, \gamma_i \leq \gamma \leq \gamma_e\}\,. \tag{3.1}$$

The choice of $r(\gamma)$ and tube size are application dependent, and may be interchanged while maintaining the same active compression components. For the example case presented in Figure 3.2, an Archimedean spiral of the form $r = r_i + k\gamma$ has been used to generate a linearly varying compression profile as a function of angular position, where r_i and k represent the initial compression radius and its angular rate of variation, respectively.

The spiral parameters r_i and k can be evaluated by considering the bearing eccentricity (c), the bearing radius (b), the geometry of the flexible tubing (e.g. tube inner diameter (id) and wall thickness (wt)), and the working angular range (γ_e - γ_i); allowing for suitable tubing access into and out of the housing.

With a desired profile selected, the components of the valve may be assembled from a combination of off-the-shelf components (e.g. ball bearings and drive motor), machined parts (e.g. upper and lower casing, tube housing, drive shaft, etc), and parts produced with additive manufacturing (e.g. tube feeder and tube guide), as illustrated in Figure 3.3. This approach delivers a flexible design for accommodating different application requirements, for example: tube sizing, machining resolution, drive torque, actuation speed, and positional resolution.

In addition to being scalable to different applications, the mechanical de-

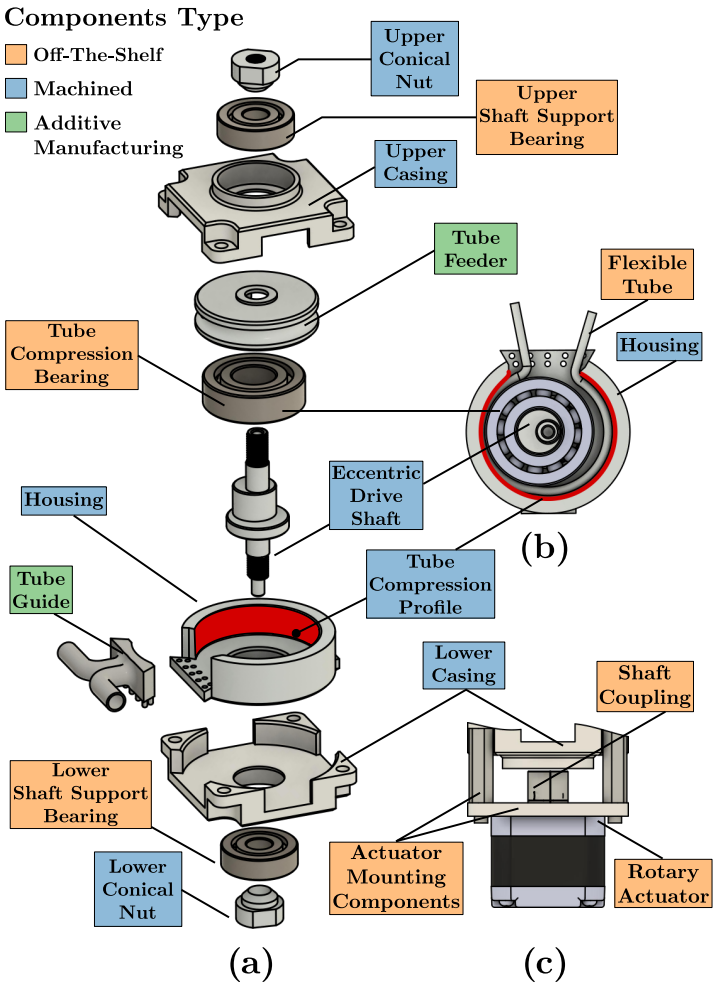

Figure 3.3: Sanitary ECV design, showing: (a) exploded view of the valve housing assembly; (b) the active and passive components acting to compress the tubing; and (c) the rotary actuator and its coupling to the housing assembly. ©2020 IEEE

sign of the valve intrinsically limits the maximum stress that can be applied on the flexible tube since the gap between active and passive pinching components is fixed, never falling below a pre-designed threshold. This will increase the longevity of the tubing and reduce the influence of damage on the output flow characteristics. As an example, a minimum closing threshold equal to twice the wall thickness (wt), and a maximum exactly equal to the thickness of the uncompressed tubing with outer diameter ($id + 2wt$) may be used as design inputs to minimize excessive stress on the tubing while maintaining high compression resolution (Figure 3.2b).

Implementation of a continuously variable compression profile allows for valve customization to match the flow characteristic of a specific pressure-tubing configuration or application. The level of customization is thereby only limited by the manufacturing process used to produce the valve. Through experimental assessment of the relationship between flow-rate (or output pressure or force)

and tube occlusion, the profile may be optimized to deliver any desired response with shaft angle across the desired working range. An example optimization scheme, for generating a linearly varying flow-rate output, has been presented in Section 3.3.1.

3.3 Design, Optimization and Manufacturing

An initial valve design was implemented using an Archimedean (linearly varying radius) spiral as described previously. Further practical considerations made to determine the shape of the compression profile were as follows:

- A suitable opening $\Delta\gamma$ (Figure 3.2a) in the housing should be included that is wide enough to accommodate the tubing and avoid undesired tubing compression when the valve is completely open.
- When the valve is in the completely closed position, the tube should be totally occluded.
- When the valve is in the completely open position, no occlusion should be present on the tube.

To evaluate the radius of the profile under the completely closed position (i.e. $r(\gamma_i) = r_i$), the bearing radius b, the distance between the shaft and the bearing's centers (bearing eccentricity) c, and the tube wall thickness wt were considered in accordance with:

$$r_i = b + c + (2 \cdot wt). \tag{3.2}$$

That is, the completely closed state is assumed to occur when the space between the bearing and housing is equal to twice the tube wall thickness. Similarly, the maximum radius r_e was calculated to occur at the maximum angle (i.e. $r(\gamma_e) = r_e$), and to generate a spacing exactly equal to the thickness of the uncompressed tubing as:

$$r_e = r_i + id. \tag{3.3}$$

Considering that, in the implemented design, the profile starts at $\gamma = \gamma_i$ and stops at $\gamma = \gamma_e$, and that it varies linearly with the angle γ, it can be described

parametrically in Cartesian coordinates using:

$$r(\gamma) = \left(\frac{r_e - r_i}{\gamma_e - \gamma_i} \cdot \gamma - \frac{\gamma_e \cdot r_i - \gamma_i \cdot r_e}{\gamma_e - \gamma_i} \right) \tag{3.4a}$$

$$x(\gamma) = r(\gamma) \cdot \sin(\gamma) \tag{3.4b}$$

$$y(\gamma) = r(\gamma) \cdot \cos(\gamma) \tag{3.4c}$$

where the coordinates $x(\gamma)$ and $y(\gamma)$ identify each point of the resulting compression profile as a function of the angular parameter γ, as shown in Figure 3.4c.

3.3.1 Output Optimization

For the purpose of optimizing the compression profile to match the needs of a particular application in terms of flow-rate resolution and linearity, (3.1) was adjusted to account for the non-linear response of tube compression vs flow-rate.

Optimization was performed using flow-rate vs position data collected using the linearly varying profile ECV. A representative function $g(r, \sigma)$ was selected and fit to these data using a curve fitting algorithm to evaluate the set of function parameters σ. Subsequently, a minimization process was performed to evaluate the compression profile shape required to linearize the output flow-rate vs position characteristic. A desired optimized compression profile curve function $\hat{r}(\gamma, \lambda)$, where λ is an unknown set of function parameters, will cause a transformation of the output profile $g(r, \sigma)$ to a straight line $g(\hat{r}, \sigma)$ passing through the origin and the point where the output is maximum. Formulating this problem as in (3.5a) allows the coefficients λ of the optimized compression curve function $\hat{r}(\gamma, \lambda)$ to be iteratively updated to minimize the difference between $g(r, \sigma)$ and $g(\hat{r}, \sigma)$:

$$\min_{\lambda} \sum_{j=1}^{n} w_j \cdot (g(r(\gamma_j), \sigma) - g(\hat{r}(\gamma_j, \lambda), \sigma))^2 \tag{3.5a}$$

$$x(\gamma) = \hat{r}(\gamma, \lambda) \cdot \sin(\gamma) \tag{3.5b}$$

$$y(\gamma) = \hat{r}(\gamma, \lambda) \cdot \cos(\gamma) \tag{3.5c}$$

where w represents the weightings used to constrain the evaluation of $\hat{r}(\gamma, \lambda)$ to obtain a $g(\hat{r}(\gamma, \lambda))$ that starts at 0 and ends at the maximum output. The

optimization process eventually produces the set of parameters λ and then (3.5b) and (3.5c) as a result.

The curve fitting on experimental data was performed using a function of the form:

$$g(r(\gamma), \sigma) = \frac{a_1}{\pi} \cdot \left(\arctan(b_1 \cdot r + c_1) + \frac{\pi}{2}\right) + d_1 \tag{3.6a}$$

$$\sigma = (a_1\ b_1\ c_1\ d_1). \tag{3.6b}$$

Finally, an $\hat{r}(\gamma, \lambda)$ with unknown parameters λ, in the form:

$$\hat{r}(\gamma, \lambda) = -\frac{a_2}{b_2} - \left(\frac{1}{b_2} \cdot \tan\left((c_2 - \gamma) \cdot \frac{\pi}{d_2} + \frac{\pi}{2}\right)\right) \tag{3.7a}$$

$$\lambda = (a_2\ b_2\ c_2\ d_2) \tag{3.7b}$$

was used to evaluate the compression profile shape. Both Equation 3.6a and Equation 3.7a were empirically selected to fit the collected data and minimize the residual error of the optimization process (`fmincon`, Matlab R2017a).

The linearly varying compression profile $r(\gamma)$, and the resulting optimized compression profile $\hat{r}(\gamma, \lambda)$ are shown in Figure 3.4a. Expected flow-rate characteristics for the two compression profiles are shown in Figure 3.4b. It is worth mentioning that in an ideal case the optimization result (expected flow-rate output) and the desired output would coincide. Instead, in the real case, the minimization problem stops when a minimum of the error function (3.5a) is detected thus introducing a disparity between the two curves.

3.3.2 Device Manufacturing

Two valve designs were fabricated to deliver a linearly varying compression profile ($r(\gamma)$), and the optimized compression profile ($\hat{r}(\gamma, \lambda)$), respectively. The design parameters used to fabricate the two ECV for use with 1/8" inch diameter tubing are summarized in Table 3.1.

As the width of the gap between active and passive compression components is responsible for fine tuning the flow-rate, a number of additional parts were integrated to ensure accurate and precise alignment (Figure 3.3). Firstly, the upper and lower casings are equipped with ball bearings to align the tube housing with the eccentric drive shaft. To further promote concentric placement, both

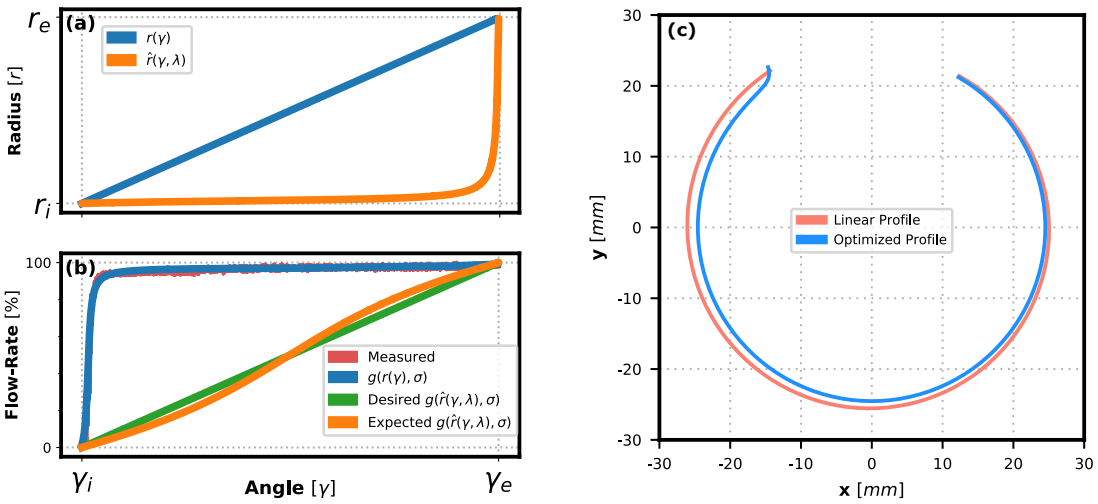

Figure 3.4: (a) Compression radius vs angle relationship for linearly varying and optimized compression profiles. (b) Volumetric flow-rate characteristic measured using a linearly varying compression profile, curve fitting, desired and expected optimization output. ©2020 IEEE . (c) Resulting linearly varying and optimized compression profiles shape.

Parameter	Value
r_i	24.6 mm
r_e	26.4 mm
c	3.2 mm
b	20.0 mm
wt	0.79375 mm
id	1.5875 mm
$\Delta\gamma$	60.0°
γ_i	0°
γ_e	300°

Table 3.1: Design parameters implemented for a linearly varying profile ECV design for 1/8" inch OD tubing. ©2020 IEEE

ends of the shaft are secured to the bearings using two conical aligning nuts. Secondly, to make sure the flexible tube is always in an optimal position in the housing and to reduce its vertical displacement, a tube feeder and a guide are also included.

Precision critical components such as tube housings (with compression profiles), upper and lower casing, eccentric drive shaft and the aligning nuts were fabricated in Aluminium using a CNC milling machine (DMU 40 eVo 5-axis CNC Milling Machine, DMG MORI). Minor custom components such as the tube feeder and the guide were produced using additive manufacturing (Form 2, Clear V4, FormLab). A stepper motor (535-0401 RS Pro, RS Components, UK) with 0.9°/step resolution was selected and coupled to a drive shaft and to

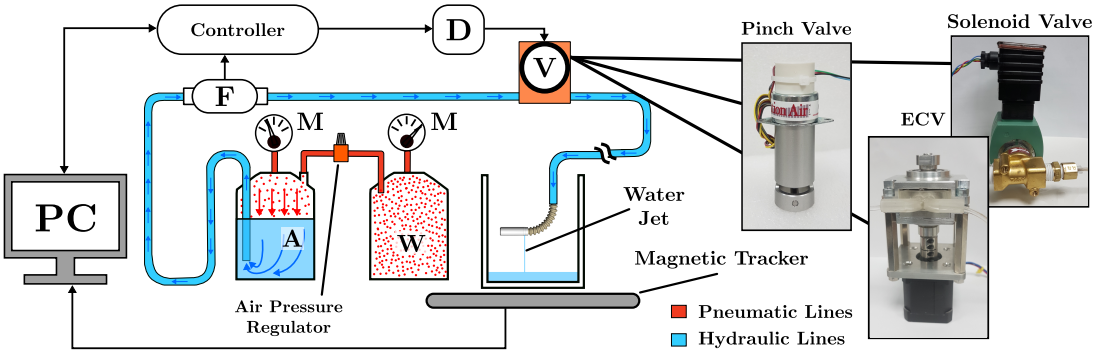

Figure 3.5: Experimental setup for evaluation of valve performance over repeated actuation; components include: (F) flowmeter, (V) valve under test (pinch or compression), (D) valve driver, (M) manometer, Personal Computer (PC); pneumatic and hydraulic lines highlighted. For the application testing (Section 3.5), the setup also includes the HJ tethered capsule and a magnetic tracker. ©2020 IEEE

a compression bearing (764-3714 NSK, RS Components, UK) using a rigid shaft coupling (MCLX-5-5-A, RS Components, UK and 6203ZZC3, NSK, Japan).

Tube compression profiles were designed and machined using the linear compression profile and the optimized profile, determined from the process described in Section 3.3.1. Profiles were subsequently used interchangeably for testing with all other valve components being retained.

3.4 Evaluation

Evaluation of the ECV was conducted to assess: the extent and influence of plastic deformation on the tubing during cyclic operation (Subsection 3.4.1), and the flow characteristics as compared to different valve designs (Subsection 3.4.2). To perform evaluation, in both cases, a testing platform was developed to allow controlled and repeated operation of the different valves; as detailed in Figure 3.5. A water tank, pressurized to 30 PSI (above the atmospheric pressure) using a regulated air supply and a digital manometer (PDMM01, PYLE), was connected to an in-line flowmeter (ATRATO Ultrasonic Flowmeter Model 760, Titan Flowmeters, UK). The outlet of the flowmeter was connected to the inlet of the valve under test via flexible tubing (1/16" I.D. - 1/8" O.D.). Tubing from the valve outlet was subsequently mounted into a water collection tank. The flowmeter data were captured and the valve commands sent using a microcontroller (PSoC 5, Cypress Semiconductor, USA) embedded in a ROS (Robotic Operative System) network. The valves tested were: (1) an ECV with linearly varying profile, (2) an ECV with optimized profile, (3) a standard 1/8" O.D. pinch valve (MPPV-2, Resolution Air, USA), and (4) an in-line solenoid valve (Posiflow Proportional Solenoid Valve, SD8202G052V, ASCO Numatics, USA).

ECV and pinch valves were interfaced using a standard stepper motor driver (Big Easy Driver, Sparkfun, USA), while the solenoid valve utilized its own electronic control unit (8908A001, ASCO Numatics, USA). Test-specific details for investigating the influence of plastic deformation during cyclic operation and for comparing valve designs are detailed in the following subsections.

3.4.1 Tubing Deformation

In the case of dry valve designs, the soft tubing used to transport fluid must be deformed to vary or occlude flow. Repeated deformation of the tubing may result in plastic deformation that has the potential to reduce the tubing integrity and alter the flow characteristics during valve operation. To assess the relative level and influence of induced plastic deformation in the tubing during dry valve (pinch valve and ECV) operation, cyclic actuation testing was conducted. As the hardness of the tubing is an important factor [116], 7 different tubing durometers in the range 40 - 70 Shore A (1/16" I.D. - 1/8" O.D.) were tested over 3000 cycles (1 cycle = completely closed to completely open to completely closed) using each valve. This range of tubing durometer was selected considering a range beyond that of the recommended values for the pinch valve (50 - 60 Shore A).

For each tube durometer-valve combination, data were collected every 50 cycles over a total of 3000 cycles. Each measurement period consisted of a single "slow" cycle (actuation rate of 5 steps-per-second) with data capture, and a subsequent 49 "fast" cycles (actuation rate of 200 steps-per-second) without any data capture. This approach was adopted as a compromise between the need to acquire data from a slow response sensor (flowmeter) and the limited amount of water available in the tank. For pinch valve tests, repeatable position-flow data capture was ensured between measurement periods through implementation of an intermittent calibration. Specifically, prior to each data capture cycle, the valve gate was moved to an internally sensed position and zeroed to avoid potential error produced by missed steps. Similarly, to ensure position-flow repeatability for the ECV, a 600 pulse-per-revolution absolute encoder (04A23902, British Encoder Company, UK) was coupled to the shaft and used to monitor the absolute shaft position and to identify possible missed steps.

After each test, the tube was removed and the visible level of plastic deformation assessed using a microscope (DMS300, Leica, Germany). Objective measures of tube damage (% reduction in diameter) were determined through comparison of the undeformed tubing thickness to the region of minimum tube thickness; measured at tubing regions that were outside and inside of the valve

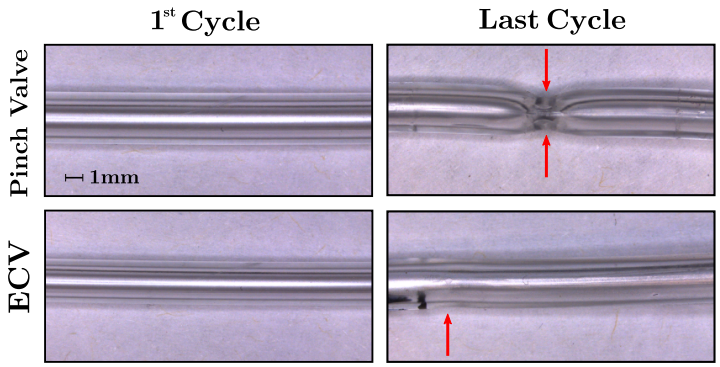

Figure 3.6: Visual influence of repeated valve actuation on 70 Shore A tubing; showing microscope images of actuation locations before and after 3000 cycle tests. Red arrows highlight the identified points of maximum stress. ©2020 IEEE

mechanism respectively. Thickness values were determined through calibrated software measurement, using a known length reference and image analysis software (LAZ EZ, Leica, Germany).

To evaluate the variation in position-flow characteristics for each durometer-valve combination, comparison was made between the first cycle response and subsequent cycles. To quantify relative error, the difference between the flow-rate at the position of 50% maximum flow on the first cycle and the flow-rate at the same position on the n-th cycle was determined. These data were calculated for each measured cycle and normalized to their respective cycle 1 maximum flow. At a pressure difference of 30 PSI, the maximum registered flow-rate was 0.324 l/min, corresponding to the valves in a completely open state.

3.4.1.1 Visual Assessment

Following the cyclic operation of the dry valves, each tube durometer-valve combination was analyzed to determine the level of plastic deformation present. An example comparison of the level of visible damage on the 70 Shore A hardness tubing before use and after 3000 actuation cycles using the pinch valve and ECV is shown in Figure 3.6. Objective measures of tube damage (% reduction in diameter) for all durometers are presented in Table 3.2. It is evident from Figure 3.6 that the pinch valve induces greater visible plastic deformation on tubing when compared to the ECV. This finding is consistent across durometers, with the average (mean ± SD) percentage reduction in tube diameter across all durometers being 21.6 ± 13.8% and 2.7 ± 2.3% for the pinch valve and ECV, respectively, which is statistically significant ($p<0.05$) under a Student's t-test.

	Durometer					
	40 A	**50 A**	**55 A**	**60 A**	**65 A**	**70 A**
Pinch valve	-	3.0	14.1	21.5	31.7	37.7
ECV	-	1.7	1.0	0.9	3.6	6.4

'-' represents no visually identifiable change in tubing diameter.

Table 3.2: Tube damage induced by repeat valve actuation on different tube durometers; showing residual % reduction in diameter measured after 3000 cycles. ©2020 IEEE

	Durometer					
	40 A	**50 A**	**55 A**	**60 A**	**65 A**	**70 A**
Pinch valve	23.5	33.5	43.6	33.7	27.6	11.7
ECV	11.7	11.4	5.2	1.9	0.5	2.3

Table 3.3: Percentage shift in 50% maximum flow-rate position between cycle 1 and cycle 3000. ©2020 IEEE

3.4.1.2 Flow Characteristic Variation

Example opening and closing flow-rate responses for the pinch valve and ECV at the first and last test cycle are shown in Figure 3.7. With fresh tubing (Figure 3.7a and 3.7c), the valve position vs flow-rate characteristic includes a hysteretic behaviour for both the pinch valve and the ECV. After 3000 loading cycles, the level of hysteresis for the pinch valve is reduced while the ECV response remains broadly unchanged, as shown in Figure 3.7b and 3.7d respectively.

Figure 3.8 presents the relative error in the 50% of maximum flow-rate position as a function of loading cycle for each durometer-valve combination for opening and closing. The graph highlights that, when using the pinch valve (Figure 3.8a to 3.8c), the relative error drifts significantly as the number of cycles increases; prevalent across all tubing durometers for opening and closing procedures. When coupled with low durometer tubing (40A-55A), the pinch valve shows less variability (Figure 3.8b), however, the median error remains high; particularly for the opening procedure. Conversely, for the ECV the reduced variability is coupled with low overall median error for opening and closing procedures (Figure 3.8e). Table 3.3 summarizes the relative error through comparison of the 3000th cycle for each valve-durometer combination. The average (mean $\pm$ SD) percentage shift across all durometers was 28.9 $\pm$ 10.8% and 5.5 $\pm$ 4.9% for the pinch valve and ECV respectively, which was statistically significant ($p < 0.05$) under a Student's t-test.

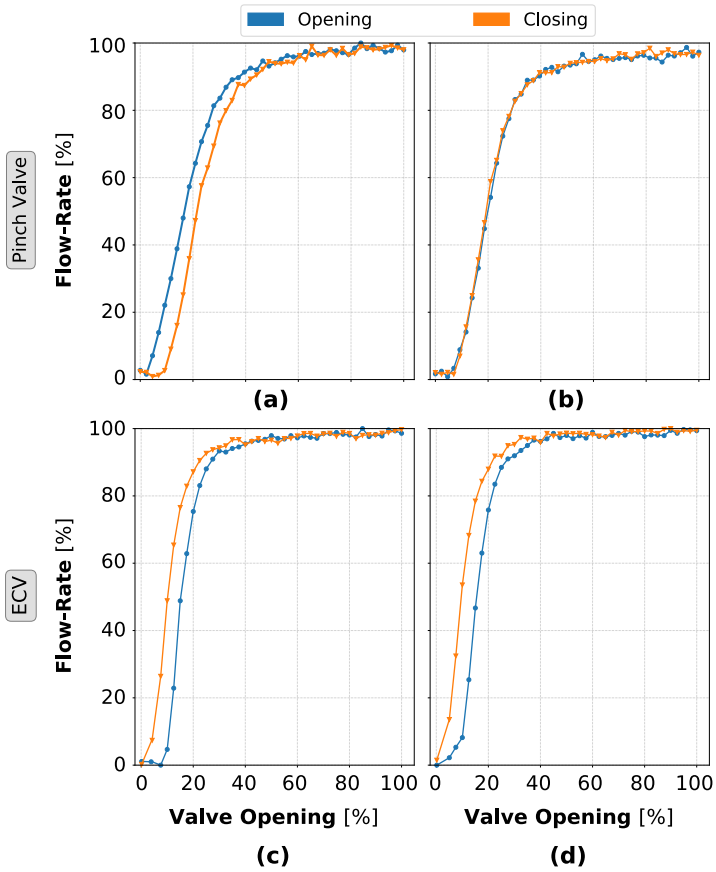

Figure 3.7: Influence of repeat valve actuation on the hysteretic behaviour of the sanitary valves. Graphs a) and c) show the hysteresis loop during the first actuation cycle. Graphs b) and d) refer to the last (3000^{th}) cycle.

3.4.2 Valves Comparison

In addition to evaluating the level and influence of plastic deformation in dry valve tubing, the ECV with a linearly varying compression profile was also compared with its optimized equivalent and a wet valve alternative (in-line solenoid valve). Each valve was tested using the same experimental setup as for cyclic loading tests (Figure 3.5) over 10 repeats at a cycle actuation rate of 5 steps-per-second while position and flow-rate data were recorded.

The volumetric flow-rate characteristics as a function of valve position for the linearly varying and optimized ECV designs are shown in Figure 3.9. For comparison, the desired and expected position vs flow-rate linear response of the optimized ECV are also presented.

The linearly varying ECV demonstrates a non-linear relationship between flow and position which leads to poor flow-rate resolution of the valve within the working range. This results in 90% of the maximum flow-rate being reached within the first 16.2 degrees (equivalent to 18 steps), while the remaining 263.7 degrees (293 steps) are used to control only the final 10% of the flow-rate range.

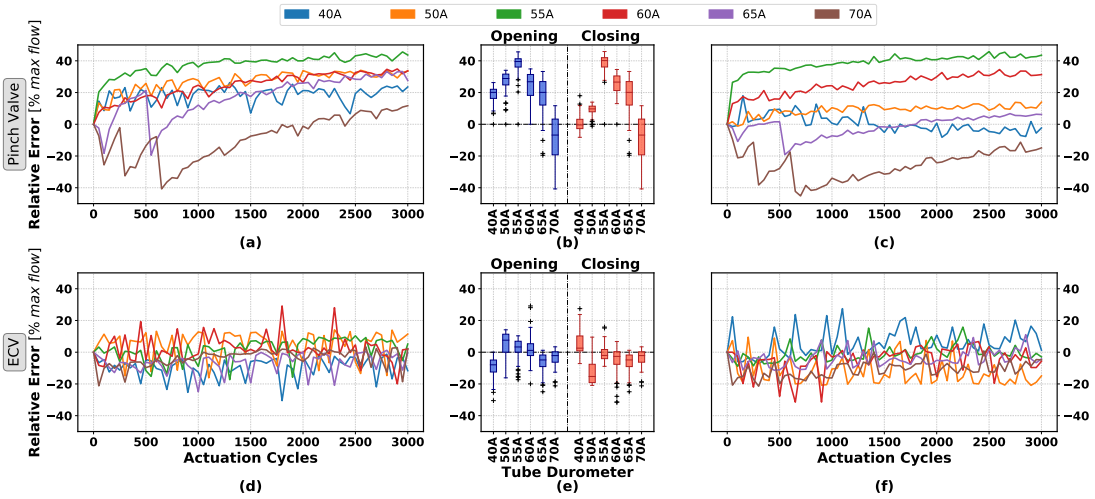

Figure 3.8: Flow-rate error (evaluated as the difference between the flow-rate at the position of 50% maximum flow on the first cycle and the value of the flow-rate at the same position on the n-th cycle) for varied durometers over 3000 actuation cycles; shoving: pinch valve opening (a), closing (c), ECV opening (d), closing (f). Median and inter-quartile range, referring to opening and closing for the pinch valve (b) and ECV (e). ©2020 IEEE

The optimized ECV profile instead shows a response with more even flow-rate changes across the entire position range. Measured data from the optimized profile ECV, however, differs from the expected output and maintains a significant level of hysteresis.

Figure 3.10 makes direct comparison of the valve position vs flow-rate response for the four valves: pinch valve, solenoid valve, linearly varying and optimized ECV. The poor resolution of pinch and solenoid valve is evident, with the flow-rate saturating after 50% of the respective valve ranges. The dynamic influence of the step resolution is also clear; as large flow-rate jumps are recognizable throughout the working range. Conversely, the optimized profile ECV maintains a smooth increasing flow-rate across the full range of valve positions, however, demonstrates a similar level of variability to the pinch valve across 10 repeats.

3.5 Application

With improved linearity and resolution (Figure 3.10), and reduced variation in valve position vs flow-rate characteristics under repeated actuation (Figure 3.8), it is important to understand the impact of using an optimized ECV on the controllability of an application-specific actuator. To this end, this section demonstrates the optimized ECV applied to a flow-rate controlled soft manipulator. Example designs were fabricated to suit the HJ endoscopic capsule device.

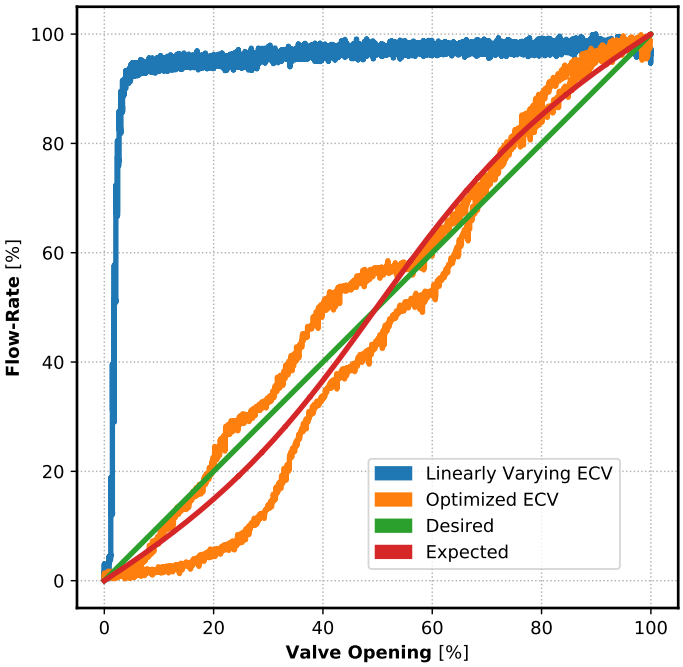

Figure 3.9: Flow-rate characteristics of the ECV generated by a linearly varying compression profile (blue) and using the optimized profile (orange). The desired response used for optimization (green) and the expected output based on the optimized profile attained (red) are also shown. ©2020 IEEE

As previously described in 2, the flow-rate of the HJ three pressure lines has previously been controlled independently through electronic actuation of a line-specific pinch valves (MPPV-2, Resolution Air, USA), [16]. The three nozzles, placed on the capsule's body , facilitate ejection of pressurized water; thereby inducing movement in the capsule as a result of the generated jet thrust T

$$T = \rho \cdot \dot{V}^2 \cdot \left(\frac{1}{A_{out}} - \frac{1}{A_{in}} \right) \tag{3.8}$$

where ρ is the density of water, $\dot{V}$ is the volumetric flow-rate, A_{in} and A_{out} are geometric parameters of the nozzles, inlet and outlet sections respectively.

Due to the soft and flexible nature of the device, even modest fluctuations in flow-rate can lead to significant position and orientation variation. This therefore, precludes the implementation of autonomous or semi-autonomous control strategies, and increases the demand on the operator. The optimized ECV design was therefore evaluated within the context of the HJ application, under direct comparison to pinch and solenoid valves. However, the design methodology and assessment techniques presented may be extended to any device requiring the sanitary control of fluid flow.

Alongside repeatability, flow-rate resolution is also crucial in the actuation of

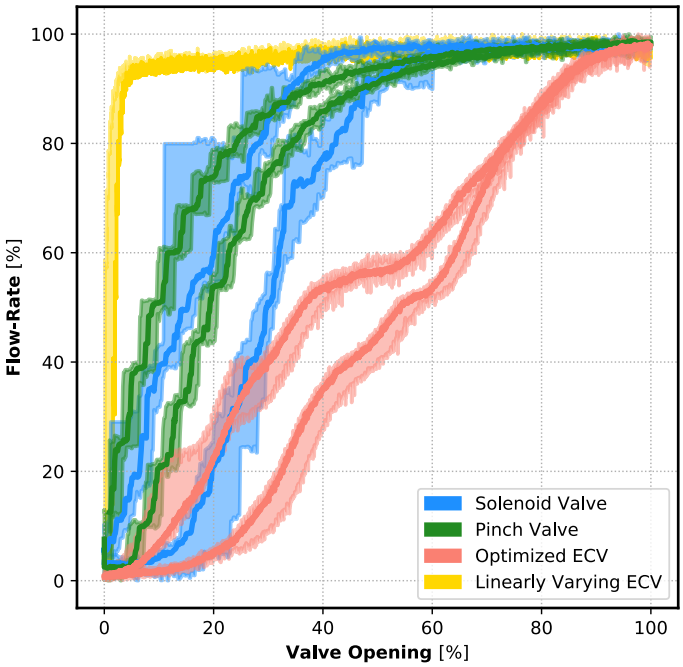

Figure 3.10: Volumetric flow-rate characteristics generated by the solenoid valve (blue), pinch valve (green) and ECV (red), linearly varying ECV (yellow), evaluated as the median (dark curves), maximum and minimum values (shaded area) over 10 repetitions for both opening and closing procedures. ©2020 IEEE

the HJ system. The possibility to fine tune the flow-rate, and consequently the jet thrusts, allows for smooth trajectories between desired positions and delivers stable anatomy visualization during a gastroscopy procedure.

To test the influence of the three valves on the performance of the HJ, a single jet bending test was performed by controlling its flow-rate (see the video in the multimedia extension). Sinusoidal command profiles at different frequencies were selected to simulate open-loop valve control. For each valve, a sinusoidal command with a fixed frequency of either 0.05 Hz, 0.1 Hz or 0.2 Hz was supplied to its controller while the flow-rate and tip pose were measured using an ultrasonic flowmeter (see Section 3.4) and magnetic tracker (Aurora Electromagnetic Tracking System, NDI), respectively. Each valve-frequency combination was tested over 10 cycles.

Figure 3.11a shows the tip angle response over two cycles at each frequency for the three valves. The desired bending angle was evaluated starting from the sinusoidal command fed to the valve and the assumption of quadratic relation between volumetric flow-rate and bending angle. Then, the valve command was re-scaled in the range between 0° and the maximum bending angle achieved for the valve under test (approximately 70°) when the flow-rate is maximum. The ECV output shows smoother tip movements across all frequencies when

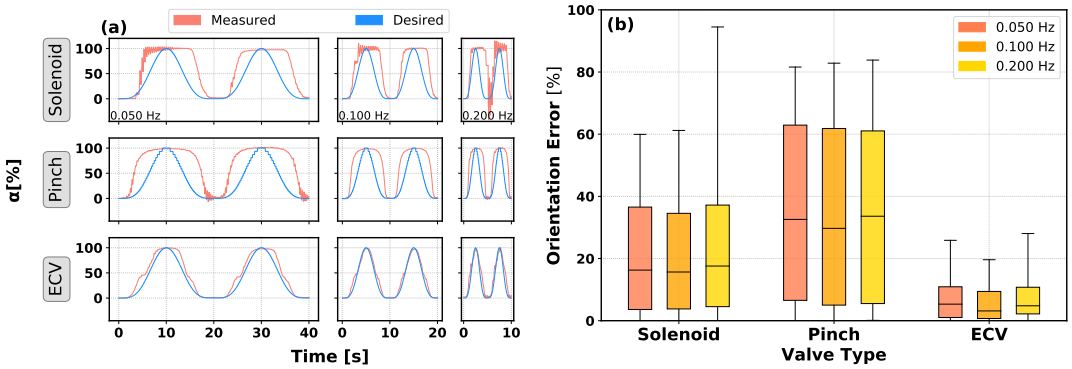

Figure 3.11: (a) HJ capsule bending angle (α) as a result of single jet actuation. The angle has been measured considering the initial orientation (tether and capsule aligned with the gravity vector) as reference (0°) and a maximum bending angle of about 70°. (b) Orientation error measured as the difference between the desired and measured bending angle. ©2020 IEEE

compared to the solenoid and pinch valve. Overall, the ECV allows the tip to follow the desired pattern with higher accuracy for all the applied commands (median errors 5.3%, 3.1% and 4.8% for the three proposed signal frequencies), as shown in Figure 3.11b. Comparative median errors are significantly higher for the pinch valve (32.5%, 29.7% and 33.6%) and solenoid valve (16.2%, 15.6% and 17.5%) respectively.

The magnitude of the flow-rate variation, and consequently the change in bending angle, resulting from opening or closing the valve one step at a time, is presented in Figure 3.12a. For solenoid and pinch valve, approximately 75% of the fluctuations stay below 5% of flow-rate variation; however more extreme values are present and reach maxima of 19.2% and 14.2%, respectively. Conversely, the ECV shows flow-rate variations generally smaller than 1%, with extreme values remaining under 4%. The effect of these flow-rate variations on the jet thrust produced and therefore on the capsule bending angles (α) is shown in Figure 3.12b. In the supplementary video, the amplitude of the oscillatory movement of the HJ capsule is presented for each valve; using a contour plot to locate the oscillations along the capsule trajectory. Congruently with the previous results, the smoother flow-rate profile produced by the ECV translate into higher actuation accuracy and an absence of oscillations.

3.6 Discussion

The reduced plastic deformation (Figure 3.6) and change in position vs flow-rate characteristics after repeated operation (Figure 3.7) realized by the ECV represent improved open-loop performance relative to the pinch valve. Although

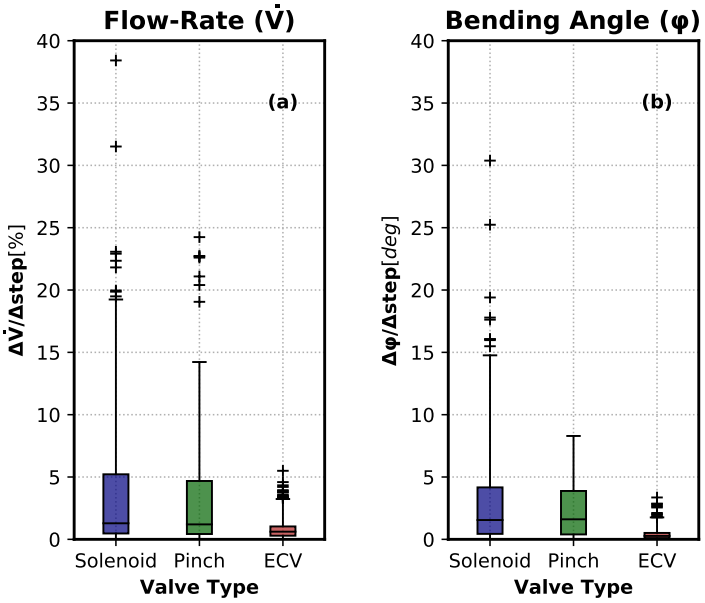

Figure 3.12: Flow-rate (a) and bending angle (b) fluctuation as a result of opening/closing the each valve one step at a time. Outliers policy: $3 \cdot IQR$. ©2020 IEEE

significant hysteresis is present in the flow characteristic, this is largely invariant with cyclic operation and may therefore be accounted for with an appropriate valve model. In contrast, the pinch valve shows a reducing but varying level of hysteresis, which amplifies complexity in generating a suitable valve model.

The reduced levels of plastic deformation were realized through increased contact area between the tubing and valve housing and the moving compression point, intrinsic to the ECV design. Although improvements may be possible with modification to the pinch valve contact area, it is not feasible to introduce a moving contact point within its existing design.

Tubing durometer has also been shown to influence flow characteristics during cyclic operation (Figure 3.8). Using the pinch valve shows larger drift across the cycle range tested when compared to the ECV, as summarized in Table 3.3. These characteristics make selection of a suitable tube durometer for the valves challenging, particularly for the pinch valve. However, with consideration of both precision and accuracy, the results indicate that a tube durometer of 55 A is most suitable for use with the ECV while 50 A is least suitable.

With reduced flow-rate drift, it becomes feasible to use the valve for applications requiring a varying test duration. In the presented study, a duration of 3000 cycles was selected in relation to the case study described in Section 3.5. This was chosen considering two factors: the maximum speed at which the ECV can be operated and an estimation of the time of completion for a gastroscopy procedure. Given that the current maximum speed without motor stall is 1000

steps/s (from completely closed to completely open in 0.333s) and a worst-case scenario gastroscopy procedural time of 30 minutes [118], the ECV will be able to perform a maximum of $\approx$ 2700, approximated to 3000, cycles during each procedure.

Through optimization of the ECV design (Subsection 3.4.2), a more linear flow-rate response with improved resolution was produced, as shown in Figure 3.10. Although effective, the optimized ECV still shows error with respect to the desired profile. Factors that are likely to contribute to this are: accuracy and precision of the manufacturing process used to generate the profile, profile-tubing alignment, imperfect fitting of measured data used for the optimization process and changes in the flow-rate regime which have not been considered in this work. For applications requiring even higher levels of flow control precision, these factors may be improved incrementally.

For the presented case study in Section 3.5, implementing the optimized ECV shows reduced variation in flow-rate and bending angle error (Figure 3.12). This results from the improved linearity and resolution of the ECV with respect to the solenoid and pinch vales; which show abrupt changes in flow-rate during opening and closing (Figure 3.10). In the supplementary video, these differences may be seen in terms of oscillatory movement of the HJ tip. Although this is one specific test case, achieving improved performance in open-loop sanitary flow control may be beneficial to a wide range of future applications, particularly in the field of soft medical robotics.

3.7 Conclusions

A novel design methodology for a sanitary fluid flow control system has been presented and implemented. The ECV offers a generic platform for application in pneumatic and hydraulic systems where sanitary flow regulation is required (e.g. medical applications). The valve is easy to fabricate thanks to the simple principle of operation which relies on off-the-shelf, machined and 3D printable components, even if the machined parts demand the manufacturing process to be sufficiently accurate. By exploiting a large and adaptable compression profile, increased resolution and linearity may be manufactured into the device; accounting for application specific requirements. To this end, we have presented a device-specific optimization strategy that shows improved linearity when compared to a standard linearly-varying profile, and to commercially available alternative valves. Through increasing the tubing contact area under compression, a sig-

nificant reduction in plastic deformation (up to about 96% reduction for tube durometer 60 A) and its associated influence on flow-rate (up to 98% for tube durometer 65 A) vs valve position was shown across a range of tubing durometers. To demonstrate the significance of these improvements on a real system, an optimized profile ECV was compared with pinch and solenoid valves for controlling the orientation of a water propelled tethered capsule (the HJ). A significant overall reduction in error with respect to the commanded behaviour has been shown, with mitigation of oscillatory movements. Ultimately, this allows for suitable open loop control of the orientation of the tip, where the linearity of the ECV allows for close following of the desired signal across frequencies.

The ECV has demonstrated the potential for a new sanitary valve actuation method that could aid in delivering more precise open-loop flow control systems and facilitate development of the next generation of medical soft robots.

Chapter 4

Task-Space Control of a Water-Jet Powered Soft Manipulator with Hysteretic Actuation

4.1 Introduction

The introduction of single-use endoscopic platforms for inspection of the stomach cavity, represents the foundation for the implementation of population based gastric cancer screening programmes in high risk countries, including their hard-to-access rural areas. Although these devices offer reduced equipment and procedural costs, they do not directly address the need for trained personnel to manually drive the tip of the endoscope and verify the cavity has been entirely explored. For this reason, their use in rural settings remains subject to the availability of specially trained personnel. The possibility for non-expert users to successfully perform an endoscopy procedure and achieve a comparable quality of diagnosis to that of a highly trained GE, would drastically reduce the time needed to screen the entire population, and reduce the overall cost of the screening programme.

One paradigm for making this possible is the development and implementation of automatic endoscope navigation techniques, capable of guiding the endoscope tip along an optimal trajectory to guarantee visualization of all gastric landmarks. This approach would allow non-experienced staff to deploy the endoscope and perform the gastroscopy procedure in a consistent and repeatable way, while images may be reviewed offline or online via algorithm-based abnormalities classification techniques [119].

A classic approach to this problem would be to implement an automatic

closed-loop position control strategy. To this end, automatic control represents the building block that allows general users to abstract from the low level mechanics and dynamics of the tool, while enabling the development of high-level autonomous functionalities [120, 121].

A number of challenges arise from the need for an automatic control scheme, with these becoming even more demanding in the field of CMs and soft CMs [55]. The advanced sensing and modelling knowledge developed over the years for classic rigid link robots clashes with the limited and relatively new tools available for CMs. This results in a dearth of standardized methods to utilize when developing a closed-loop control system.

First of all, the elastic behaviour of CM and the large deformations created by applied forces make modeling of soft CMs a significant problem. In contrast with rigid link robots, the kinematic problem in CM can not be defined in a closed-form unless simplifying assumption are made [122]. Moreover, the inversion of the kinematic problem does not generally result in a single solution. Different methods have been developed over the years aiming at estimating how a soft body reacts to applied loads: Constant-Curvature (CC) or Piecewise-Constant-Curvature (PCC) assumption [93, 122, 123], Finite Element Method (FEM) [124] and Cosserat-Rod model [18] to cite a few.

Designing a control strategy that employs inverse kinematics, in open-loop fashion, often results in poor performance or instability of the controlled system. A sensor feedback is thus necessary to close the control loop, compensate for the model inaccuracies and stabilize the plant [18]. Furthermore, the robot model often does not take into account the interaction between the robot and obstacles so that, when the CM moves inside a constrained environment, a model-based closed loop-control generally fails. Attempts to include a description of the collision have been made, but resulted in a model characterized by a high level of complexity and computational cost while necessitating additional sensors or calibration procedures [125].

The above mentioned limitations could be avoided by implementing model-free controllers. Such methods generally consist of data-based [126, 127] or empirical method [125, 128] that learn or estimate the actuation inputs required to position the CM in a defined pose, and they have been proven extremely effective when applied to non-uniform and highly non-linear soft CMs [105].

The ability to measure the output of the actuators (e.g. force, pressure, flow-rate, etc.) remains essential for both estimating the localized or distributed loads acting on the CM's body and for compensating for actuators' non-linearities. Hysteresis is a common non-linearity which often creates difficulties in controller

design and reduces the expected performance of the controlled system, thus requiring a compensation strategy that minimizes its detrimental effects.

Despite not being further discussed in this chapter, position sensing represents another challenging topic for soft CMs. The sensors must be able to provide accurate and precise localization feedback if fine control is needed, and, at the same time, they must minimize their influence on the the manipulator kinematics or dynamics. These requirements significantly narrow the choice of suitable sensors; the consequences of which are particularly evident in the case of low-cost disposable endoscopy. The sensor technology of such devices is typically limited to a camera module and makes the implementation of localization and closed-loop control trajectory tracking strategies complex or inaccurate. The image sensor, not only provides an essential visual feedback to the physician but, may contribute with additional information such as the 3D pose of the endoscope's tip and a sparse/dense 3D reconstruction of the environment structure, thanks to Simultaneous Localization and Mapping (SLAM) algorithms [129, 130, 131, 132].

In this chapter a model-free closed-loop control strategy is presented and applied to a soft CM under Tip Follower Actuation (TFA): the HJ endoscope. The control problem is defined in a polar coordinate system, considered as the most suitable and intuitive way to describe the HJ's task-space. The hysteresis loop, observed in the actuation system, is modelled and the effects of both a compensated and non-compensated control strategy are shown. The control action, incrementally adjusts the wrench, acting at the tip of the HJ, along the two controlled coordinates φ and ϑ, forcing the tip of the endoscope to follow a desired trajectory. The chapter is structured in two main parts: Section 4.2 introduces the sensor calibration procedure, the task-space description, the valves hysteresis loop modelling and the closed-loop control architecture, while Section 4.3 shows the results from a series of experiments, demonstrating the advantages introduced by the hysteresis compensation and the ability of the control scheme to lead the endoscope's tip along the requested trajectory.

4.2 Task Space Control

In this section, the approach adopted to implement position control of the HJ's tip is described. The proposed method controls the HJ's tip in a polar coordinate system by modulating the wrench that acts on the endoscope's tip. A first implementation of the control scheme directly acts on the actuators (ECV [104]) to adjust the tip wrench, while a successive optimization of the controller

considers the valves' hysteresis loop to achieve a more responsive system, able to follow a desired trajectory.

4.2.1 Sensors

Closed-loop control architectures relies on the sensor feedback to minimize the error between desired and measured values of the controlled variables. As previously described in Chapter 2, the HJ's sensor equipment consists of an IMU placed inside the base connector, a camera module at the tip of the endoscope and two 6-DoF EM probes, one at the base and one at the tip of the endoscope. During the fabrication process, these sensors are installed in specific positions, but due to axial symmetry of the probes (e.g. EM and camera module) or imprecise manual positioning, a calibration method is required to compensate for orientation offsets. A calibration rig, fabricated through rapid prototyping (Tough White, S5, Ultimaker, Netherlands), was designed to align the sensors' local reference frames according to a predefined convention. The calibration object was designed to accomplish this task for all the available sensors, including the estimation of the camera intrinsic and extrinsic parameters, and the lens distortion using a checkerboard. For the purposes of this chapter, only the calibration of the EM probes is considered.

The calibration process aims at defining local reference frames that are aligned with mechanical features of the HJ's tip. Specifically, the adopted convention considers the tip z-axis ($\boldsymbol{z}_t$) aligned with the tip longitudinal direction and pointing outwardly, while the y-axis ($\boldsymbol{y}_t$) is aligned with the nozzle that corresponds to the second water jet J_2. A preparatory procedure consists of positioning the HJ endoscope on the calibration object as shown in Figure 4.1a, and twisting the steerable section until J_2 aligns with a mark on the calibration object. Eventually, the HJ is locked in position using two clamps.

To achieve the desired configuration of the sensors' reference frame and considering that the cylindrical EM probes are located in 0.9 mm diameter slots in the HJ's tip and base, and have their local z-axis aligned with their longitudinal direction, a two-parts calibration process was performed. A z-axis calibration was executed first: the calibration object was positioned on the EM field generator (Aurora Tabletop) as shown in Figure 4.1b, then the rotation angles around the sensor's x and y axes that align the $\boldsymbol{z}_t$ with the field generator world frame z-axis ($\boldsymbol{z}_w$), are estimated. The same procedure was repeated with the calibration object in the configuration shown in Figure 4.1c. Here, the sensor's reference frame is rotated around $\boldsymbol{z}_t$ until $\boldsymbol{y}_t$ aligns with -$\boldsymbol{z}_w$, in this way obtaining a tip reference

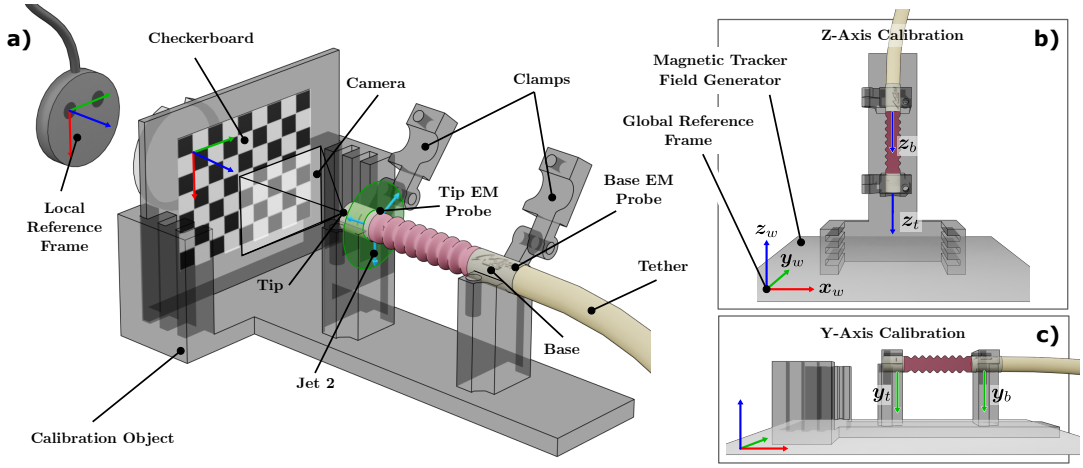

Figure 4.1: Sensor calibration procedure showing a) the HJ steerable segment positioned on the calibration object, the camera calibration checkerboard and b-c) the two configurations required for local frames calibration process, $\boldsymbol{z}_t$, $\boldsymbol{z}_b$ in b) and $\boldsymbol{y}_t$, $\boldsymbol{y}_b$ in c).

frame as shown in Figure 4.2a. The same method applies to the calibration of the base EM probe.

4.2.2 Task Space

Thanks to its kinematic characteristics and actuation system that generates a localized wrench at the tip of the endoscope (TFA), the HJ's tip can move in the free space with two bending DoF: up-down and left-right as it happens in a standard FE. In its configuration space, the HJ bending section can be described by the vector $\boldsymbol{c} = [u\, v\, s]^T$ [133], with u and v components of the bending axis and s arc-length of the bending section (fixed in the HJ) such that a change in u or v results in both an increased or decreased bending angle and a change in the bending direction, at the same time. A more intuitive approach to the description of the HJ's tip movements considers its task space expressed in a polar coordinates system. Similarly to its configuration space, a single-section CM's task space can be described, in a polar coordinates system, by the vector $\boldsymbol{\omega} = [\varphi\, \vartheta\, r]^T$ (Figure 4.2c), representing the tip's azimuth and elevation with respect to the base reference frame, and the tip-base distance respectively. The latter is mentioned here for the sake of completeness but is non-controllable in the current implementation of the HJ, thus it is omitted in the following sections. Such a description allows independent control of each variable and intuitively defines a trajectory to be followed by the tip.

Using the the information relative to the orientation of the HJ's tip and base, provided by the EM probes, the tip elevation ϑ is evaluated as the angle between $\boldsymbol{z}_b$ and $\boldsymbol{z}_t$, with these two vectors also defining the bending plane β. The tip

azimuth φ represents the angle between β and the plane defined by the vectors $\boldsymbol{y}_b$ and $\boldsymbol{z}_b$ (Equation 4.1).

$$\begin{aligned} \vartheta &= \boldsymbol{z}_t \cdot \boldsymbol{z}_b \\ \varphi_a &= (\boldsymbol{z}_b \times (\boldsymbol{z}_t \times \boldsymbol{z}_b)) \cdot (-\boldsymbol{y}_b)\,. \end{aligned} \tag{4.1}$$

Despite the advantage of using this representation, such a description of the task space shows two main singularities. In an ideally straight configuration of the HJ's bending segment ($\vartheta = 0$), $\boldsymbol{z}_t$ aligns with $\boldsymbol{z}_b$, resulting in an initial offset of $\pi/2$ in φ, and sudden change in φ when the tip oscillates in a local region around $\vartheta \simeq 0$. The second singularity refers to the range of variation of φ. The evaluation of φ, as in Equation 4.1, returns a symmetrical value with respect to $\boldsymbol{y}_b$, ranging in between 0 and π, while, for control purposes, a non-symmetrical 0 to 2π range is desirable.

To mitigate the risk of incurring into position discontinuities that could not be handled by the control scheme and could result in an instability of the system, a few precautions were considered in the evaluation of the tip position $\boldsymbol{\omega}$. Despite being responsible for the discontinuity of φ, the elevation ϑ is never singular and can be controlled at all times. In a real scenario, the evaluation of φ will then start only after a stable plane β is identified, in other words, when ϑ exceeds a user defined safety threshold; otherwise φ remains null. Henceforth, desired and measured values of ϑ below the safety threshold must be avoided.

To prevent symmetry in φ coordinate, the output of Equation 4.1 is updated using Equation 4.2

$$\begin{cases} \varphi_b = 2\pi - \varphi_a & if\ c < 0 \\ \varphi = \varphi_b & otherwise \end{cases} \qquad where\ \ c = (\boldsymbol{z}_b \times (\boldsymbol{z}_t \times \boldsymbol{z}_b)) \times (\boldsymbol{y}_b) \tag{4.2}$$

with φ_a and φ_b accessory variables used in the φ correction process.

At this point, φ continuously varies between 0 and 2π but, at these two extreme points, a discontinuity exists ($0 \equiv 2\pi$). To eliminate this remaining singularity, φ is further corrected using Equation 4.3:

$$\begin{cases} \Delta\varphi = \varphi\,(t-1) - \varphi\,(t) & \\ \quad g = g + \Delta\varphi & if\ \Delta\varphi \geq 2\pi \\ \quad \varphi = \varphi + g & \end{cases} \tag{4.3}$$

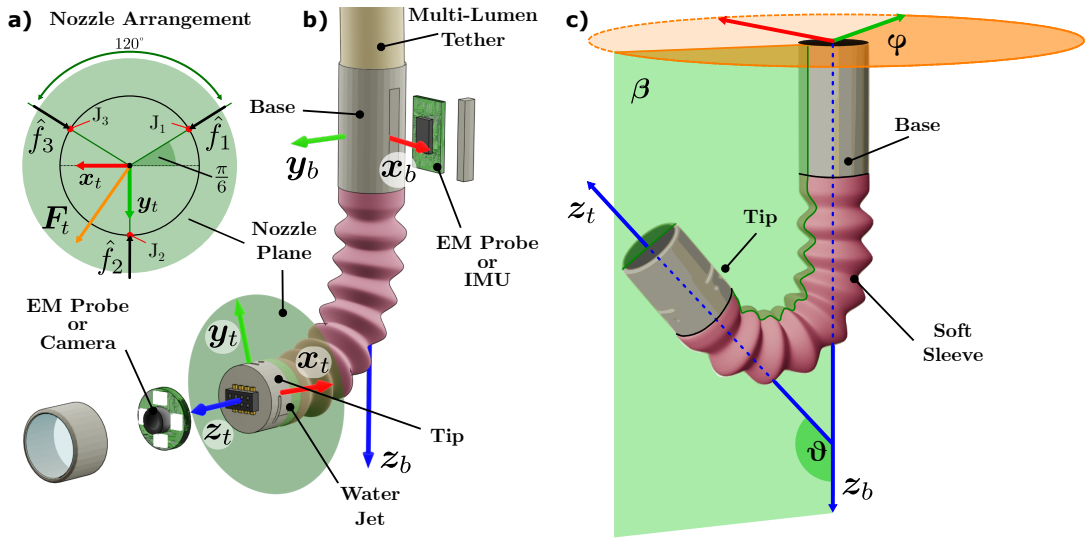

Figure 4.2: The HJ's steerable section with a) a detailed description of the nozzle arrangement with respect to the tip reference frame ($\boldsymbol{T}_t$), b) an exploded view of the HJ's components and sensor equipment, and c) a representation of the polar coordinates φ and ϑ.

where $\Delta\varphi$ identifies the discontinuity in φ, and g registers the number of full revolutions performed by the tip.

This approach guarantees a continuously varying φ in a range $[-\infty, +\infty]$, ideal for a position control scheme.

As mentioned in Section 4.2.1, the tip local reference frame $\boldsymbol{T}_t$ has $\boldsymbol{x}_t$ and $\boldsymbol{y}_t$ lying on the nozzle plane and $\boldsymbol{z}_t$ aligned with the capsule longitudinal axis. The axis $\boldsymbol{y}_t$ is also aligned with one of the three nozzles which was referred to as Jet 2 (J_2) or, in terms of jet force, $\hat{f}_2$. Given this nozzle arrangement (Figure 4.2a) and their resulting in-plane force, the only non-null elements of the tip wrench are the x and y components of the Cartesian force $\boldsymbol{F}_t$ generated by the thrusters. The force $\boldsymbol{F}_t$, expressed in $\boldsymbol{T}_t$, can then be written as:

$$
\begin{aligned}
\boldsymbol{F}_t &= \boldsymbol{A} \cdot \hat{\boldsymbol{f}} \\
\boldsymbol{F}_t &= \begin{bmatrix} F_x \\ F_y \end{bmatrix} \\
\boldsymbol{A} &= \begin{bmatrix} -cos(\frac{\pi}{6}) & 0 & cos(\frac{\pi}{6}) \\ sin(\frac{\pi}{6}) & -1 & sin(\frac{\pi}{6}) \end{bmatrix} \\
\hat{\boldsymbol{f}} &= \begin{bmatrix} \hat{f}_1 \\ \hat{f}_2 \\ \hat{f}_3 \end{bmatrix}
\end{aligned}
\tag{4.4}
$$

where $\boldsymbol{A}$ describes how the nozzles, and consequently the jet forces, are oriented with respect to $\boldsymbol{T}_t$, while $\hat{\boldsymbol{f}}$ contains the forces generated by the i-*th* jet.

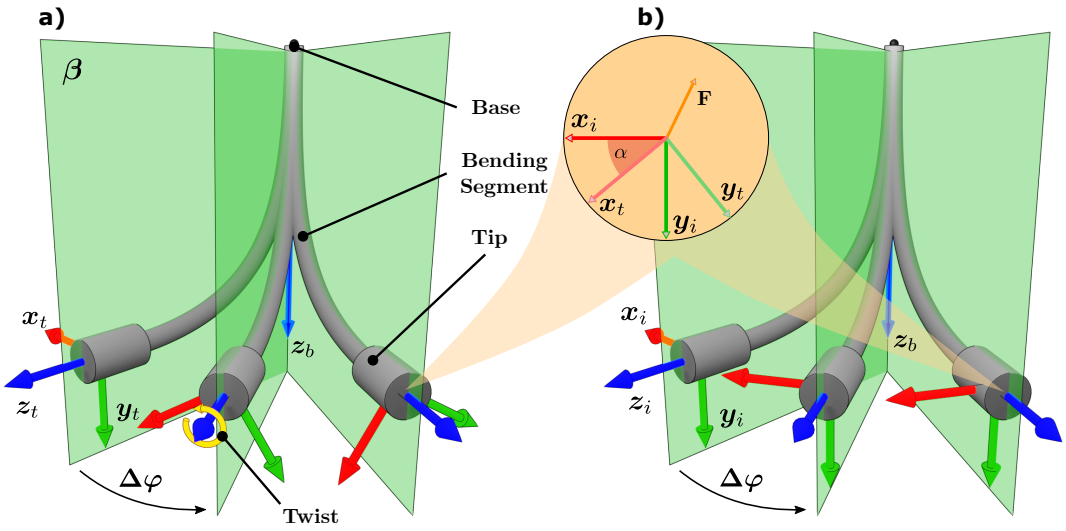

Figure 4.3: Orientation of the reference frames at the HJ's tip showing how a change in the φ coordinate causes a twist in a) $\boldsymbol{T}_t$, while b) $\boldsymbol{T}_i$ remains invariant.

It is worth noticing that the opposite problem, i.e. finding the set of jet forces $\hat{\boldsymbol{f}}$ that generates a desired $\boldsymbol{F}_t$, is under-determined and can only be solved as a constrained minimization problem. The constrains are dictated by the nature of the actuation system: each water jet can only generate positive thrust. The problem can then be written in the form of a non-negative least-squares minimization:

$$\underset{\hat{\boldsymbol{f}} \geqslant \boldsymbol{0}}{\operatorname{argmin}} \, || \, \boldsymbol{A} \cdot \hat{\boldsymbol{f}} - \boldsymbol{F}_t \, || \, . \tag{4.5}$$

To understand how a variation in the applied force affects the position of the tip, it becomes necessary to introduce an accessory reference frame $\boldsymbol{T}_i$, invariant to changes in φ. $\boldsymbol{T}_i$ and $\boldsymbol{T}_t$ share their origins and z-axes, while $\boldsymbol{x}_i$ is always normal to the β plane, pointing in the direction of decreasing φ. $\boldsymbol{y}_i$ is evaluated accordingly, in this way pointing towards the direction of decreasing ϑ (Figure 4.3b). This known transformation between $\boldsymbol{T}_i$ and $\boldsymbol{T}_t$ is described by the rotation matrix $\boldsymbol{B}$:

$$\begin{aligned} \boldsymbol{F}_t &= \boldsymbol{B}^{-1} \cdot \boldsymbol{F}_i \\ \boldsymbol{B} &= \begin{bmatrix} cos(\alpha) & -sin(\alpha) \\ sin(\alpha) & cos(\alpha) \end{bmatrix} \end{aligned} \tag{4.6}$$

with α measured rotation angle around $\boldsymbol{z}_t$. Using $\boldsymbol{B}$, the Cartesian components of the tip force $\boldsymbol{F}_t = [F_x \, F_y]^T$ can be mapped into $\boldsymbol{T}_i$ and vice versa (Equation 4.6). Thanks to the above mentioned geometric properties of $\boldsymbol{T}_i$, $\boldsymbol{F}_i$

can be expressed as $\boldsymbol{F}_i = [F_\varphi \, F_\vartheta]^T$ since a change in F_φ directly affects the azimuth position of the tip, while F_ϑ generates changes only in the tip elevation. In other words, $\boldsymbol{T}_i$ allows to express the force acting at the tip as if the HJ was actuated by two forces and each of these two forces was influencing directly and exclusively one of the controlled variables.

4.2.3 Hysteresis

The HJ platform employs a flow-rate control system based on the ECV. The hysteresis loop exhibited by these valves, described in in Chapter 3, represents a challenge from a control system design point of view. The lack of compensation for such non-linearities of the actuation system often leads to limited performance of the control system or, in the worst-case scenario, to an instability of the controlled plant.

This typically happens when the hysteresis prevents the control system from acting synchronously on the actuators. For example, in the case of the HJ, a movement driven by a single jet can easily, even if not optimally, be performed in a closed-loop fashion without the need to compensate for the hysteresis of the ECVs. This is possible because, in this particular case, synchronization of multiple jets is no necessary. On the other hand, when the desired tip position requires the simultaneous actuation of more than one jet, the ability of the valves to promptly adjust the jet's flow-rate becomes crucial in maintaining the stability of the endoscope's tip.

For these reasons a hysteresis model was developed using experimental data acquired during preliminary calibration of the ECVs. Using the experimental set-up described in Figure 2.8, flow-rate and valve position data were acquired while sequentially operating the valve. Starting from its completely closed initial state, the valve was completely opened and then closed again. Such a procedure was repeated 3 times for each valve, in this way obtaining the results shown in Figure 4.4. The linear characteristics of the ECV simplify greatly the mathematical description of the hysteresis loop. As such, this was modelled using two different linear functions, one for closing operations ($h_{close}(\boldsymbol{f})$) and one for the opening operations ($h_{open}(\boldsymbol{f})$), excluding from the curve-fitting dataset all the data points belonging to the "dead-zone" (i.e. the region where a change in the valve position does not result in a change in the flow-rate).

While the closing curve perfectly matches the ideal valve characteristic, the opening curve presents a dead-zone followed by a lower slope linear region. The main expected consequence is a difference in the responsiveness of the actuator

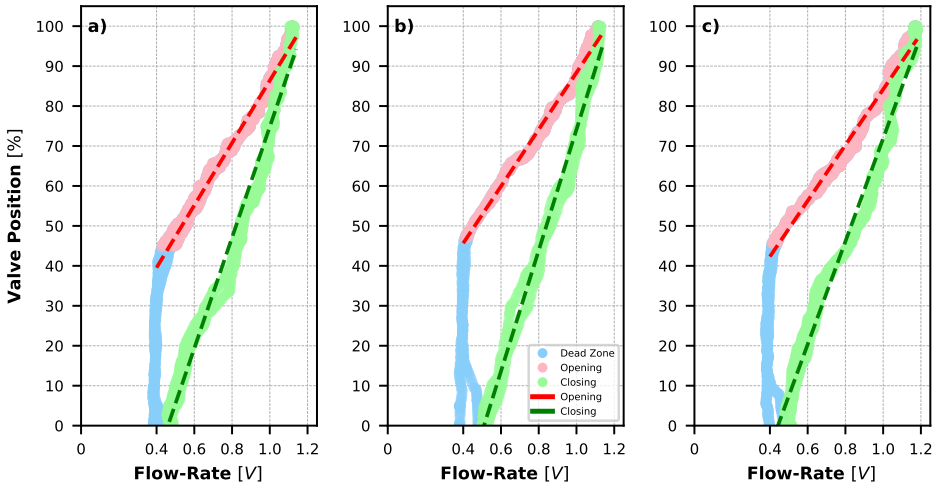

Figure 4.4: Experimental hysteresis loop examples for the tree valves, highlighting three regions: closing (green) and opening (red) characteristics, and "dead-zone" (blue). The superimposed green and red dashed lines refer to the estimated hysteresis model for valve closing and opening respectively.

while opening or closing, and a delay in the opening of the valve due to the presence of the dead-zone. From a control perspective, a non-compensated change in the valve opening command would generate a variation of the measured flow-rate larger than expected, thus resulting in an uneven control action during the opening and closing of the valve.

4.2.4 Control Scheme

To test the hypothesis that the hysteresis compensation enhances the performances of the control system, two different control schemes were developed. The two architectures both rely on the PID controller shown in Figure 4.5b. Given the positioning error vector $\boldsymbol{\omega}_{err} = \boldsymbol{\omega}_{des} - \boldsymbol{\omega}_{obs} = [\varphi_{err}\, \vartheta_{err}]^T$, where $\boldsymbol{\omega}_{des}$ and $\boldsymbol{\omega}_{obs}$ are the desired and measured tip position in a polar coordinate system, the controller's output is evaluated in three steps. At first, the proportional, integral and derivative output is evaluated such as

$$\boldsymbol{u}_i = \boldsymbol{K}_P \boldsymbol{\omega}_{err} + \boldsymbol{K}_I \int \boldsymbol{\omega}_{err} dt + \boldsymbol{K}_D \frac{d\boldsymbol{\omega}_{err}}{dt} \tag{4.7}$$

with $\boldsymbol{K}_P$, $\boldsymbol{K}_I$ and $\boldsymbol{K}_D$ representing the proportional, integral and derivative gains respectively. Assuming the linearity of the relation between the actuators output and the tip positioning error, in a local region around $\boldsymbol{\omega}_{obs}$, $\boldsymbol{u}_i$ is mapped into changes in tip forces $\boldsymbol{F}_i$.

To map the Cartesian components of the tip force into jet forces, Equation 4.5

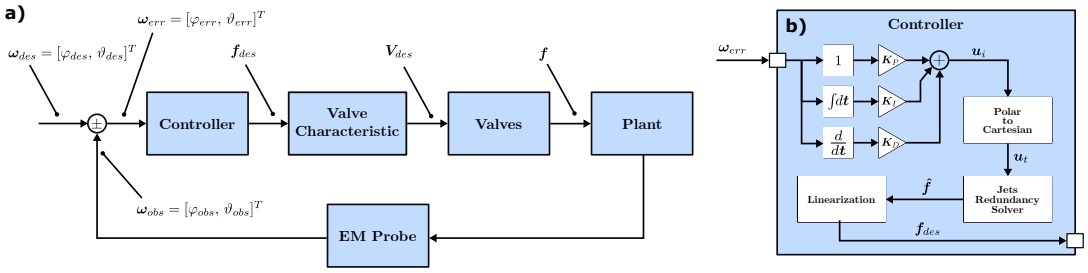

Figure 4.5: Control system architecture (a) and detailed view of the linearized PID controller (b).

is used, in this way obtaining $\hat{\boldsymbol{f}} = [\hat{f}_1\ \hat{f}_2\ \hat{f}_3]^T$. Ultimately, a compensation of the non-linear relation between jet forces $\hat{\boldsymbol{f}}$ and jets flow-rate $\boldsymbol{f}$ is performed using the inverse of calibration curves in Figure 2.6.

Here, the architectures of the two control systems deviate. In particular, in the non-compensated implementation (Figure 4.5a), the controller's output is directly fed into conversion block that, considering only the ideal valve's characteristic (closing curve), transforms the the desired flow-rate $\boldsymbol{f}_{des}$ into desired valve position $\boldsymbol{V}_{des}$. The latter becomes the input to the actuation system.

On the other hand, in a second implementation of the control system (Figure 4.6a), a Feed-Forward (FF) hysteresis compensation term is introduced. Starting from a known valve hysteresis model, the FF[1] block (Figure 4.6b) is used to quickly act bringing the flow-rate to the desired set-point ($\boldsymbol{f}_{des}$), in this way reducing the delays generated by the valve asymmetrical responsiveness. Given the flow-rate set-point $\boldsymbol{f}_{des}$ and error $\boldsymbol{f}_{err}$, the hysteresis compensation block acts such as

$$\boldsymbol{f}_{err} = \boldsymbol{f}_{des} - \boldsymbol{f}_{obs} \tag{4.8}$$

$$\begin{cases} h(\boldsymbol{f}) = h_{close}(\boldsymbol{f}) & if\ \boldsymbol{sign}(\boldsymbol{f}_{err}) > 0 \\ h(\boldsymbol{f}) = h_{open}(\boldsymbol{f}) & if\ \boldsymbol{sign}(\boldsymbol{f}_{err}) < 0 \\ h(\boldsymbol{f}) = h(\boldsymbol{f}) & otherwise \end{cases} \tag{4.9}$$

$$\boldsymbol{V}_{des} = h(\boldsymbol{f}_{des}) \tag{4.10}$$

where $h_{open}(\boldsymbol{f})$ and $h_{close}(\boldsymbol{f})$ refer to the opening and closing model of the ECV respectively. Such an approach allows to quickly switch between the two curves of the model to promptly adjust the output flow-rate to the desired values. However, when $\boldsymbol{f}_{obs}$ approaches $\boldsymbol{f}_{des}$, inaccuracies of the hysteresis model and the

[1]Even if the controller relies on a feedback from the sensors, it is still referred to as "Feed-Forward" to highlight its immediate response to a modelled disturbance such as the hysteresis.

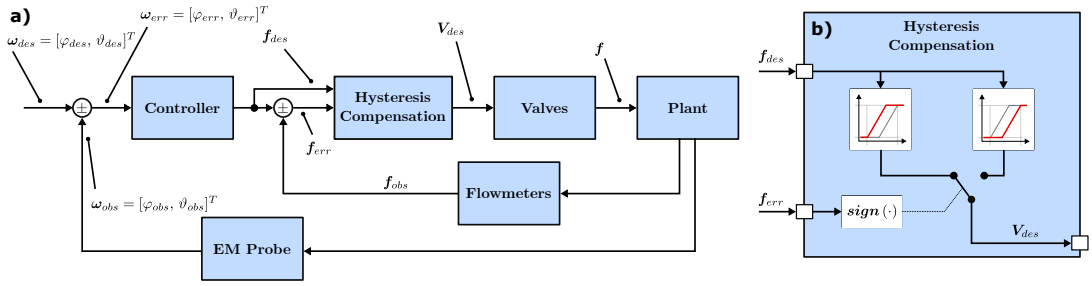

Figure 4.6: Hysteresis compensated closed-loop control architecture (a) and detailed view of the FF module (b).

noise superimposed to the measured flow-rate generate a continuous oscillations of the observed signal around the desired flow-rate value. For this reason, a safety offset ($\boldsymbol{f}_{off}$) is added to $\boldsymbol{f}_{des}$ (Equation 4.11) such that $\boldsymbol{f}_{obs}$ never exceeds $\boldsymbol{f}_{des}$ during the opening operation of the valve. As a consequence, when closing the valve, a short delay, proportional to $\boldsymbol{f}_{off}$, will be experienced before the compensation box switches from $h_{open}(\boldsymbol{f})$ to $h_{close}(\boldsymbol{f})$.

$$\boldsymbol{V}_{des} = \boldsymbol{h}(\boldsymbol{f}_{des} - \boldsymbol{f}_{off}). \tag{4.11}$$

4.3 Evaluation

Experimental evaluation of the proposed closed-loop control schemes was conducted to assess the influence of the hysteresis loop on the behaviour of the HJ's tip, the ability of the FF block to account for the asymmetric flow-rate characteristics and the performance of the controller in leading the endoscope's tip along a predefined trajectory. The experimental set-up used for the following tests is described in Figure 2.8, while the HJ device, fabricated for the tests, presented a slight pre-bending of about 17 deg (ϑ_{pb}) at $\varphi_{obs} \simeq 0$. The control algorithm was designed using python nodes in a Robot Operating System (ROS, Kinetic Kame) environment and was executed on an Intel Xeon powered machine (CPU E5-1660 v4, 3.2GHz). Manual tuning of the proportional and integral gains was performed to achieve an acceptable balance between transient response and stability of the system. $\boldsymbol{K}_D$ was set to zero. Test specific results for the evaluation of the hysteresis compensation and trajectory following algorithms are detailed in the following subsections.

4.3.1 Hysteresis Compensation

The test, executed with $\boldsymbol{z}_b$ aligned with the gravity vector, consisted of supplying a set of one ascending and one descending ϑ_{des} set-point ramps to the controller, while the control action on φ was disabled (e.g. all PID gains set to null). Each step in ϑ_{des} has an amplitude of 10 deg. The ascending ramp starts at 20 deg, a value just above ϑ_{pb}, and ends at 120 deg. The opposite applies to the descending ramp, with ϑ_{des} reaching a lower final value of 10 deg. A new ascending or descending step is automatically provided as soon as ϑ_{obs} reaches a steady-state status and the error drops below a prescribed threshold.

The tests aim was to evaluate the control system responsiveness to a new ϑ_{des} in terms of time needed to achieve a regime state and time to complete the task. Concurrently, the asymmetric set-point ramps allow the ϑ_{des} to decrease below the ϑ_{pb}, in this way requiring an action against the tether's pre-bending to achieve such elevation. In fact, in an ideal ($\vartheta_{pb} = 0$) configuration, J_2 would be the only jet required to accomplish the task, while, due to the pre-bending, the synchronous actuation of both J_1 and J_3 is required to achieve ϑ_{des} below ϑ_{pb}. Both the implemented controllers were tested and the results are shown in Figure 4.7.

The time-series in Figure 4.7c highlight the asymmetry in the ascending and descending paths of the HJ's tip when a non-compensated control scheme is used. As predicted in Section 4.2.3, such a control approach results in an aggressive action during the ascending section, which coincide with the opening of the valve. Inversely, during the descending portion of the path, the control action remains more gentle. As a direct consequence of this two opposite behaviours, the median time required by the controller to stabilize the tip at a desired elevation is 10.43 s and 31.40 s for the ascending and descending sections respectively (Figure 4.7a and e). Moreover, an unstable behaviour arises when the tip is required to achieve elevations below the pre-bending value. Here, the flow-rate asymmetric characteristics prevent the controller to rapidly adjust the jets' propulsive forces, in this way generating self-sustaining oscillations of the tip.

Conversely, Figure 4.7d shows how the compensated control scheme successfully counteracts the asymmetry of valve response, thus generating comparable ascending and descending paths. This is particularly clear in Figure 4.7b and f where the median time to reach a steady-state is 5.22 s and 7.63 s for the ascending and descending tasks respectively. One of the reasons for a longer descending times is to be found in the establishment of an oscillatory flow-rate control action generated by the FF compensation block for ϑ_{des} ranging from 70

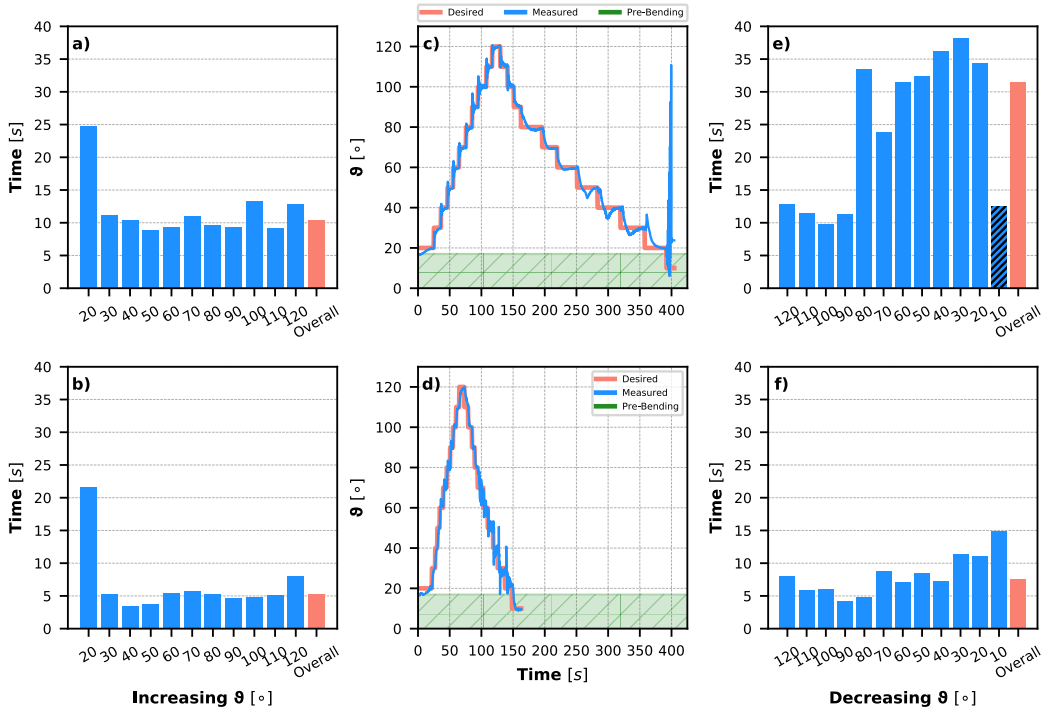

Figure 4.7: Results for ϑ closed-loop control tests performed using the HJ endoscope. The tests were executed with the HJ base longitudinal axis aligned with the gravity vector. Two different control approaches were tested: direct wrench control (a), c) and e) and hysteresis compensation control (b), d) and f). In c) and d), the shape of the set-point ramp is visible (red) together with the measured ϑ_{obs} values (blue), while the pre-bending values are indicated by the hatched area (green). The bar plots indicate the time the controllers need to stabilize the tip of the endoscope at a given set-point during the ascending (a) and b)) and descending ramps (e) and f)). The red bars indicate the median time-to-regime value, while the hatched bar in e) refers to the last descending step, incomplete due to instability.

to 20 deg. Despite these fluctuations, the controller was successful in stabilizing the tip and position it at an elevation of 10 deg.

In both Figure 4.7c and d, the protracted time to steady-state experienced at the beginning of the test ($\vartheta_{des} = 20$ deg) is caused by the initialization of the filters used to reduce the noise of the measured position signals.

4.3.2 Trajectory Tracking

With improved stability and shorter transient period demonstrated for control of ϑ, the hysteresis compensated controller was further evaluated in a trajectory following test. For this experiment, the controllers for both ϑ and φ coordinates were enabled to achieve a 3D motion of the HJ's tip. The trajectory, in a flattened polar reference system (Figure 4.8b), consists of a zig-zag movement of the endoscope's tip starting from the rest position ($\boldsymbol{\omega}_{obs} = [0\ \vartheta_{pb}]$); resulting in a 3D trajectory as shown in Figure 4.8a. The φ_{des} evolves in the range 0 deg to

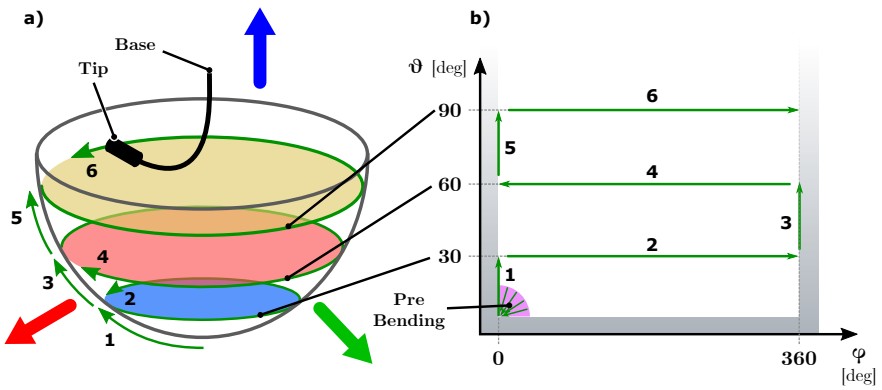

Figure 4.8: Representation of the desired trajectory in a a) 3D Cartesian reference frame and in a b) flattened Polar reference frame. In both a) and b) the sequence of movements is illustrated by green numbered arrows.

360 deg, or vice versa, with a step size of 10 deg, while ϑ_{des} varies from 30 deg to 90 deg with a 30 deg wide step size. Before increasing or decreasing the value of φ_{des}, the trajectory generator algorithm waits for ϑ_{obs} to achieve a steady-state. A step in ϑ_{des} is performed at the beginning of the test and each time the φ_{des} completes a full revolution.

Figure 4.9a and b show the experimental results from a test example for the two controlled variables ϑ and φ, while Figure 4.9c and d describe the non-negative values of the difference between the measured and the desired positions. For both ϑ and φ, this error is evaluated after a steady-state regime is achieved, thus excluding the error generated by ϑ and φ transient periods. Results show how, during 90% of the duration of the test, the error remains below 5 deg, specifically 3.30 deg and 4.24 deg for ϑ and φ respectively. Nevertheless, if a φ_{err} is evaluated for each available data point, localized spikes in the measured φ coordinates are visible and exceed 25 deg. Such an evaluation of the error does not ignore the system transients, however, it becomes necessary to highlight that wider oscillations of the tip were observed for φ_{obs} (with a 90^{th} percentile value of 9.77 deg). In all of these cases, the controller was able to stabilize the tip and drive it towards φ_{des}.

In Figure 4.10, ϑ_{err} and φ_{err} tracking errors are mapped against the controlled coordinates ϑ and φ. Such a representation shows how the errors evolve along the trajectory. Specifically, Figure 4.10a and c illustrate how ϑ_{err} and φ_{err} change at three different tip elevations. The median values of ϑ_{err} remains fairly constant across the three ϑ_{des} levels, with median errors measuring 0.71, 0.67 and 1.13 deg at 30, 60 and 90 deg elevation levels. The cause of an higher ϑ_{err} value registered at 90 deg elevation is to be found in the tubing re-arrangement that occurs at these wide bending angles, visible in Figure 2.10. With this tubing configuration

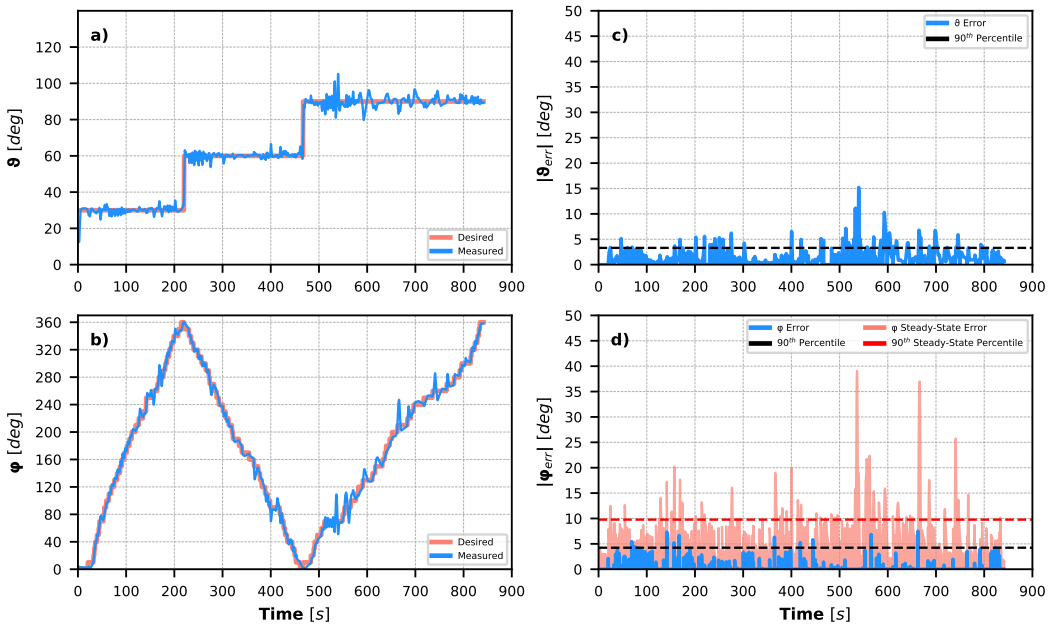

Figure 4.9: Results from a trajectory following example showing the time series of set-point and measured tip position for a) ϑ and b) φ. In c) and d) the regime errors are shown for ϑ and φ respectively (blue), while the black dashed line indicates the 90^{th} percentile of the data distribution. In d) the full set of φ_{obs} is shown, together with a red dashed line indicating the value of its 90^{th} percentile.

and when a change in φ is requested, the endoscope's tip has to reach lower ϑ_{obs} values to allow the tubes to re-arrange in a different stable position. When this happens, the tip goes back to the desired elevation and reaches φ_{des}. This a behaviour becomes more evident in Figure 4.10b, where the evolution of ϑ_{err} is shown as a function of φ_{des}. The median values of the ϑ_{err} follow a sinusoidal trend, with minimum values reached approximately around the six stable φ_{des} positions that characterize the HJ's tip: 0, 120 and 240 deg for a single jet actuation, and 60, 180 and 300 deg for a dual jet actuation. The transition in between these values involves a change in ϑ_{obs} in this way causing a wider ϑ_{err}.

With regard to φ_{err}, Figure 4.10c shows a decrease in its median value at high elevation angles, attributable to the increased radius of the revolution path. The consequent longer distance travelled by the tip to cover the 10 deg step in φ_{des}, allows the controller to finely position the tip at the desired φ_{des} value. Similar behaviour seen in Figure 4.10b is also observed in Figure 4.10d. In both cases, the non-perfect correspondence between stable positions and minimum error values is attributable to fabrication defects such as the tether pre-bending.

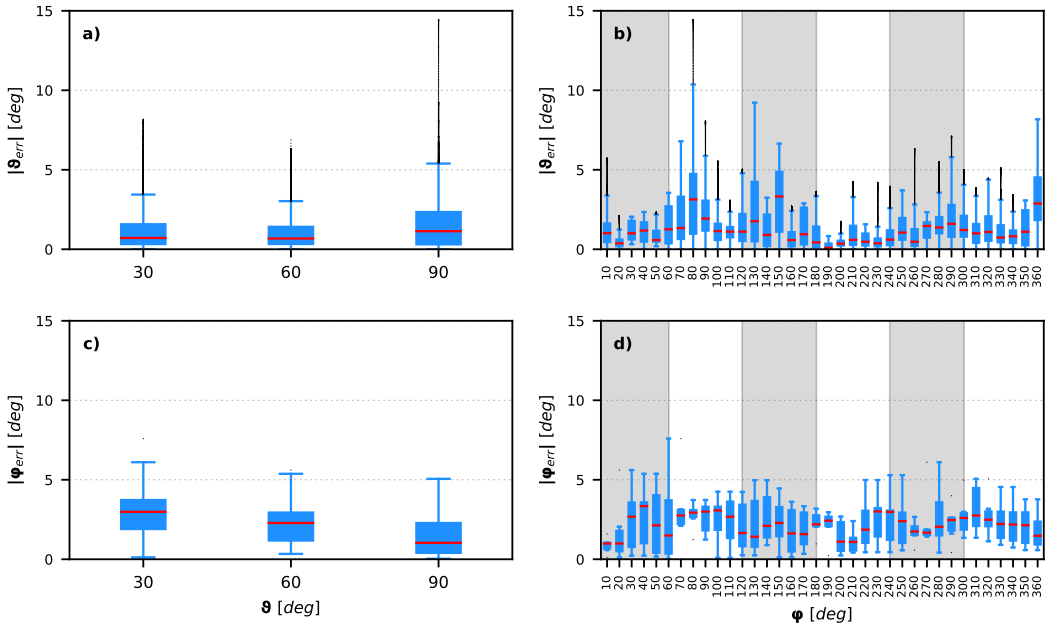

Figure 4.10: Results from a trajectory following example (Figure 4.9) showing the ϑ and φ error distributions as a function of ϑ and φ: a) $|\vartheta_{err}|$ vs. ϑ, b) $|\vartheta_{err}|$ vs. φ, c) $|\varphi_{err}|$ vs. ϑ, d) $|\varphi_{err}|$ vs. φ.

4.3.3 Repeated Trials

To assess the consistency of the results presented in the previous sections, the trajectory following task was repeated multiple times, while all the system's parameters remained unchanged. Figure 4.11a and b compare the resulting distribution of $\boldsymbol{\omega}_{err}$ registered across 5 test repetitions. The median and magnitude of the "Overall" boxes indicates how ϑ_{err} and φ_{err} remain consistent for each test repetition reaching a median value of 0.91 and 1.90 deg respectively.

A description of the duration of the trials is presented in Figure 4.11c. In the boxplots shown, the time-to-completion of each tip revolution at different elevations is reported, both in terms of absolute time since the start of the test or relative time since the end of the previous revolution. The median time required to complete the full task was 914 s ($\simeq$15 min), while the elapsed time between the end of two consecutive revolutions increases quadratically with ϑ_{des}.

4.4 Discussion

The results presented in this chapter indicate how the implementation of a model-free closed-loop control strategy represents a viable solution for manipulating a tip actuated (or TFA) soft continuum endoscope. The selected polar coordinate system, describing the position of the endoscope's tip, perfectly fits the kinematic

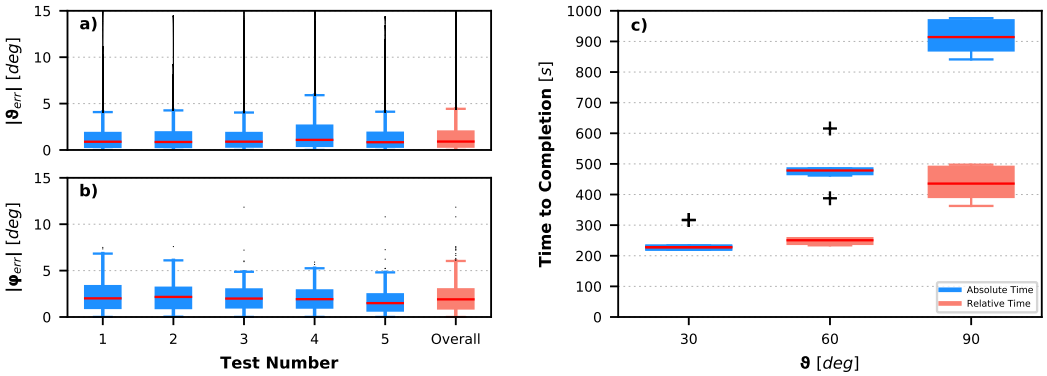

Figure 4.11: Results from repeated trials (n = 5) showing the positioning errors relative to the controlled variables a) ϑ and b) φ. The positioning error is evaluated as the absolute value of the difference between the set-point and the measured values. Trajectory following time to task completion (c). Each task is intended as a full, 360 deg, φ trajectory, at three different ϑ elevations: 30, 60 and 90 deg. The box corresponding to the 90 deg task is indicative of the entire duration of the test, while, at ϑ_{des} = 30 deg the the absolute and relative time-to-completion coincide.

characteristics of the HJ, while defining a convenient and intuitive approach to the design of a control scheme. The resulting automatic position control architecture is based only on a knowledge of the magnitude and direction of the forces acting at the tip, and does not require a kinematic or dynamic model of the soft continuum robot, thus not being constrained by quasi-static model assumptions or the computational cost of dynamics modelling. Position feedback was provided by EM sensors, although the same or similar information could be provided by more economical off-the-shelf components such as IMUs or image sensors in combination with visual odometry methods.

An hysteretic behaviour was observed in the HJ actuation system. The implementation of a control strategy that does not take into account this non-linearity of the valves, resulted in poor performance of the controlled plant in terms of responsiveness and stability of the endoscope's tip. The need for enhanced system performance led to the implementation of a hysteresis compensated control system. Such a controller is based on an a-priori knowledge of the hysteresis loop which was modelled using two linear curves. The features of the custom valves used during the experimental evaluation (ECV) and specifically, the linear input-output characteristic of such devices, promoted the adoption of a simple modelling approach and the achievement of a reactive and stable control action.

Multiple trajectory following trials were performed to test the ability of the control strategy to lead the HJ's tip along a predefined path. The shape of the trajectory was selected in order to enable an automatic scanning of the stomach wall. The implemented zig-zag movements can be tuned to achieve a

full coverage or visualization of the gastric mucosa, avoid overlapping paths and, at the same time, implement simple motion trajectories. Experimental results show that the proposed controller was capable of controlling the position of the endoscope's tip along the required trajectory in a stable and accurate fashion (median values for ϑ_{err} and φ_{err}, 0.91 and 1.90 deg respectively). The design of the HJ bending segment generated unwanted fluctuations of the tip during the transition between two stable positions. Despite the positioning error caused by these oscillations, the closed-loop control strategy was able to redirect and stabilize the tip on the desired path. Results from repeated trials proved the consistency of the control action across 5 test in terms of amplitude of the error and time needed to complete the task (914 s). Moreover, even if the proposed trajectories are not directly comparable, a 20% decrease in the time needed to complete the task up to an elevation of 60 deg was observed with respect to [18].

The total amount of water used for each test was estimated integrating the flowmeter information in time. A volume of 7.21 $\pm$0.6 liters was used. Despite this high amount of water needed to complete the task, the excess of liquid can be easily removed from the stomach, thanks to the suction ports placed at the tip of the endoscope.

4.5 Conclusions

A position control system operating in polar coordinates was implemented to steer the HJ in the free space. The control system modulates the components of the force, F_φ and F_ϑ, acting at the tip of the HJ to drive it along a user defined trajectory. The presence of a hysteresis loop in the actuators characteristic represented a non negligible limitation in achieving high performance controlling capabilities, both in terms of time required to reposition the endoscope and stability of the movements. A control strategy that considers the actuation hysteresis and promptly compensates for its effects was implemented, leading to improved stability and controllability of the soft manipulator. The proposed method represents a reliable approach to the control of tip actuated soft continuum manipulator, providing solid foundations to the implementation of advanced autonomous capabilities.

Chapter 5

Obstacle Detection for Autonomous Navigation of a Soft Continuum Robot for Gastric Cavity Inspection

5.1 Introduction

Inspection of the gastric cavity relies on manual actuation of a classic FE operated by a skilled GE. This is to ensure that the procedure is properly performed and the quality of the diagnosis meets the desired standards. Alternative approaches to the inspection of GI cavities exist and they are mainly based on robotic actuation to deliver a reliable inspection procedure [85]. Despite the closed-loop control strategies adopted to help the physician in performing the endoscopy, an experienced user is still required to guarantee the success of the procedure.

This approach represents a viable solution for the majority of the endoscopic procedures, however, when population based gastric cancer screening programmes have to be implemented, the ability to include non-expert personnel in the pool of suitable users, would allow wider population screening to be achieved and reduce the time needed for the completion of the programme. Autonomous strategies are therefore needed to compensate for the lack of experience of the novice operator.

The automation of tasks, especially in the field of MIS, has been extensively studied over the past years. Such autonomous behaviours allow the surgeon to focus on the primary objective of the surgery procedure, while the robotic platform would be responsible for more repetitive tasks. Examples of tasks automation have been presented for autonomous tissue retraction [121], suturing [134, 135]

and tissue resectioning [136]. In the field of FE for the GI tract inspection, the work introduced in [85] demonstrate how the introduction of a minimum level of autonomy allows the non-expert user to achieve performances comparable to those by a fully trained GE.

The implementation of autonomous capabilities is based on two major assumptions: a basic knowledge of the environment that the robot is required to explore and the ability of the control system to localize the robot's end-effector. The combination of these two elements enables the navigation inside the environment and allows the execution of collision avoidance strategies to reach a generic goal position. However, if the localization of the end-effector can only be achieved by directly measuring its pose or estimating it using sensor-fusion techniques, a map of the environment is not always available or easily accessible. In the case of navigation inside anatomical cavities, pre-operative 3D imaging provides the control system with the required information to perform the inspection [137]. This approach assumes the possibility to access medical imaging techniques before the procedure, in this way resulting in prolonged times to perform the cavity inspection and a considerable increase of the cost of the procedure. Moreover, possible changes in the anatomy in between images acquisition and endoscopic procedure must be considered.

Without an a-priori map of the environment, the navigation must rely on a different method to deliver a successful inspection procedure. In this scenario, the ability to recognize a possible interference between the robot's end-effector and environmental features (obstacles) becomes essential and triggers successive measures that allow the robot to escape collision status. Obstacle detection algorithms rely on a sensory information to identify the collision event. In [138], the combination of the information provided by a continuum kinematic model and sensor feedback enable the implementation of a collision detection strategy. A similar approach, developed in [139], relies on a measure of the closed-loop control effort to understand when the end-effector is not able to reach a desired configuration as a result of a collision. In both these methods, the detection algorithm is based on a double threshold approach to detect and confirm the collision, in this way discarding false positives and enhancing the sensitivity of the method.

The ability to detect collisions allows a level of environment mapping and division into free-space and restricted areas. Once the distribution of these regions is known, a strategy to navigate towards the goal pose can be identified by using path planning techniques. Well known examples in the field of continuum robotics for medical applications include motion planning applied to concentric

tube robots [140, 141], steerable needles [142] and Continuum Reconfigurable Incisionless Surgical Parallel (CRISP) robots [143].

In this Chapter, three steps towards the implementation of autonomous exploration of the gastric cavity using the HJ endoscopic platform are described. An obstacle detection algorithm, based on [138] is presented. A strategy for building a map of the explored environment and registering the position of the detected obstacles is described. Finally, an online motion planning technique is introduced, allowing the HJ to react to collisions an reposition to continue the inspection until an acceptable portion of the environment is explored. A final section presents an experimental validation of the obstacle detection algorithm, while the full autonomous behaviour was tested in a simulated environment.

5.2 Principle of Operation

This section describes three methods developed to enable the implementation of an autonomous behaviour that allows the HJ endoscope to perform an unsupervised inspection of the gastric cavity. For this purpose, the HJ employs all the functionalities described in the previous chapters. An approach to obstacle detection is firstly presented, relying on both a measure of the endoscope's tip pose and a kinematic model of the bending section. Then a method for building a 2D map of the explored environment is proposed. Given a map of the free-space and obstacles, a path planning and repositioning scheme is introduced to allow a collision-free movement in between obstacles and enable complete exploration of the environment.

5.2.1 Obstacle Detection

5.2.1.1 CM Kinematics

The kinematic modeling of the HJ low-stiffness section was previously introduced and further discussed in [18] and [144] respectively. The modelling approach is based on the Cosserat rod theory which uses an arc-length parametrized homogeneous transformation to describe how a rod in an pre-curved unloaded configuration deforms under the action of a known external wrench (e.g. gravity or actuation forces). In this way, given the set of forces applied at the HJ's tip, measured using the flowmeters, and considering the mechanical characteristics of the bending section, the model returns the full pose of the tip $\boldsymbol{T}_g$ in a Cartesian reference system, with respect to the base coordinate frame. To achieve this, the

unknown mechanical properties of the bending section, including stiffness (E), pre-bending (u and v) and length (L) of the soft section, must be estimated. A two step calibration process, relying on a parameters optimization strategy, was deigned to achieve fine tuning of the required mechanical properties. The experimental set-up, used for the calibration process was previously introduced in Section 2.3 and described in Figure 2.8. It employs two EM 6-DoF probes, one at the HJ's base, which indicates the orientation of the gravity vector with respect to the endoscope, and one at the tip, used as a position and orientation gold-standard measurement $\boldsymbol{T}_t$.

Initially, with the endoscope longitudinal axis aligned with the gravity vector, u, v and L were estimated solving the minimization problem that aligns $\boldsymbol{T}_g$ with $\boldsymbol{T}_t$:

$$\underset{u,v,L}{\operatorname{argmin}}(e_1 + e_2)^2 + e_3 \tag{5.1}$$

where e_1 and e_2 are the angular offsets between $\boldsymbol{T}_g$ and $\boldsymbol{T}_t$ x- and y axis, while e_3 represents the Euclidean distance between $\boldsymbol{T}_g$ and $\boldsymbol{T}_t$ origins. The initial values of the parameters vector $\boldsymbol{\lambda_1} = [u, v, L]$ were determined by manually adjusting their values using sliders on a user interface in the attempt to align $\boldsymbol{T}_g$ to $\boldsymbol{T}_t$, while receiving a visual feedback of the tips poses in RViz (3D visualization tool for ROS).

With these known pre-bending and length values, a second step of the calibration process involved the estimation of the bending section stiffness by applying known forces to the tip via the water jets and measuring the deflection. To account for inaccuracies in the nozzle geometry that could influence the evaluation of the jet forces $\hat{\boldsymbol{f}}$, three additional parameters were added to the estimation problem. This parameter vector $\hat{\boldsymbol{f}}_{err} = [\hat{f}^1_{err}\ \hat{f}^2_{err}\ \hat{f}^3_{err}]$, combined with the jet-force calibration curve $m(\boldsymbol{f})$ (Figure 2.6), results in a $\tilde{m}(\boldsymbol{f})$ with a narrower or broader aperture. The parameter estimation is performed solving the minimization problem:

$$\underset{E,\hat{\boldsymbol{f}}_{err}}{\operatorname{argmin}} \parallel e_1 \parallel + \parallel e_2 \parallel + \parallel e_3 \parallel . \tag{5.2}$$

To obtain an initial estimation of E, the HJ's base was oriented 90 deg with respect to the gravity vector, so that the tip of the endoscope bends in response to the gravity. In this configuration, the optimization of Equation 5.2 was performed, restricting the parameter estimation to E only. Subsequently, the base was re-aligned to the gravity vector and, in turn, the i-*th* jet was powered

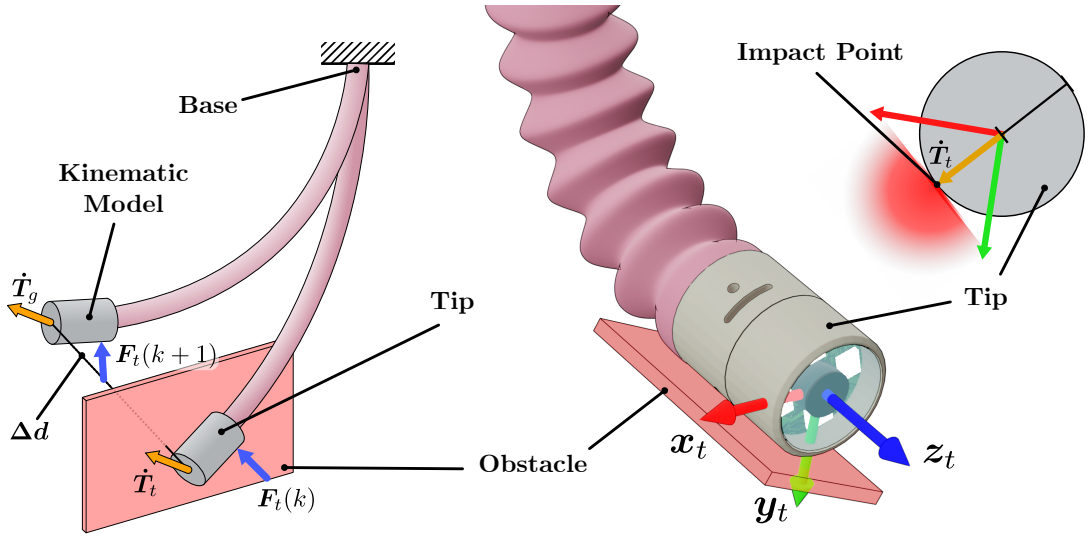

Figure 5.1: Representation of the information provided by the kinematic model and the EM probe at the tip of the HJ. Position, velocity and force applied at the tip are used to implement the obstacle detection algorithm.

to its maximum output. For each jet, the optimization was performed restricting the unknown parameters to E and $\hat{f}^i_{err}$. Finally, using the initialization values for the full set of parameters $\boldsymbol{\lambda_2} = [E,\ \hat{f}^1_{err},\ \hat{f}^2_{err},\ \hat{f}^3_{err}]$, a final minimization was executed while all the jets were powered to their maximum output.

Additional details on the implementation of the kinematic model are not further discussed here, as they are considered out of the scope of this chapter.

5.2.1.2 Detection Algorithm

In an unstructured environment such as the gastric cavity, the stomach wall constrains the movements of the endoscope. The shape of the HJ workspace and the lack of a fully controllable endoscope tip, leaves part of the workspace unreachable. In this scenario, most of the obstacles remain outside of the camera FoV, making it impossible for the user to promptly react to the collision or for an image-based obstacle detection algorithm to properly operate. The ability to identify a collision event would allow the user or the automatic control scheme to acknowledge the presence of an obstacle that does not allow continuation along the current path. Therefore, the detection of the collision event is critical for triggering a successive reaction.

The proposed obstacle detection algorithm uses a combination of information coming from the measured ($\boldsymbol{\omega}_t$) and estimated ($\boldsymbol{\omega}_g$) tip pose provided by the EM and kinematic model respectively; expressed in a polar coordinate system as explained in Section 4.2.2. The effects of a collision on $\boldsymbol{\omega}_t$ and $\boldsymbol{\omega}_g$ are different and this difference can be used as an instrument to describe the collision event.

Specifically, $\boldsymbol{\omega}_g$ is not influenced by the the presence of an obstacle along the path of the tip, in this way it results in an estimation of the tip pose as if the collision never occurred. Contrarily, $\boldsymbol{\omega}_t$ experiences an instant drop in the magnitude of its velocity vector. By monitoring the difference Δv between $\dot{\tilde{\boldsymbol{T}}}_g$ and $\dot{\tilde{\boldsymbol{T}}}_t$ (Figure 5.1), where $\dot{\square}$ represents the time derivative operator, such that $\dot{\tilde{\boldsymbol{T}}}_g$ and $\dot{\tilde{\boldsymbol{T}}}_t$ refer to the measured and estimated tip translational velocities, a first assumption of the presence of an obstacle can be made. Assuming that the odometry of the robot's tip is only known in a polar reference frame, the nomenclature $\tilde{\boldsymbol{T}}$ is here used to indicate the Cartesian position obtained starting from $\boldsymbol{\omega} = [\varphi\ \vartheta\ r]^T$ and considering a unitary value for r

$$\begin{aligned} \tilde{x} = &\quad r \cdot sin(\vartheta) \cdot cos(\varphi) \\ \tilde{y} = &\quad r \cdot sin(\vartheta) \cdot sin(\varphi) \\ \tilde{z} = &\quad\quad r \cdot cos(\vartheta). \end{aligned} \tag{5.3}$$

Despite the optimal parameters estimated during the calibration process, the kinematic model is based on the assumption of homogeneity of the CM's body. In this way, the model well describes the behaviour of the HJ bending segment in most of its configurations, until a tubing re-arrangement occurs inside the soft sleeve. In this circumstance, a higher speed difference between the two tips is experienced, even though a collision did not occur. To account for these modelling inaccuracies, the speed difference is weighted using the time derivative of the norm of the force applied at the tip ΔF. The founding idea is that, assuming the absence of moving obstacles, if a high velocity difference is experienced when no change in the actuation force is commanded, then this event is attributable to modelling errors.

To reduce the number of false positives, an additional signal confirms that the supposed collision in fact occurred. The euclidean distance (Δd in Figure 5.1) between the $\tilde{\boldsymbol{T}}_g$ and $\tilde{\boldsymbol{T}}_t$ is considered for this purpose. When a possible collision occurs, the algorithm monitors how Δd evolves in time and, if it continues increasing, the presence of an obstacle is confirmed. These signals and triggers are evaluated as follow:

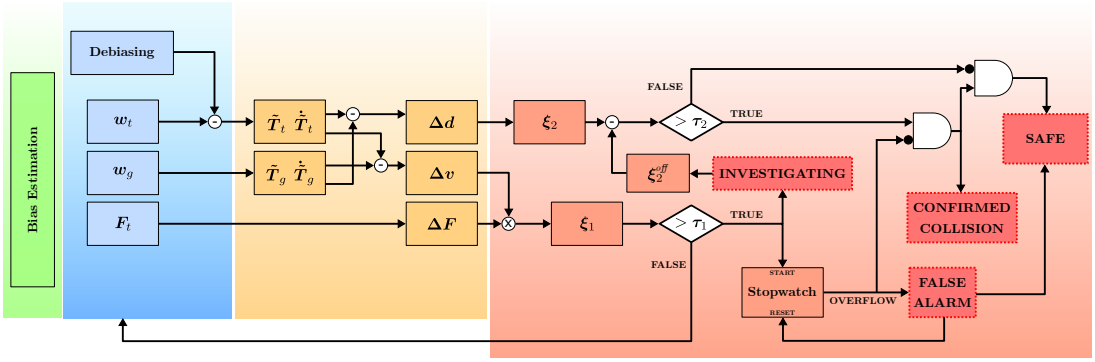

Figure 5.2: Flow chart for the obstacle detection algorithm, highlighting the initial bias estimation (green), data collection and debiasing (blue), signals evaluation (yellow) and collision detection logic. The four algorithm outputs are also shown (dashed red boxes): safe, investigating, false alarm and confirmed collision

$$\begin{aligned} \Delta v &= || \dot{\tilde{\boldsymbol{T}}}_g || - || \dot{\tilde{\boldsymbol{T}}}_t || \\ \Delta F &= \frac{|| \boldsymbol{F}_t(k+1) || - || \boldsymbol{F}_t(k) ||}{dk} \\ \Delta d &= || \tilde{\boldsymbol{T}}_g - \tilde{\boldsymbol{T}}_t || \end{aligned} \tag{5.4}$$

$$\begin{aligned} \xi_1 &= \Delta v \cdot \Delta F \\ \xi_2 &= \Delta d. \end{aligned}$$

The implementation of the obstacle detection algorithm is detailed in Figure 5.2. Initially, the position offsets between $\boldsymbol{\omega}_g$ and $\boldsymbol{\omega}_t$ are evaluated by averaging the data acquired over a period of 3 s (arbitrarily selected to ensure reliable mean values). The resulting φ_{off} and ϑ_{off} are used to debias $\boldsymbol{\omega}_t$. Tip Cartesian position and velocity are thus evaluated and combined together as shown in Equation 5.4, resulting in Δd and Δv. The two triggering signals ξ_1 and ξ_2 are also evaluated. At each time step, if ξ_1 exceeds a user defined threshold τ_1, the possibility of a collision is investigated and the current value of ξ_2 is registered as ξ_2^{off}. At this point ξ_2 is zeroed by subtracting ξ_2^{off} from each new ξ_2 sample, in this way monitoring the change in Δd, starting from the onset of the investigation period. The investigation lasts for a time period defined by a stopwatch and, if no confirmation arrives in this time frame, a false alarm is triggered. Otherwise, if ξ_2 exceeds the threshold τ_2 before the stopwatch overflows, the supposed collision event is confirmed. Finally, the endoscope's tip is considered in a collision state until ξ_2 returns below τ_2. When this happens the tip return to its safe initial condition.

The detected collision is registered in the form of an impact point $\boldsymbol{\omega}_{coll} =$

$[\varphi_{coll}\ \vartheta_{coll}]^T$. To take into account the size of the end-effector, the impact point is moved away from the tip center, along the direction of the tip velocity vector $\dot{\boldsymbol{\omega}}_{coll}$ measured at the onset of the investigation status.

5.2.2 Mapping

Achievement of autonomous environment scanning requires the ability to keep track of the portions of the workspace already explored, the locations of unexplored regions and the positions of potential obstacles that could prevent the endoscope from reaching a desired position through a straight path. Such information may be provided by a map of the surroundings. To this end, a real-time construction of a map of the environment was implemented. The map localizes the position, in a 2D polar coordinate system, of three regions of the workspace: explored, unexplored and unreachable (e.g. obstacles). It consists of a 2D image with resolution φ_{max} by ϑ_{max}, with each pixel representing a 1 deg displacement in φ or ϑ coordinates. In the map, each workspace region is color-coded using white for the *unexplored*, green for already *explored* and red for *unreachable*. The map is periodically checked, for example when an additional increase in ϑ_{des} would exceed ϑ_{max}, and the ratio between unexplored and explored regions is evaluated, in this way defining the achieved percentage of coverage. If this value reaches a user defined threshold, the scanning ends.

The map is initialized as a completely white image and, while the endoscope moves along the desired trajectory, the $\boldsymbol{\omega}_{obs}$ coordinates are registered in the image as a green colored circle. When the endoscope's tip collides with an obstacle, the event is registered at the point $\boldsymbol{\omega}_{coll}$, in this way updating the unreachable domain of the map. Since the obstacles can only be described by the impact point $\boldsymbol{\omega}_{coll}$ and their shape or dimensions is not known a-priori, the map building method relies on assumptions to best represent such entities. A failure in mapping the dimensions of an obstacle could result in the presence of unexplored areas that are actually inside an obstacle, thus unreachable. In this way, the consequential low percentage of coverage will generate an uninterrupted and incomplete scanning procedure.

Considering the geometric characteristics of the environment the HJ is meant to explore (the stomach walls can be represented as a single continuous obstacle that limits the tip's movement along φ or ϑ), a continuous function was selected to describe the shape of the obstacles. Such a function $\boldsymbol{s}$ consists of a cubic spline that relies on $\boldsymbol{\omega}_{coll}$ and a series of artificial via points $\boldsymbol{\omega}_{via} = [\boldsymbol{\omega}_0^l\ \boldsymbol{\omega}_0^r \cdots \boldsymbol{\omega}_n^l\ \boldsymbol{\omega}_n^r]$.

When the scanning procedure starts, $\boldsymbol{s}$ is described by only two via points,

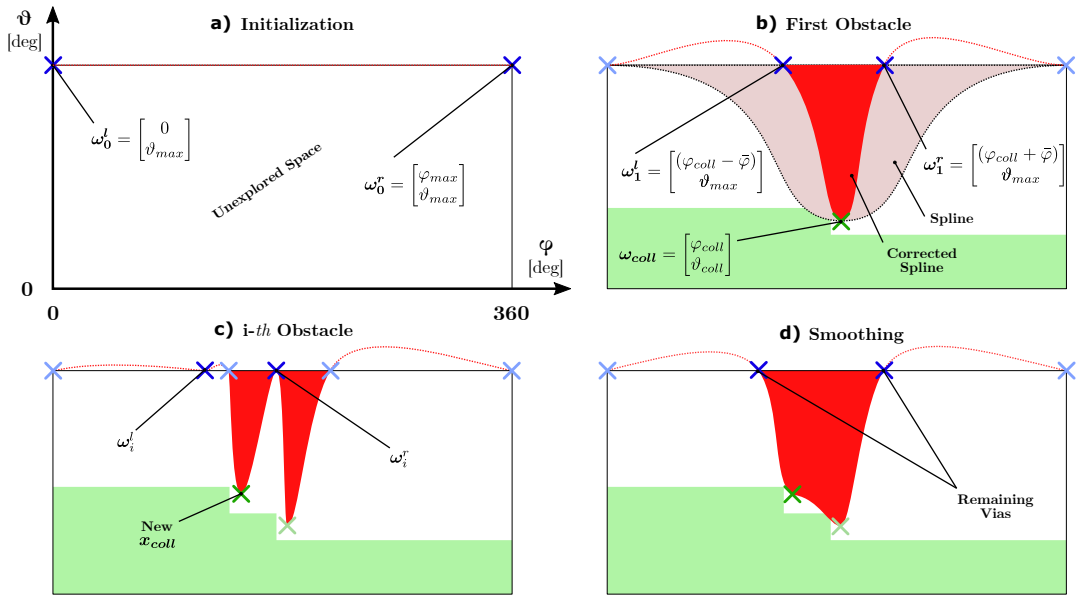

Figure 5.3: Obstacle forming algorithm based on a cubic spline function. The positions of the detected collisions (green crosses) are used as spline control points, while (b) artificial vias (blue crosses) are added to limit the aperture of the curve. In c) and d) the obstacle merging and spline smoothing techniques are shown.

$\boldsymbol{\omega_0^l}$ and $\boldsymbol{\omega_0^r}$, placed at $[0\ \vartheta_{max}]^T$ and $[\varphi_{max}\ \vartheta_{max}]^T$ respectively, such that $\boldsymbol{s}$ is a straight line at the top edge of the workspace as in Figure 5.3a. When the first collision is detected, a new spline control point is added at $\boldsymbol{\omega}_{coll}$, while two new via points are added in $\boldsymbol{\omega}_1^{l/r} = [(\varphi_{coll} \pm \bar{\varphi})\ \vartheta_{coll}]$ as shown in figure 5.3b. An appropriate selection of the parameter $\bar{\varphi}$ allows to restrict the aperture of $\boldsymbol{s}$, in this way determining the minimum size of the obstacles. The obstacle shaping algorithm continues adding control points and vias whenever a collision is experienced (Figure 5.3c), with the only exception of avoiding a left or right vias if a control point is within $\pm\bar{\varphi}$ from the current $\boldsymbol{\omega}_{coll}$. A final smoothing phase consists of eliminating the excess of via points that causes sharp variations in $\boldsymbol{s}$. This decimation process evaluates the distance between each via and the closest φ_{coll}, and removes the vias which are too close to a control point. By doing this, the spline peaks created by two collisions events, are merged in one single large obstacle (Figure 5.3d). The resulting area enclosed in between $\boldsymbol{s}$ and ϑ_{max} is marked as obstacle (coloured in red).

5.2.3 Path Planning

The ability to detect collisions and register the position of the obstacles on a map provide the HJ with the necessary information to enable autonomous navigation within an unknown environment. Despite this, an online method for generating

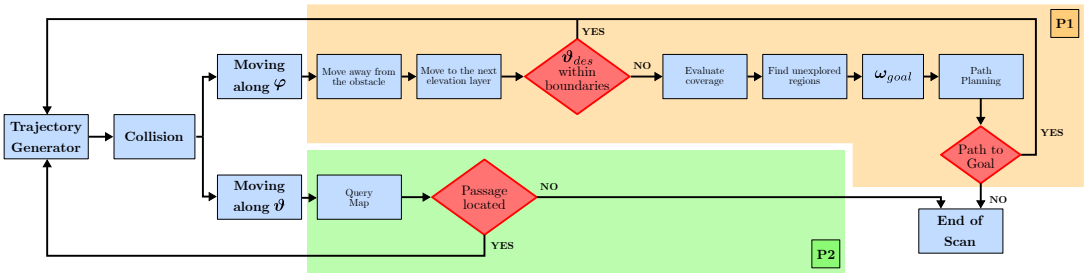

Figure 5.4: Finite-State machine describing the online path planning method used in the event of a collision with an obstacle. In yellow and green the reaction policies P1 and P2 are shown.

the desired trajectory that the endoscope's tip has to follow is required. As shown in Chapter 4, the combination of position closed-loop control and a static path planning algorithm that generates a static zig-zag trajectory, represents a suitable approach in an obstacle free environment. On the other hand, the decision making process triggered by the detection of a collision involves a modification of the desired tip path, aimed at moving away from the obstacle and re-planning the trajectory to achieve a desired position in unexplored regions, unreachable with the current planning approach.

The proposed online path planning scheme is based on the zig-zag trajectory generation, as shown in Chapter 4, while two main reaction policies were introduced and used in the event of a collision. By relying on the characteristics of the zig-zag trajectory, with a single coordinate φ_{des} or ϑ_{des} varying at all times, the selection of the reaction policy is implemented by tracking the changes in $\boldsymbol{\omega}_{des}$. If φ_{des} was evolving when the collision is detected, then policy P1 is considered, otherwise policy P2 is used. The entire decision making process is shown in Figure 5.4 in the form of a finite-state machine.

The main trajectory generation algorithm generates a new set-point $\boldsymbol{\omega}_{des}$ considering its current value and the workspace boundaries, so that, for example, ϑ_{des} is incremented every time a full revolution is completed. When a collision is detected while the tip is moving along the φ direction, then P1 is executed.

The main purpose of P1 is to move the tip away from the obstacle, towards a safe configuration. To do so, φ_{des} is updated in the opposite direction with respect to its previous course. Therefore, ϑ_{des} is increased to allow the endoscope to explore the next elevation layer (Figure 5.5a). If this new value of ϑ_{des} remains in between the workspace boundaries, the main trajectory generation takes control and a new zig-zag scanning process begins. However, if ϑ_{des} is out of the allowed workspace boundaries (Figure 5.5a), the new elevation level cannot be reached by the endoscope's tip. In this scenario, the map is used to evaluate the

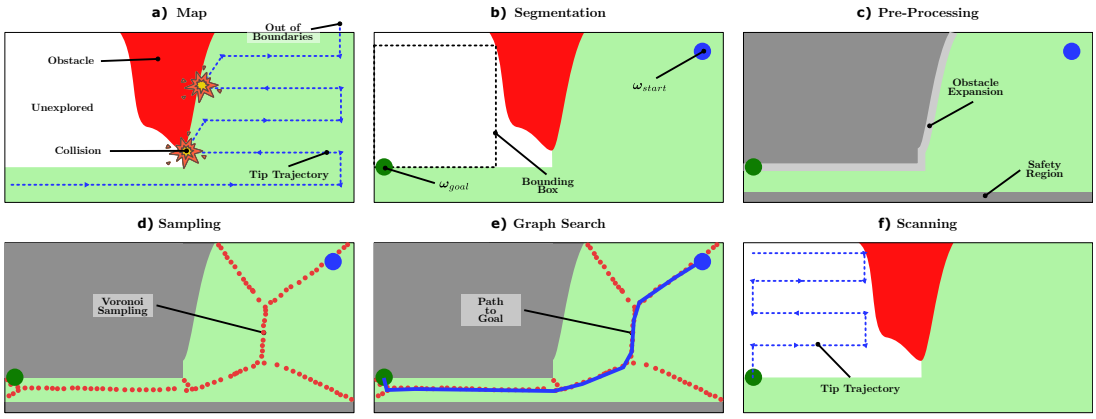

Figure 5.5: Detailed view of the main steps of P1. a) A new $\boldsymbol{\omega}_{des}$ out of the manipulator's workspace triggers the need for repositioning the tip in a different, unexplored, region of the map. b) The region of interest is located by segmenting the map, thus $\boldsymbol{\omega}_{goal}$ is evaluated. c) Additional collisions are avoided by expanding the obstacles. A safety region is included to prevent singular configurations of the manipulator. d) The free-space (green) is sampled using a Voronoi sampling algorithm. e) Dijkstra's search algorithm relied on the sampled free-space to find the shortest path that connects $\boldsymbol{\omega}_{start}$ to $\boldsymbol{\omega}_{goal}$. f) Once the tip reaches the goal position, a the normal zig-zag motion resumes.

coverage percentage. If this value is adequate, the exploration can be considered concluded, otherwise an approach that allows the tip to reach the unexplored regions is required.

This is achieved by processing the map. At first, the map is segmented to differentiate between regions of interest (e.g. unexplored portions) and the already-known environment (Figure 5.5b). The properties of each white unexplored region are evaluated in terms of their area and center of mass. The largest region in the set is finally selected. The position of this unexplored area is provided in the form of a $\boldsymbol{\omega}_{goal}$ which corresponds to the lower-left corner of the bounding-box enclosed in the selected area. This is built by seeding a 2 x 2 pixels rectangle at the center of mass of the region, and letting it grow evenly in all directions until a non-white pixel is met.

Eventually, a path planning algorithm is used to plan the obstacle-free route that connects the current tip pose $\boldsymbol{\omega}_{start}$ to $\boldsymbol{\omega}_{goal}$. The implemented method considers a Road-Map planning strategy relying on Voronoi diagrams to sample the free-space and Dijkstra's algorithm to find the shortest path to the goal pose (considering the HJ as holonomic in its task space expressed in polar coordinates) (Figure 5.5d and e). The path planning algorithm considers the green channel of the map as a free-space, while obstacles and unexplored regions are considered as restricted areas during the sampling an planning process. The Voronoi diagram based sampling approach allows generation of paths that generally maximize the distance from the obstacles. In this way, when compared with Rapidly-

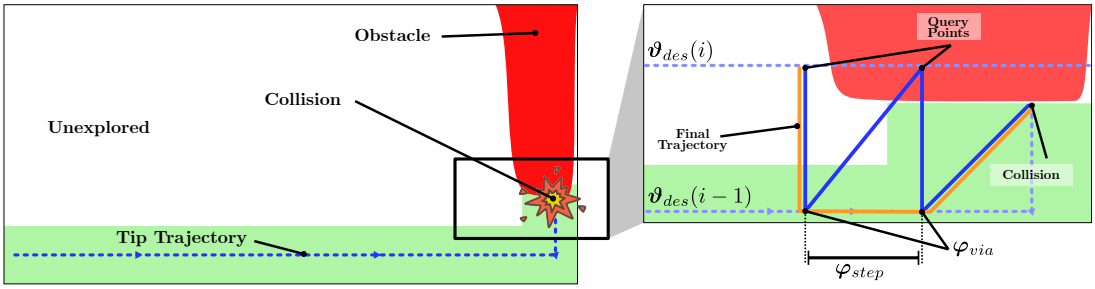

Figure 5.6: Detailed view of the main steps of P2. When a collision is experienced while moving along ϑ, the map is queried searching for a passage around the obstacle.

Exploring Random Trees (RRT) approaches or Probabilistic Road Map (PRM), Voronoi sampling represents a more reliable solution when a path through a narrow passage is required.

Two main safety measures were adopted to ensure a collision free transition from $\boldsymbol{\omega}_{start}$ to $\boldsymbol{\omega}_{goal}$. The obstacles were expanded by a constant value (e.g. 5 pixels) inside the free-space, in this way taking into account the dimensions of the tip and guaranteeing a minimum safety distance from the generated path (Figure 5.5c). Moreover, to avoid path samples in the region where ϑ_{des} would cause the singularity of φ_{obs} (see Section 4.2.2), the safety region in between $\vartheta = 0$ and $\vartheta = 10$ deg was marked as restricted.

The result of the path planning algorithm is fed to the position controller as a series of via points. Once the tip reaches $\boldsymbol{\omega}_{goal}$, the normal zig-zag motion resumes.

When the tip moves from a current elevation to the successive ϑ_{des}, a collision with an unknown obstacle can occur. The reaction steps of P1 might not be enough to escape the collision state. P2 approaches this problem by analysing the map in the attempt to find a passage on the left or right of the obstacle (Figure 5.6). This is accomplished by iteratively querying the map at $\boldsymbol{\omega}_{des} = [\varphi_{des} + \varphi_{step},\ \vartheta_{des}]^T$, until an obstacle-free pose is found. If this happens, the tip is moved to the previous elevation level, then translated along the set of φ_{via} generated during the iterations, and finally driven to ϑ_{des}. Here, the normal zig-zag motion resumes. If the method fails in finding a safe passage, the tip is considered trapped in between two obstacles. In this situation the coverage percentage is evaluated and the procedure terminated.

5.3 Evaluation

5.3.1 Obstacle Detection

To estimate the values for the thresholds τ_1 and τ_2 and test the robustness of the obstacle detection algorithm, a series of calibration and validation tests were performed. An experimental set-up was assembled for these tests as shown in Figure 5.7. It consisted of the standard set-up described Figure 2.8, with the addition of a series of obstacles. The color-coded obstacles were designed to stop the HJ's tip along the main directions of motion: φ (blue obstacles) and ϑ (red obstacles). The obstacles were comprised of medium-density fibreboard panels mounted on an aluminium profile. This configuration allowed adjustment of the relative position between the red obstacles and the endoscope. The blue obstacles could also be repositioned thanks to a 3D printed attachment, reversibly fixing them to the main structure.

During a first calibration stage, the HJ was steered in its workspace by independently actuating a single jet at a time, starting from the HJ resting pose. The set of obstacles was reduced to include the red obstacles only, obstructing the movements along the ϑ direction. When the tip of the endoscope hit the obstacle, the collision was manually recorded using a custom Graphical User Interface (GUI) and by visually inspecting the scene. Each test, consisting of 10 collisions, was repeated once for each jet, in this way obtaining a total of 30 collisions. The resulting data were used to tune the thresholds τ_1 and τ_2 in the attempt to maximize the sensitivity of the algorithm, defined as the ratio between the the number of True Positive (TP) detections and the actual number of collisions (TP plus False Negatives (FN)). At the same time, the number of False Positives (FP) was taken into account and minimized with a appropriate choice of τ_1 and τ_2. The resulting thresholds guaranteed a sensitivity of 93.3% with only one FP detected.

To validate the calibration output, new data registered during 60 collisions was analysed by the obstacle detection algorithm. Half of collisions were recorded during a tip movement along the ϑ direction, as described for the calibration test. The remaining 30 collisions were registered while the HJ was moving along the φ coordinate. In this case, a series of 10 collisions were generated with the HJ's tip initially positioned at $\varphi_{test} = [0,\ 120,\ 240]$ deg and with two obstacles located at $\varphi_{test} \pm 20$ deg. From its initial position, the tip was steered towards the obstacles and the collision recorded using the GUI.

By using the previous estimated values for τ_1 and τ_2, the resulting sensitivity

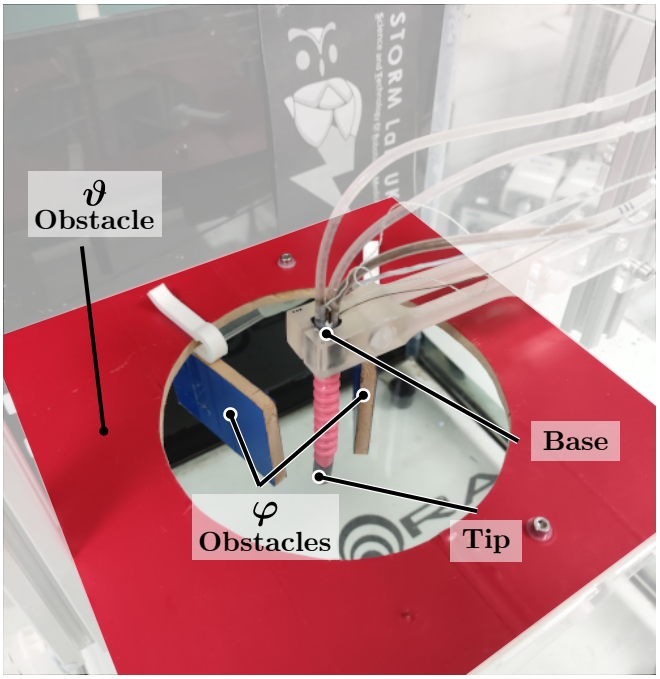

Figure 5.7: Experimental set-up for the calibration of τ_1 and τ_2 and the validation of the obstacle detection algorithm.

of the obstacle detection algorithm was 90.0%, with a total of 3 FP detected.

An example of the signals used to detect the collision is shown in Figure 5.8a and b, where the three detection stages are highlighted. When ξ_1 exceeded τ_1, the inspection period started (yellow shaded area). This caused the zeroing of ξ_2 (the blue dashed line refers to the original, non-zeroed ξ_2) and the monitoring of its evolution in time. In this example, ξ_2 exceeded τ_2 before the end of the inspection period, thus triggering the confirmation of the collision. The collision state (red shaded area) persisted until ξ_2 fell below τ_2, in this way returning to a safe status.

To asses the responsiveness of the detection strategy, the elapsed time between the visual recognition of the collision (registered by user input to the GUI) and the acknowledgement produced by the algorithm was evaluated. The results in Figure 5.8 show how the time to detect the collision is not influenced by the type of movement the HJ is performing. The mean and standard deviation values are 0.66 $\pm$0.33 s and 0.61 $\pm$0.84 s for movements along ϑ and φ respectively. The overall mean and standard deviation values are 0.64 $\pm$0.56 s.

5.3.2 Autonomous Exploration

By relying on the closed-loop control strategy described in Chapter 4 and the obstacle detection algorithm introduced in Section 5.2.1, a comprehensive test

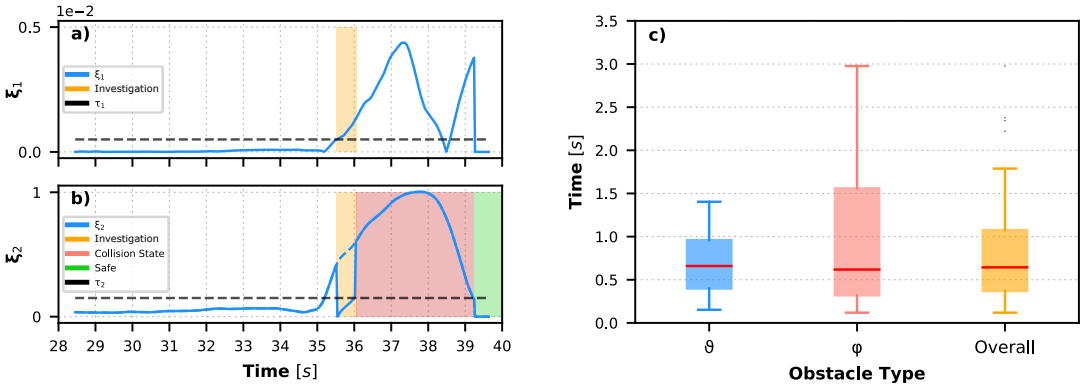

Figure 5.8: Experimental results for the validation of the obstacle detection algorithm. In a) and b) an example of obstacle detection is presented, highlighting the three phases of the detection: investigation (yellow), collision (red) and safety (green). In c) the time required for confirmation of the collision is presented for movements along ϑ (blue) and φ (red). In yellow the overall responsiveness of the algorithm is presented.

was designed to asses the ability of the autonomous navigation algorithm (mapping and path planning) to explore the environment. The test was executed in a simulated environment based on Gazebo (Open Source Robotics Foundation, v7). The HJ soft bending section was modelled using a series of 20 rigid links, interconnected using torsional springs with known stiffness. Two identical models of the endoscope are spawned, however, only in one of these models the possibility of collision is enabled. In other words, when the HJ collides with an obstacle, the collision-enabled model M_t will stop, while the second model M_g will penetrate the obstacle. In this way the real-world scenario was replicated, with M_t simulating the physical HJ, while M_g replicated the response of the kinematic model. The obstacle detection, mapping and planning algorithms were designed using python nodes in a Robot Operating System (ROS, Kinetic Kame) environment and were executed on an Intel Xeon powered machine (CPU E5-1660 v4, 3.2GHz). The simulation real-time factor was in the range 0.93 to 0.95 for the entire duration of the trials.

Artificial obstacles were introduced in the scene. The obstacles, created using Blender (The Blender Foundation, v2.79b), were designed to limit the movement of the HJ along its main trajectory. An obstacle-free region around the HJ resting position was considered to ensure that the tip was able to escape the singularity region of the workspace at the beginning of the test.

In a first test, the ϑ_{des} range of variation was limited to 120 deg, to meet the bending requirements defined in Chapter 2. Tests considering a maximum value of ϑ_{des} of 90 deg were also performed to reproduce the control results shown in Chapter 4. The results from one simulation example are shown in Figure 5.9.

The 3D representation of the environment in Figure 5.9a shows how the the

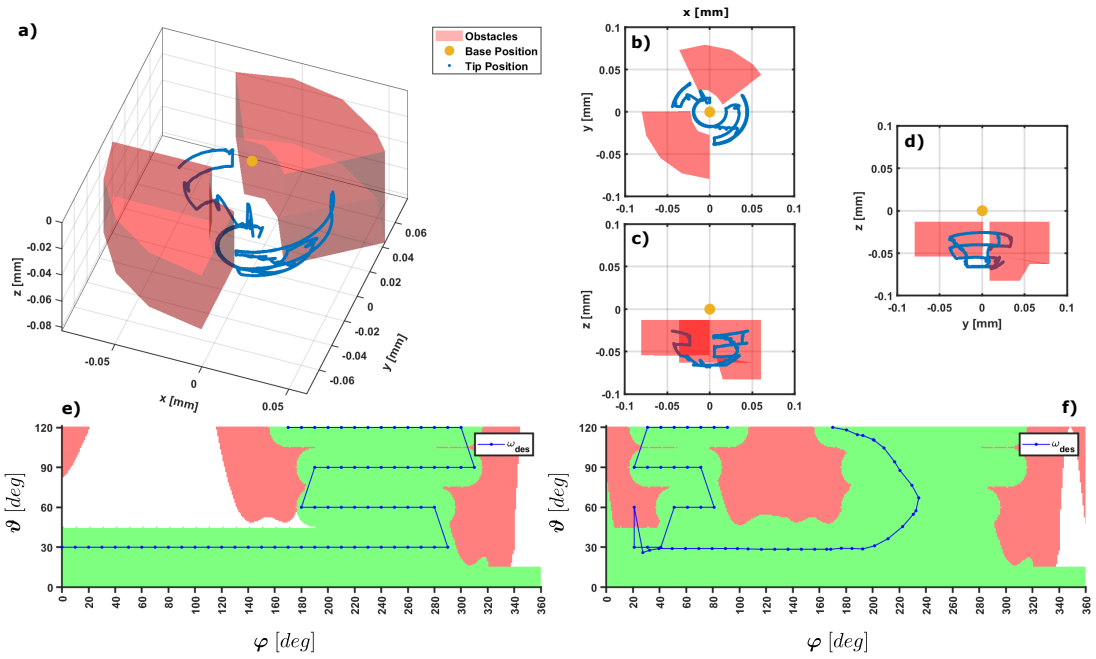

Figure 5.9: Simulation results showing a) the shape of the obstacles (red) and the trajectory followed by the tip (blue). In b), c) and d) 3 orthogonal projections of the simulated scene are shown. In e) and f) the map of the environment before and after the re-planning is presented respectively (green regions represent the explored and obstacle free areas, while the red regions refer to the detected obstacles).

first set of obstacles divides the workspace into four areas, in this way precluding the exploration of half of the workspace along the φ coordinate. The geometry of the obstacle is also visible from three orthogonal projections showing the top, front and side view of the scene (Figure 5.9b, c and d respectively). The HJ was successful in exploring the entire free-space as shown by the trajectory followed by the tip. In in Figure 5.9b, the difference between the plain zig-zag motion and the trajectory generated by the path planner is visible. The same trajectory is visible in in Figure 5.9e and f. In in Figure 5.9e the tip reached the maximum allowed elevation (120 deg) and could not proceed to the next level. The path planning output, triggered in such a scenario, is shown in in Figure 5.9f. Here, the HJ moved from its current position toward the goal, following the planned trajectory. When the tip tried to enter the unexplored region, a collision was experienced and triggered the map querying process. A passage around the obstacle was successfully found, allowing the tip to continue the exploration. Despite 95% coverage being achieved, the presence of the safety strip at the lower edge of the map and the symmetry of the map, not considered for the tests, created an unreachable region at the right end of the map, which remained unexplored.

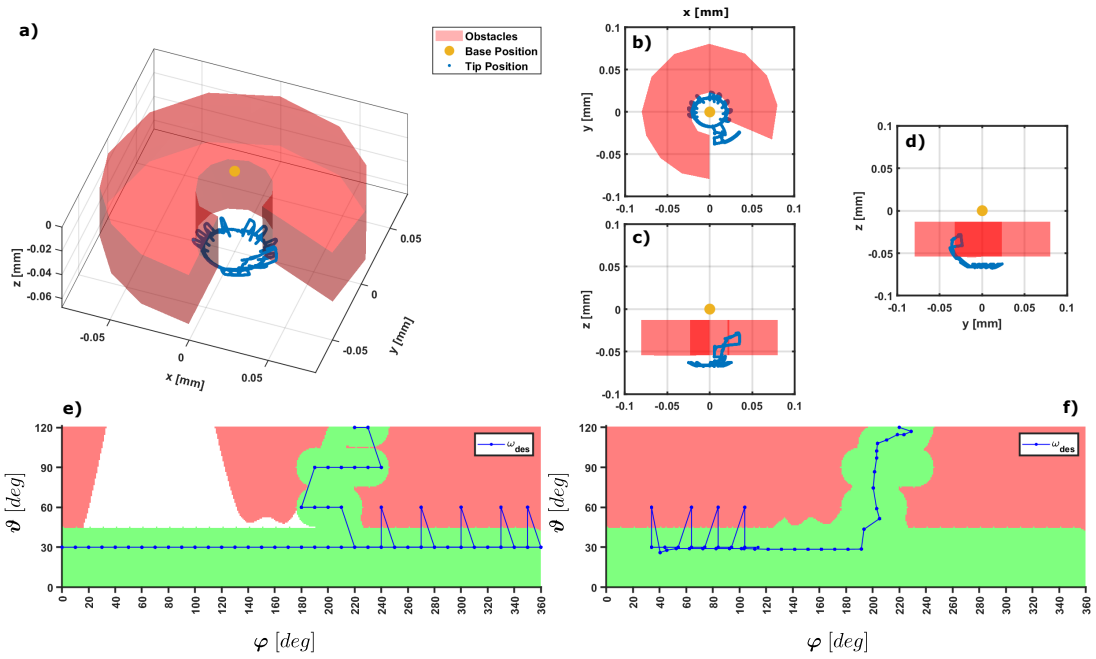

Figure 5.10: Simulation using a different set of obstacles represented in a) by the red 3D model together with the trajectory followed by the tip in blue. In b), c) and d) 3 orthogonal projections of the simulated scene are shown. In e) and f) the map of the environment before and after the re-planning is presented respectively (green regions represent the explored and obstacle free areas, while the red regions refer to the detected obstacles).

A more challenging scenario is offered by a second set of obstacles. The movements of the HJ's tip are constrained by a C-shaped obstacle that only allows the exploration of narrow portion of the environment. Success in exploring this region relies on the ability to find a collision free passage around the obstacle. As visible in Figure 5.9e, this is accomplished by trying to reach the desired point first, and searching for a path around the obstacle if a collision is detected. Given the shape of the obstacles, the tip explored multiple times (9 in total) the possibility of reaching the desired elevation within a single step.

Results from tests characterized by a maximum value of ϑ_{des} of 90 deg where comparable to the those shown in Figures 5.9 and 5.10. The planning time and overall duration of the test represent the only noticeable differences. A median time to plan the trajectory of 6.88 $\pm$0.25 s and 8.89 $\pm$0.54 s was recorded for ϑ_{max} values of 90 and 120 deg respectively, while the median time to complete the test was 348.6 $\pm$40 s and 533.4 $\pm$132.2 s, over a total of 16 repetitions.

To compare the shape of the trajectory generated by the Voronoi based path planning strategy, three significant images were selected and supplied to a RRT and a PRM planners. The images include a short narrow passage, a long narrow passage and a large free-space area (Figure 5.11a b and c respectively). The resulting paths are shown in Figure 5.11. The images confirm that the Voronoi

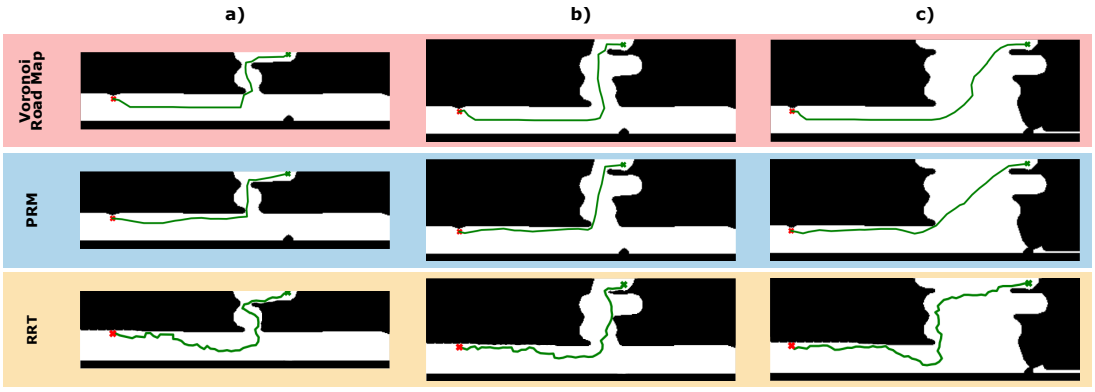

Figure 5.11: Comparison of path planning algorithms on examples of maps obtained from the simulated exploration of the environment. Voronoi Road Map, Probabilistic Road Map and Rapidly-Growing Random Tree are used on examples of a) a short narrow passage, b) a long narrow passage and c) a large free-space area.

based planner represents the most suitable choice when a safe distance from the obstacles and a smooth trajectory are needed. On the other hand, the PRM produces paths that are too close to the obstacles, while the RRT generates trajectories characterized by unnecessary and sudden changes of direction, resulting in longer path to reach the goal pose.

5.4 Discussion

The results presented in this chapter indicate the feasibility of an autonomous strategy for the exploration of an unknown environment using the HJ. An obstacle detection algorithm based on comparison between a kinematic model and sensor feedback has been presented. The detection of the collision event relies on estimated and measured poses of the tip to evaluate the status of the endoscope. A sensitivity of 93.3% and 90.0% was assessed during a calibration and validation process respectively, with the algorithm misinterpreting the data (FP and FN) in 12 cases over 90 collisions events. With respect to previous works on the HJ platform [139], the obstacle detection algorithm presented an exceptional responsiveness, with the time required to recognize the collision event below 1 s (0.64 $\pm$0.56 s). Consequently, a faster exploration and a lower water consumption are achievable.

Mapping and path planning methods have also been presented. The collision-mapping strategy employs a continuously varying curve to describe the position and volume of the obstacles, while the path planning method safely reacts to the collisions by implementing two reaction policies. By relying on the closed-loop control scheme described in Chapter 4, and the obstacle detection, environment

mapping and motion planning described in this chapter, the HJ was used to autonomously explore two scenes characterized by different sets of obstacles. In all tests the proposed approach successfully reacted to collisions, guided the endoscope along the re-planned trajectory and achieved a coverage value of more than 95%, thus confirming the effectiveness of the approach. This is important for reducing the required skill level of the user who is only asked to initialize the inspection or re-start a procedure halted by incorrect detections of collisions.

5.5 Conclusions

In this chapter a method for enabling autonomous behaviours of the HJ endoscopic platform has been presented. The method is based on the ability of the endoscope to detect a collision with an obstacle, build a map of the surroundings while exploring the unknown environment and autonomously re-planning the inspection trajectory to maximize the percentage of visualized areas.

A method for detecting the collisions with obstacles has been described and tested, resulting in a responsive approach that allows the duration of the task and thus the amount of water used during the test to be reduced.

The autonomous exploration procedure, demonstrated in a simulated environment, showed how the implemented approach was able to manoeuvre the HJ while building a map of the surroundings. The proposed approach was effective in safely reacting to collisions and planning the desired trajectory accordingly to explore unknown areas of the environment.

Chapter 6

Conclusions and Future Directions

The feasibility of a water-jet powered endoscope for the inspection of the gastric cavity was demonstrated in [17] and [16]. The resulting endoscopic platform, the HJ, exhibited promising performance from both a technical and economic point of view. The simplicity of its construction potentially allows the high costs related to standard FE to be overcome. To this end, the ability to fabricate the endoscope at a minimal production cost enables the use of the HJ as a single-use device, in this way eliminating all costs related to maintenance and reprocessing of the endoscope.

Despite the encouraging capabilities demonstrated by early HJ prototypes, a number of crucial limitations were identified. First, the manoeuvrability of the endoscope was highly limited by the confined range of motion of the tip. A solution to this problem was proposed and consisted of using the combination of water-jet actuation and a pivoting action off of the stomach wall to achieve the retroflexion of the tip, thus allowing visualization of all gastric landmarks. This represents a valid approach, however, it requires substantial mental effort and user skill; inevitably causing a protraction of the procedure.

Secondly, the actuation system, relying on dry pinch valves to modulate the flow-rate of the water ejected from the nozzles, caused damage of the soft tubing. This in turn resulted in a high probability of rupture of the tube and a modified input-output characteristic of the actuator during operation.

The technical solutions proposed by this thesis represent feasible improvements that allow the aforementioned limitations to be overcome and introduce advanced capabilities aimed at facilitating the employment of the HJ platform in real-world scenarios.

In Chapter 2, a HJ design characterized by a non-homogeneous stiffness of the tether has been presented. Introducing a lower stiffness section into the distal

part of the endoscope allowed for a wider range of motion of the tip; although, it also introduces unstable behaviours at wide bending angles. The kinking event of thin-walled tubing carrying pressurized water to the tip of the endoscope was identified as the principal cause of the instability. The use of a stiffer constituent material for the soft bending section was explored and the newly developed HJ was extensively tested. Results from the experimental validation showed how the the proposed design helped in achieving the minimum bending requirements on 120 deg while guaranteeing the stability of the tip. The HJ was equipped with an improved camera module that, combined with the enhanced range of motion, enabled a range of view of 180 deg. The adoption of a stiffer bending section allowed minimization of the number of pneumatic/hydraulic components while maintaining the suction and isufflation capabilities of the system.

A inhomogeneous bending behaviour was also observed. This can be caused by a variety of factors such as inaccuracies in the fabrication of the propulsion module (variable nozzle geometry), non-straight paths of the hydraulic channels or the non-homogeneous properties of the soft sleeve. In fact, the curing (combination of heat and UV radiation) process, required by the mould fabrication procedure, can cause a visible warping that results in a non constant thickness of the moulded soft sleeve.

To address this issue, alternative fabrication methods could be explored to produce the soft sleeve (e.g. blow moulding). In addition, a variety of soft sleeve constituent materials could be explored to identify the optimal compound that produces wide bending angles while guaranteeing the stability of the tip.

To address the problem caused by the pinching action of the flow-rate control system, a novel valve design called the ECV has been proposed in Chapter 3. The combination of a wider compression area and a moving contact point guaranteed a stable input-output characteristic of the valve, when compared with the standard approach based on pinch valves. Tests performed with a variety of tube durometers allowed the tube material that would ensure the ideal performance of the valve to be identified.

A specific optimization strategy has also been introduced to deliver a linear input-output characteristic and improved actuator resolution. Comprehensive tests on the HJ endoscope demonstrated how the optimized ECV was able to reduce variation of the flow-rate, resulting in smoother movements of the endoscope's tip when compared to the action of both pinch valves and wet solenoid valves.

Additional factors could be taken into account when performing the optimization of the custom compression profile. Flow-rate regime (laminar or turbulent),

precision of the fabrication process, tubing alignment could be considered to further improve the device efficiency.

In Chapter 4, a model-free closed-loop control strategy in a polar coordinate system has been presented. The approach only relies on sensor feedback to deliver reliable control of the endoscope tip along a user defined trajectory. Although the control scheme does not require inversion of a kinematic model, a compensation of the hysteresis, produced by the actuators (ECV), was needed to reach particular configurations in the workspace. Considering the stable and linear input-output characteristic of the ECV, the hysteretic behaviour of the valve was modelled using two linear curves. The resulting hysteresis-compensated controller was able to steadily drive the HJ't tip along a predefined path.

The tip elevation restricted to 90 deg during the zig-zag motion represents the main limitation of the proposed method, and it is caused by the arrangement (or re-arrangement) of the tubing inside the soft bending segment. An alternative to the zig-zag path could be explored for elevations above the critical value where the tube re-arrangement occurs, so that the displacement along the φ direction is performed at lower elevations, while the exploration of the remaining part of the workspace is achieved with pure movements along ϑ.

Implementation of a velocity control scheme represents a potential future solution that could minimize the time required to complete the task, while testing the HJ in submerged conditions could help to reduce the amplitude of the tip oscillations.

The third DoF (elongation of the bending section) could also be introduced into the design of the system and integrated in the proposed control scheme by considering the term r of the polar coordinate system as variable. The elongation of the bending segment could help in reaching the distal part of the stomach without the need for the user to adjust the insertion of the tether; further supporting procedural automation.

The implementation of autonomous or semi-autonomous behaviours has been explored in the attempt to relieve physicians of the burden of repetitive tasks. This is particularly true in the case of MIS but, it can be also translated into the field of robotic endoscopy with the promise for reduced time to complete a procedure, as well as a lower mental demand from a user point of view.

In the specific case of endoscopy for gastric cancer screening, task automation has the potential to facilitate the implementation of mass screening programmes for gastric cancer in countries where the risk of stomach cancer is high. In fact, such population based screening campaigns generally require an enormous economic and logistic effort in the attempt to reach the entire pool of eligible

patients. These limitations often result in a limited diffusion of the screening action that consequently causes poor mortality reduction.

With the endoscopic platform described in Chapter 2 defining a low-cost alternative to standard FE, the introduction of autonomous capabilities could help in spreading the action of the programs to areas that are generally poorly served by the national health systems.

The autonomous strategy for the inspection of the gastric cavity, presented in Chapter 5, represents an example of how autonomous behaviours could help in performing gastroscopy procedures with no or minimal intervention of the user. The motivation of this approach lies in the need for non-expert personnel to be involved in the screening process, so that more procedures can be performed in parallel.

The combination of collision detection, mapping of the environment and trajectory re-planning methods have been proven to be effective in optimizing the output of the inspection process, so that the accessible environment can be completely explored and visualized.

Despite the positive results confirming the performance of the suggested approach, some limitations remain and need to be properly addressed to effectively translate the use of the HJ into clinical use. An example is represented by the reliability of the obstacle detection algorithm. In spite of the high sensitivity of the method, the probability of occurrence of FP or FN remains significant and requires the intervention of the user to interpret specific situations and allow the HJ to continue the inspection autonomously.

In a simulated environment, the collision detection method never failed at identifying a collision, thus guaranteeing the continuation of the exploration task without the need for cooperation of the user. Further studies are required to identify how the autonomous exploration would act in laboratory settings or in real-case scenarios, and determine the consequences of undesired FP and FN.

The translation into clinical use would also require adapting the HJ sensory equipment to meet the low-cost and portability requirements. Alternative to the EM probes, used to perform the experimental validation in this thesis, exist and one example is represented by the IMU; one is already integrated into the base of the endoscope. An additional IMU was used in [144] to measure the orientation of the HJ's tip and account for modelling inaccuracies. Despite being a reliable and well-established method to estimate the orientation of a body, the use of an IMU at the tip of the endoscope implies bigger capsule dimensions and increased assembly costs (e.g. additional wiring).

On the other hand, the image sensor at the tip of the endoscope could, at the

same time, allow the visualization of the stomach mucosa and reconstruct the 3D pose of the endoscope by relying on visual odometry methods [130, 131, 140, 145]. When an image from a monocular camera is used, the estimated pose is without meaningful scale. To obtain physically meaningful data and enable closed-loop control strategies, the scale factor needs to be estimated. This can be achieved using known 3D features of the environment(e.g. markers, known sized objects), information coming from additional sensors located at the tip of the endoscope (e.g. IMU, EM probes), registration on medical imaging or, using a relatively accurate kinematic model of the robot. The latter is already available for the HJ soft bending section, in this way enabling the estimation of the scale factor and the initialization of the camera pose without the need for additional hardware.

The calibration object presented in Chapter 4 offers the possibility to calibrate intrinsic and extrinsic camera parameters as part of the HJ standard sensor calibration procedure. Thus, the relative positioning of the camera and propulsion system can be easily estimated. To further improve the performance, the use automatic lesions and landmarks detection methods could be integrated in the automation strategy and guide the HJ towards suspicious regions that require further inspection.

In summary, the work presented in this thesis is motivated by the need for a low-cost yet practical and reliable solution to realize population based gastric cancer screening programs in countries characterized by high incidence of this disease. The design and control improvements, together with the introduction of autonomy, optimized and augmented the capabilities of the low-cost endoscope, in this way bringing the HJ a step closer to its clinical use.

References

[1] J. Ferlay, M. Colombet, I. Soerjomataram, C. Mathers, D. M. Parkin, M. Piñeros, A. Znaor, and F. Bray, "Estimating the global cancer incidence and mortality in 2018: GLOBOCAN sources and methods," *International journal of cancer*, vol. 144, no. 8, pp. 1941–1953, 2019. viii, 10, 11

[2] P. Valdastri, R. J. Webster III, C. Quaglia, M. Quirini, A. Menciassi, and P. Dario, "A new mechanism for mesoscale legged locomotion in compliant tubular environments," *IEEE Transactions on Robotics*, vol. 25, no. 5, pp. 1047–1057, 2009. viii, 23, 26

[3] I. De Falco, G. Tortora, P. Dario, and A. Menciassi, "An integrated system for wireless capsule endoscopy in a liquid-distended stomach," *IEEE transactions on biomedical engineering*, vol. 61, no. 3, pp. 794–804, 2014. viii, 23, 26

[4] D. Son, M. D. Dogan, and M. Sitti, "Magnetically actuated soft capsule endoscope for fine-needle aspiration biopsy," in *Robotics and Automation (ICRA), 2017 IEEE International Conference on*, pp. 1132–1139, IEEE. viii, 24, 25, 26

[5] H. Keller, A. Juloski, H. Kawano, M. Bechtold, A. Kimura, H. Takizawa, and R. Kuth, "Method for navigation and control of a magnetically guided capsule endoscope in the human stomach," in *Biomedical Robotics and Biomechatronics (BioRob), 2012 4th IEEE RAS & EMBS International Conference on*, pp. 859–865, IEEE. viii, 24, 26, 35

[6] G. Kósa, P. Jakab, G. Székely, and N. Hata, "MRI driven magnetic microswimmers," *Biomedical microdevices*, vol. 14, no. 1, pp. 165–178, 2012. viii, 24, 26

[7] E. Ayvali, C.-P. Liang, M. Ho, Y. Chen, and J. P. Desai, "Towards a discretely actuated steerable cannula for diagnostic and therapeutic pro-

cedures," *The International journal of robotics research*, vol. 31, no. 5, pp. 588–603, 2012. ix, 27

[8] I. I. I. Robert J. Webster, J. S. Kim, N. J. Cowan, G. S. Chirikjian, and A. M. Okamura, "Nonholonomic Modeling of Needle Steering," *The International Journal of Robotics Research*, vol. 25, no. 5-6, pp. 509–525, 2006. ix, 27

[9] R. J. Webster, A. M. Okamura, and N. J. Cowan, "Toward Active Cannulas: Miniature Snake-Like Surgical Robots," pp. 2857–2863, 2006. ix, 27, 28

[10] D. R. Berg, P. Y. Li, and A. G. Erdman, "Achieving dexterous manipulation for minimally invasive surgical robots through the use of hydraulics," *ASME Paper No. DSCC2012-MOVIC2012-8685*, 2012. ix, 27, 28

[11] K. Ikuta, H. Ichikawa, K. Suzuki, and D. Yajima, "Multi-degree of freedom hydraulic pressure driven safety active catheter," in *Robotics and Automation, 2006. ICRA 2006. Proceedings 2006 IEEE International Conference on*, pp. 4161–4166, IEEE. ix, 27, 28

[12] J. H. Chandler, M. Chauhan, N. Garbin, K. L. Obstein, and P. Valdastri, "Parallel Helix Actuators for Soft Robotic Applications.," *Frontiers in robotics and AI*, vol. 7, p. 119, 2020. ix, 27, 29

[13] G. Pittiglio, L. Barducci, J. W. Martin, J. C. Norton, C. A. Avizzano, K. L. Obstein, and P. Valdastri, "Magnetic Levitation for Soft-Tethered Capsule Colonoscopy Actuated With a Single Permanent Magnet: A Dynamic Control Approach HHS Public Access," *IEEE Robot Autom Lett*, vol. 4, no. 2, pp. 1224–1231, 2019. ix, 27, 29

[14] Y. Kim, G. A. Parada, S. Liu, and X. Zhao, "Ferromagnetic soft continuum robots," vol. 4, p. 7329, 2019. ix, 27, 29

[15] S. Jeon, A. K. Hoshiar, K. Kim, S. Lee, E. Kim, S. Lee, J. Y. Kim, B. J. Nelson, H. J. Cha, B. J. Yi, and H. Choi, "A Magnetically Controlled Soft Microrobot Steering a Guidewire in a Three-Dimensional Phantom Vascular Network," *Soft Robotics*, vol. 6, pp. 54–68, feb 2019. ix, 27

[16] F. Campisano, F. Gramuglia, I. R. Dawson, C. T. Lyne, M. L. Izmaylov, S. Misra, E. D. Momi, D. R. Morgan, K. L. Obstein, and P. Valdastri, "Gastric cancer screening in low-income countries: System design, fabrication, and analysis for an ultralow-cost endoscopy procedure," *IEEE Robotics*

Automation Magazine, vol. 24, pp. 73–81, June 2017. ix, 3, 35, 36, 38, 40, 53, 68, 112

[17] R. Caprara, K. L. Obstein, G. Scozzarro, C. Di Natali, M. Beccani, D. R. Morgan, and P. Valdastri, "A platform for gastric cancer screening in low- and middle-income countries.," *IEEE Transactions on Biomedical Engineering*, vol. 62, no. 5, pp. 1324–1332, 2015. ix, 3, 33, 36, 37, 38, 40, 112

[18] F. Campisano, S. Calò, A. A. Remirez, J. H. Chandler, K. L. Obstein, and P. Valdastri, "Closed-loop control of soft continuum manipulators under tip follower actuation," *International Journal of Robotics Research*, 2019. ix, 40, 44, 75, 92, 95

[19] World Health Organization, "Cancer Key Facts," 2018. xvi, 10

[20] J. Ferlay, I. Soerjomataram, R. Dikshit, S. Eser, C. Mathers, M. Rebelo, D. M. Parkin, D. Forman, and F. Bray, "Cancer incidence and mortality worldwide: sources, methods and major patterns in GLOBOCAN 2012," *International journal of cancer*, vol. 136, no. 5, 2015. xvi, 10, 12

[21] W. H. Organization, "Globocan project." 12

[22] A. Giuseppe, *Human Anatomy*. 2014. 13

[23] P. Lauren, "The two histological main types of gastric carcinoma: diffuse and so-called intestinal-type carcinoma. an attempt at a histo-clinical classification," *Acta pathol microbiol scand*, vol. 64, pp. 31–49, 1965. 13

[24] L. P. Carcas, "Gastric cancer review," *Journal of carcinogenesis*, vol. 13, 2014. 14

[25] P. Correa, "Gastric cancer: overview," *Gastroenterology Clinics of North America*, vol. 42, no. 2, p. 211, 2013. 14

[26] R. Miyahara, Y. Niwa, T. Matsuura, O. Maeda, T. Ando, N. Ohmiya, A. Itoh, Y. Hirooka, and H. Goto, "Prevalence and prognosis of gastric cancer detected by screening in a large Japanese population: data from a single institute over 30 years," *Journal of gastroenterology and hepatology*, vol. 22, no. 9, pp. 1435–1442, 2007. 14

[27] L. Yang, "Incidence and mortality of gastric cancer in China," *World journal of gastroenterology: WJG*, vol. 12, no. 1, p. 17, 2006. 14

[28] M. Plummer, C. de Martel, J. Vignat, J. Ferlay, F. Bray, and S. Franceschi, "Global burden of cancers attributable to infections in 2012: a synthetic analysis," *The Lancet Global Health*, vol. 4, no. 9, pp. e609–e616, 2016. 14

[29] W. K. Leung, M.-s. Wu, Y. Kakugawa, J. J. Kim, K.-g. Yeoh, K. L. Goh, K.-c. Wu, D.-c. Wu, J. Sollano, and U. Kachintorn, "Screening for gastric cancer in Asia: current evidence and practice," *The lancet oncology*, vol. 9, no. 3, pp. 279–287, 2008. 14, 17, 18

[30] G. H. Kim, P. S. Liang, S. J. Bang, and J. H. Hwang, "Screening and surveillance for gastric cancer in the United States: Is it needed?," *Gastrointestinal endoscopy*, vol. 84, no. 1, pp. 18–28, 2016. 15, 16, 17

[31] K. Sugano, "Screening of gastric cancer in asia," *Best Practice and Research Clinical Gastroenterology*, vol. 29, no. 6, pp. 895–905, 2015. 15, 16, 18

[32] C. Hamashima, "Current issues and future perspectives of gastric cancer screening," *World Journal of Gastroenterology: WJG*, vol. 20, no. 38, p. 13767, 2014. 16

[33] O. Hosokawa, T. Miyanaga, Y. Kaizaki, M. Hattori, K. Dohden, K. Ohta, Y. Itou, and H. Aoyagi, "Decreased death from gastric cancer by endoscopic screening: Association with a population-based cancer registry," *Scandinavian Journal of Gastroenterology*, vol. 43, no. 9, pp. 1112–1115, 2008. 16

[34] C. Hamashima, K. Ogoshi, M. Okamoto, M. Shabana, T. Kishimoto, and A. Fukao, "A Community-Based, Case-Control Study Evaluating Mortality Reduction from Gastric Cancer by Endoscopic Screening in Japan," *PLOS ONE*, vol. 8, no. 11, p. e79088, 2013. 16, 18

[35] C. Hamashima, M. Okamoto, M. Shabana, Y. Osaki, and T. Kishimoto, "Sensitivity of endoscopic screening for gastric cancer by the incidence method," *International journal of cancer*, vol. 133, no. 3, pp. 653–659, 2013. 16

[36] H. O. Adami, N. E. Day, D. Trichopoulos, and W. C. Willett, "Primary and secondary prevention in the reduction of cancer morbidity and mortality," *European Journal of Cancer*, vol. 37, no. Supplement 8, pp. 118–127, 2001. 16

[37] I. H. p. W. Group, "Helicobacter pylori eradication as a strategy for preventing gastric cancer," report, International Agency for Research on Cancer (IARC Working Group Reports, No. 8), 2014. 16

[38] Y. Yuan, "A survey and evaluation of population-based screening for gastric cancer," *Cancer biology and medicine*, vol. 10, no. 2, p. 72, 2013. 17, 18

[39] M. Areia, M. C. W. Spaander, E. J. Kuipers, and M. Dinis-Ribeiro, "Endoscopic screening for gastric cancer: A cost-utility analysis for countries with an intermediate gastric cancer risk," *United European Gastroenterology Journal*, vol. 0, no. 0, p. 2050640617722902. 17

[40] T. Mizoue, T. Yoshimura, N. Tokui, Y. Hoshiyama, H. Yatsuya, K. Sakata, T. Kondo, S. Kikuchi, H. Toyoshima, and N. Hayakawa, "Prospective study of screening for stomach cancer in japan," *International journal of cancer*, vol. 106, no. 1, pp. 103–107, 2003. 17

[41] C. Hamashima, D. Shibuya, H. Yamazaki, K. Inoue, A. Fukao, H. Saito, and T. Sobue, "The japanese guidelines for gastric cancer screening," *Japanese Journal of Clinical Oncology*, vol. 38, no. 4, pp. 259–267, 2008. 10.1093/jjco/hyn017. 18

[42] Y. Kim, J. K. Jun, K. S. Choi, H.-Y. Lee, and E.-C. Park, "Overview of the National Cancer screening programme and the cancer screening status in Korea," *Asian Pac J Cancer Prev*, vol. 12, no. 3, pp. 725–730, 2011. 18

[43] J. H. Lee, J. G. Kim, H.-K. Jung, J. H. Kim, W. K. Jeong, T. J. Jeon, J. M. Kim, Y. I. Kim, K. W. Ryu, S.-H. Kong, H.-I. Kim, H.-Y. Jung, Y. S. Kim, D. Y. Zang, J. Y. Cho, J. O. Park, D. H. Lim, E. S. Jung, H. S. Ahn, and H. J. Kim, "Clinical Practice Guidelines for Gastric Cancer in Korea: An Evidence-Based Approach," *Journal of Gastric Cancer*, vol. 14, no. 2, pp. 87–104, 2014. 18

[44] A. Rollan, R. Giancaspero, F. Fuster, C. Acevedo, C. Figueroa, K. Hola, M. Schulz, and I. Duarte, "The long-term reinfection rate and the course of duodenal ulcer disease after eradication of Helicobacter pylori in a developing country," *The American journal of gastroenterology*, vol. 95, no. 1, p. 50, 2000. 18

[45] C. Hamashima and R. Goto, "Potential capacity of endoscopic screening for gastric cancer in Japan," *Cancer science*, vol. 108, no. 1, pp. 101–107, 2017. 18

[46] S. Han, A. Hsu, and W. Y. Wassef, "An update in the endoscopic management of gastric cancer," *Current opinion in gastroenterology*, vol. 32, no. 6, pp. 492–500, 2016. 19

[47] C. Pant, M. S. Olyaee, and A. Rastogi, "Advanced imaging and therapeutic endoscopy," *Techniques in Gastrointestinal Endoscopy*, 2017. 19, 20

[48] E. D. Rozeboom, R. Reilink, M. P. Schwartz, P. Fockens, and I. A. Broeders, "Evaluation of the tip-bending response in clinically used endoscopes," *Endoscopy international open*, vol. 4, no. 4, p. E466, 2016. 19

[49] S. E. Funk and N. L. Reaven, "High-level endoscope disinfection processes in emerging economies: financial impact of manual process versus automated endoscope reprocessing," *Journal of Hospital Infection*, vol. 86, no. 4, pp. 250–254, 2014. 20

[50] X. Zhang, J. Kong, P. Tang, S. Wang, Q. Hyder, G. Sun, R. Zhang, and Y. Yang, "Current status of cleaning and disinfection for gastrointestinal endoscopy in China: A survey of 122 endoscopy units," *Digestive and Liver Disease*, vol. 43, no. 4, pp. 305–308, 2011. 20

[51] W. Ren-Pei, X. Hui-Jun, Q. Ke, W. Dong, N. Xing, and L. Zhao-Shen, "Correlation between the growth of bacterial biofilm in flexible endoscopes and endoscope reprocessing methods," *American Journal of Infection Control*, vol. 42, no. 11, pp. 1203–1206, 2014. 21

[52] C. L. Ofstead, H. P. Wetzler, E. M. Doyle, C. K. Rocco, K. H. Visrodia, T. H. Baron, and P. K. Tosh, "Persistent contamination on colonoscopes and gastroscopes detected by biologic cultures and rapid indicators despite reprocessing performed in accordance with guidelines.," *American journal of infection control*, vol. 43, pp. 794–801, aug 2015. 21

[53] C. L. Ofstead, K. M. Hopkins, B. L. Buro, J. E. Eiland, and H. P. Wetzler, "Challenges in achieving effective high-level disinfection in endoscope reprocessing.," *American journal of infection control*, vol. 48, pp. 309–315, mar 2020. 21

[54] C. L. Ofstead, M. R. Quick, J. E. Eiland, and S. J. Adams, "A glimpse at the true cost of reprocessing endoscopes," *International Association of Healthcare Central Service Material Management*, 2017. 21

[55] T. da Veiga, J. H. Chandler, P. Lloyd, G. Pittiglio, N. J. Wilkinson, A. K. Hoshiar, R. A. Harris, and P. Valdastri, "Challenges of continuum robots in clinical context: a review," *Progress in Biomedical Engineering*, vol. 2, p. 32003, aug 2020. 22, 27, 43, 75

[56] A. Attanasio, B. Scaglioni, E. De Momi, P. Fiorini, and P. Valdastri, "Autonomy in Surgical Robotics," *Annual Review of Control, Robotics, and Autonomous Systems*, vol. 4, no. 1, p. null, 2021. 22

[57] P. Valdastri, M. Simi, and R. J. Webster III, "Advanced technologies for gastrointestinal endoscopy," *Annual review of biomedical engineering*, vol. 14, pp. 397–429, 2012. 23

[58] A.-M. Singeap, C. Stanciu, and A. Trifan, "Capsule endoscopy: The road ahead," *World journal of gastroenterology*, vol. 22, no. 1, p. 369, 2016. 23

[59] C. Stefanini, A. Menciassi, and P. Dario, "Modeling and experiments on a legged microrobot locomoting in a tubular, compliant and slippery environment," *The International Journal of Robotics Research*, vol. 25, no. 5-6, pp. 551–560, 2006. 23

[60] M. Quirini, A. Menciassi, S. Scapellato, P. Dario, F. Rieber, C.-N. Ho, S. Schostek, and M. O. Schurr, "Feasibility proof of a legged locomotion capsule for the GI tract," *Gastrointestinal endoscopy*, vol. 67, no. 7, pp. 1153–1158, 2008. 23

[61] M. Quirini, A. Menciassi, S. Scapellato, C. Stefanini, and P. Dario, "Design and fabrication of a motor legged capsule for the active exploration of the gastrointestinal tract," *IEEE/ASME transactions on mechatronics*, vol. 13, no. 2, pp. 169–179, 2008. 23

[62] P. R. Slawinski, K. L. Obstein, and P. Valdastri, "Capsule endoscopy of the future: What's on the horizon?," *World Journal of Gastroenterology: WJG*, vol. 21, no. 37, p. 10528, 2015. 23

[63] I. Rahman, N. A. Afzal, and P. Patel, "The role of magnetic assisted capsule endoscopy (MACE) to aid visualisation in the upper GI tract," *Computers in biology and medicine*, vol. 65, pp. 359–363, 2015. 23

[64] H.-L. Ching, M. F. Hale, and M. E. McAlindon, "Current and future role of magnetically assisted gastric capsule endoscopy in the upper gastrointestinal tract," *Therapeutic advances in gastroenterology*, vol. 9, no. 3, pp. 313–321, 2016. 23

[65] H. M. Kim, J. S. Choi, and J. H. Cho, "A pilot trial of ambulatory monitoring of gastric motility using a modified magnetic capsule endoscope,"

Journal of neurogastroenterology and motility, vol. 20, no. 2, p. 261, 2014. 24

[66] G. Ciuti, P. Valdastri, A. Menciassi, and P. Dario, "Robotic magnetic steering and locomotion of capsule endoscope for diagnostic and surgical endoluminal procedures," *Robotica*, vol. 28, no. 2, pp. 199–207, 2010. 24

[67] J. Rahmer, C. Stehning, and B. Gleich, "Spatially selective remote magnetic actuation of identical helical micromachines," *Science Robotics*, vol. 2, no. 3, p. eaal2845, 2017. 24

[68] J.-F. Rey, H. Ogata, N. Hosoe, K. Ohtsuka, N. Ogata, K. Ikeda, H. Aihara, I. Pangtay, T. Hibi, and S. Kudo, "Feasibility of stomach exploration with a guided capsule endoscope," *Endoscopy*, vol. 42, no. 07, pp. 541–545, 2010. 24

[69] J.-F. Rey, H. Ogata, N. Hosoe, K. Ohtsuka, N. Ogata, K. Ikeda, H. Aihara, I. Pangtay, T. Hibi, and S.-E. Kudo, "Blinded nonrandomized comparative study of gastric examination with a magnetically guided capsule endoscope and standard videoendoscope," *Gastrointestinal endoscopy*, vol. 75, no. 2, pp. 373–381, 2012. 25

[70] Z. Liao, X.-D. Duan, L. Xin, L.-M. Bo, X.-H. Wang, G.-H. Xiao, L.-H. Hu, S.-L. Zhuang, and Z.-S. Li, "Feasibility and safety of magnetic-controlled capsule endoscopy system in examination of human stomach: a pilot study in healthy volunteers," *Journal of interventional gastroenterology*, vol. 2, no. 4, p. 155, 2012. 25

[71] K.-C. Kong, J. Cha, D. Jeon, and D.-i. D. Cho, "A rotational micro biopsy device for the capsule endoscope," in *Intelligent Robots and Systems, 2005.(IROS 2005). 2005 IEEE/RSJ International Conference on*, pp. 1839–1843, IEEE. 25

[72] M. Simi, G. Gerboni, A. Menciassi, and P. Valdastri, "Magnetic mechanism for wireless capsule biopsy," in *Proc. of ASME Design of Medical Devices Conference,(DMD2012), Minneapolis, MN, April*, pp. 10–12. 25

[73] T. D. Wang and J. Van Dam, "Optical biopsy: a new frontier in endoscopic detection and diagnosis," *Clinical gastroenterology and hepatology*, vol. 2, no. 9, pp. 744–753, 2004. 25

[74] H. Zhang, D. Morgan, G. Cecil, A. Burkholder, N. Ramocki, B. Scull, and P. K. Lund, "Biochromoendoscopy: molecular imaging with capsule endoscopy for detection of adenomas of the gi tract," *Gastrointestinal Endoscopy*, vol. 68, no. 3, pp. 520–527, 2008. 26

[75] Z. Jia, G. Yan, H. Liu, Z. Wang, P. Jiang, and Y. Shi, "The optimization of wireless power transmission: design and realization," *The International Journal of Medical Robotics and Computer Assisted Surgery*, vol. 8, no. 3, pp. 337–347, 2012. 26

[76] J. Burgner-Kahrs, D. C. Rucker, and H. Choset, "Continuum robots for medical applications: A survey," *IEEE Transactions on Robotics*, vol. 31, no. 6, pp. 1261–1280, 2015. 26, 53

[77] J. H. Crews and G. D. Buckner, "Design optimization of a shape memory alloy–actuated robotic catheter," *Journal of Intelligent Material Systems and Structures*, vol. 23, no. 5, pp. 545–562, 2012. 27

[78] K. Ikuta, Y. Matsuda, D. Yajima, and Y. Ota, "Pressure pulse drive: A control method for the precise bending of hydraulic active catheters," *IEEE/ASME Transactions on Mechatronics*, vol. 17, no. 5, pp. 876–883, 2012. 28

[79] L. Manfredi, E. Capoccia, G. Ciuti, and A. Cuschieri, "A Soft Pneumatic Inchworm Double balloon (SPID) for colonoscopy," *Scientific Reports*, vol. 9, no. 1, p. 11109, 2019. 28

[80] A. Zatopa, S. Walker, and Y. Menguc, "Fully Soft 3D-Printed Electroactive Fluidic Valve for Soft Hydraulic Robots," *Soft Robotics*, vol. 00, no. 00, p. soro.2017.0019, 2018. 28

[81] P. Rothemund, A. Ainla, L. Belding, D. J. Preston, S. Kurihara, Z. Suo, and G. M. Whitesides, "A soft , bistable valve for autonomous control of soft actuators," vol. 7986, no. March, pp. 1–11, 2018. 28

[82] G. Chen, M. T. Pham, and T. Redarce, "Sensor-based guidance control of a continuum robot for a semi-autonomous colonoscopy," *Robotics and autonomous systems*, vol. 57, no. 6, pp. 712–722, 2009. 28

[83] P. Valdastri, G. Ciuti, A. Verbeni, A. Menciassi, P. Dario, A. Arezzo, and M. Morino, "Magnetic air capsule robotic system: proof of concept

of a novel approach for painless colonoscopy," *Surgical endoscopy*, vol. 26, no. 5, pp. 1238–1246, 2012. 29

[84] J. C. Norton, P. R. Slawinski, H. S. Lay, J. W. Martin, B. F. Cox, G. Cummins, M. P. Y. Desmulliez, R. E. Clutton, K. L. Obstein, S. Cochran, and P. Valdastri, "Intelligent magnetic manipulation for gastrointestinal ultrasound," 2019. 29

[85] J. W. Martin, B. Scaglioni, J. C. Norton, V. Subramanian, A. Arezzo, K. L. Obstein, and P. Valdastri, "Enabling the future of colonoscopy with intelligent and autonomous magnetic manipulation," *Nature Machine Intelligence*, vol. 2, pp. 595–606, oct 2020. 29, 38, 93, 94

[86] P. Lloyd, A. Kafash Hoshiar, T. Da Veiga, A. Attanasio, N. Marahrens, J. H. Chandler, and P. Valdastri, "A learnt approach for the design of magnetically actuated shape forming soft tentacle robots," 2020. 29

[87] R. Stopforth, S. Davrajh, and K. Althoefer, "Low cost robotic endoscope design considerations," in *Pattern Recognition Association of South Africa and Robotics and Mechatronics International Conference (PRASA-RobMech), 2016*, pp. 1–6, IEEE. 29

[88] XENOCOR, "Xenoscope," *https://xenocor.com/press/*, 2017. 30

[89] EVOTECH-MED, "Evocam," *http://evotechmed.com/*, 2017. 30

[90] PrimeSight, "Endosheath," *https://www.laborie.com/*. 30

[91] IntroMedic, "Eg-scan," *https://www.intromedic.co.kr:550/eng/*, 2021. 30

[92] Ambu, "ascope," *https://www.ambu.co.uk/endoscopy/*, 2021. 30

[93] N. Garbin, L. Wang, J. H. Chandler, K. L. Obstein, N. Simaan, and P. Valdastri, "A disposable continuum endoscope using piston-driven parallel bellow actuator," in *2018 International Symposium on Medical Robotics (ISMR)*, pp. 1–6, mar 2018. 31, 75

[94] N. Garbin, L. Wang, J. H. Chandler, K. L. Obstein, N. Simaan, and P. Valdastri, "Dual-Continuum Design Approach for Intuitive and Low-Cost Upper Gastrointestinal Endoscopy," *IEEE Transactions on Biomedical Engineering*, vol. 66, no. 7, pp. 1963–1974, 2019. 31

[95] N. Garbin, A. P. Mamunes, D. Sohn, R. W. Hawkins, P. Valdastri, and K. L. Obstein, "Evaluation of a novel low-cost disposable endoscope for visual assessment of the esophagus and stomach in an ex-vivo phantom model.," *Endoscopy international open*, vol. 7, pp. E1175–E1183, sep 2019. 31

[96] M. Moshkowitz, Y. Hirsch, I. Carmel, T. Duvdevany, I. Fabian, E. P. Willenz, and J. Cohen, "A novel device for rapid cleaning of poorly prepared colons.," *Endoscopy*, vol. 42, pp. 834–836, oct 2010. 35

[97] D. Wang, X. Xie, G. Li, Z. Yin, and Z. Wang, "A lumen detection-based intestinal direction vector acquisition method for wireless endoscopy systems," *IEEE Transactions on Biomedical Engineering*, vol. 62, pp. 807–819, mar 2015. 38

[98] P. Jin, X. Ji, W. Kang, Y. Li, H. Liu, F. Ma, S. Ma, H. Hu, W. Li, and Y. Tian, "Artificial intelligence in gastric cancer: a systematic review," sep 2020. 38

[99] J. Y. Lee, J. Jeong, E. M. Song, C. Ha, H. J. Lee, J. E. Koo, D. H. Yang, N. Kim, and J. S. Byeon, "Real-time detection of colon polyps during colonoscopy using deep learning: systematic validation with four independent datasets," *Scientific Reports*, vol. 10, pp. 1–9, dec 2020. 38

[100] P. H. Niu, L. L. Zhao, H. L. Wu, D. B. Zhao, and Y. T. Chen, "Artificial intelligence in gastric cancer: Application and future perspectives," sep 2020. 38

[101] P. Brandao, O. Zisimopoulos, E. Mazomenos, G. Ciuti, J. Bernal, M. Visentini-Scarzanella, A. Menciassi, P. Dario, A. Koulaouzidis, A. Arezzo, D. J. Hawkes, and D. Stoyanov, "Towards a Computed-Aided Diagnosis System in Colonoscopy: Automatic Polyp Segmentation Using Convolution Neural Networks," *Journal of Medical Robotics Research*, vol. 03, p. 1840002, jun 2018. 38

[102] Y. Ikenoyama, T. Hirasawa, M. Ishioka, K. Namikawa, S. Yoshimizu, Y. Horiuchi, A. Ishiyama, T. Yoshio, T. Tsuchida, Y. Takeuchi, S. Shichijo, N. Katayama, J. Fujisaki, and T. Tada, "Detecting early gastric cancer: Comparison between the diagnostic ability of convolutional neural networks and endoscopists," *Digestive Endoscopy*, vol. 33, pp. 141–150, jan 2021. 38

[103] H. Luo, G. Xu, C. Li, L. He, L. Luo, Z. Wang, B. Jing, Y. Deng, Y. Jin, Y. Li, B. Li, W. Tan, C. He, S. R. Seeruttun, Q. Wu, J. Huang, D. wang Huang, B. Chen, S. bin Lin, Q. ming Chen, C. ming Yuan, H. xin Chen, H. ying Pu, F. Zhou, Y. He, and R. hua Xu, "Real-time artificial intelligence for detection of upper gastrointestinal cancer by endoscopy: a multicentre, case-control, diagnostic study," *The Lancet Oncology*, vol. 20, pp. 1645–1654, dec 2019. 38

[104] S. Calò, J. H. Chandler, F. Campisano, K. L. Obstein, and P. Valdastri, "A Compression Valve for Sanitary Control of Fluid Driven Actuators," *IEEE/ASME Transactions on Mechatronics*, vol. 25, pp. 1005–1015, apr 2019. 53, 76

[105] T. George Thuruthel, Y. Ansari, E. Falotico, and C. Laschi, "Control Strategies for Soft Robotic Manipulators: A Survey," *Soft Robotics*, no. January, p. soro.2017.0007, 2018. 53, 75

[106] B. S. Homberg, R. K. Katzschmann, M. R. Dogar, and D. Rus, "Haptic Identification of Objects using a Modular Soft Robotic Gripper," *2015 Ieee/Rsj International Conference on Intelligent Robots and Systems*, pp. 1698–1705, 2015. 53

[107] E. W. Hawkes, L. H. Blumenschein, J. D. Greer, and A. M. Okamura, "A soft robot that navigates its environment through growth," *Science Robotics*, vol. 2, no. 8, p. eaan3028, 2017. 53

[108] R. F. Shepherd, F. Ilievski, W. Choi, S. A. Morin, A. A. Stokes, A. D. Mazzeo, X. Chen, M. Wang, and G. M. Whitesides, "Multigait soft robot," *Proceedings of the National Academy of Sciences*, vol. 108, no. 51, pp. 20400–20403, 2011. 53

[109] K. C. Galloway, K. P. Becker, B. Phillips, J. Kirby, S. Licht, D. Tchernov, R. J. Wood, and D. F. Gruber, "Soft robotic grippers for biological sampling on deep reefs," *Soft Robotics*, vol. 3, no. 1, pp. 23–33, 2016. PMID: 27625917. 53

[110] M. Cianchetti, T. Ranzani, G. Gerboni, T. Nanayakkara, K. Althoefer, P. Dasgupta, and A. Menciassi, "Soft Robotics Technologies to Address Shortcomings in Today's Minimally Invasive Surgery: The STIFF-FLOP Approach," *Soft Robotics*, vol. 1, no. 2, pp. 122–131, 2014. 53

[111] E. T. Roche, M. A. Horvath, I. Wamala, A. Alazmani, S. E. Song, W. Whyte, Z. Machaidze, N. V. Vasilyev, D. J. Mooney, F. A. Pigula, and C. J. Walsh, "Soft Robotic Sleeve Restores Heart Function," *Science Translational Medicine*, vol. 9, no. 373, p. eaaf3925, 2017. 53

[112] M. Wehner, Y. L. Park, C. Walsh, R. Nagpal, R. J. Wood, T. Moore, and E. Goldfield, "Experimental characterization of components for active soft orthotics," *Proceedings of the IEEE RAS and EMBS International Conference on Biomedical Robotics and Biomechatronics*, pp. 1586–1592, 2012. 53

[113] V. R. Muthusamy and A. S. Ross, "Sa1068 Economic Burden of Emergent Practices of Duodenoscopes Reprocessing and Surveillance: Balancing Risk- and Cost-Containment," *Gastrointestinal Endoscopy*, vol. 87, no. 6, Supplement, pp. AB167 – AB168, 2018. 54

[114] M. M. Schmauch, S. R. Mishra, B. A. Evans, O. D. Velev, and J. B. Tracy, "Chained Iron Microparticles for Directionally Controlled Actuation of Soft Robots," *ACS Applied Materials and Interfaces*, vol. 9, no. 13, pp. 11895–11901, 2017. 54

[115] K. W. Oh, R. Rong, and C. H. Ahn, "Miniaturization of pinch-type valves and pumps for practical micro total analysis system integration," *Journal of Micromechanics and Microengineering*, vol. 15, no. 12, pp. 2449–2455, 2005. 54

[116] G. J. Peek, K. Wong, C. Morrison, H. M. Killer, and R. K. Firmin, "Tubing failure during prolonged roller pump use: A laboratory study," *Perfusion*, vol. 14, no. 6, pp. 443–452, 1999. 54, 63

[117] M. Liermann, "Active Pneumatic Pulsation Damper for Peristaltic Pump Flow Loops," in *BATH/ASME 2016 Symposium on Fluid Power and Motion Control*, p. V001T01A005, ASME, sep 2016. 54

[118] NIH (The National Institute of Diabetes and Digestive and Kidney Diseases), "Upper GI Endoscopy." 72

[119] T. Hirasawa, K. Aoyama, T. Tanimoto, S. Ishihara, S. Shichijo, T. Ozawa, T. Ohnishi, M. Fujishiro, K. Matsuo, J. Fujisaki, and Others, "Application of artificial intelligence using a convolutional neural network for detecting gastric cancer in endoscopic images," *Gastric Cancer*, vol. 21, no. 4, pp. 653–660, 2018. 74

[120] P. R. Slawinski, A. Z. Taddese, K. B. Musto, K. L. Obstein, and P. Valdastri, "Autonomous Retroflexion of a Magnetic Flexible Endoscope," *IEEE Robotics and Automation Letters*, vol. 2, pp. 1352–1359, jul 2017. 75

[121] A. Attanasio, B. Scaglioni, M. Leonetti, A. F. Frangi, W. Cross, C. S. Biyani, and P. Valdastri, "Autonomous Tissue Retraction in Robotic Assisted Minimally Invasive Surgery - A Feasibility Study," *IEEE Robotics and Automation Letters*, vol. 5, pp. 6528–6535, oct 2020. 75, 93

[122] I. I. I. Robert J. Webster and B. A. Jones, "Design and Kinematic Modeling of Constant Curvature Continuum Robots: A Review," *The International Journal of Robotics Research*, vol. 29, no. 13, pp. 1661–1683, 2010. 75

[123] A. D. Marchese, K. Komorowski, C. D. Onal, and D. Rus, "Design and control of a soft and continuously deformable 2D robotic manipulation system," pp. 2189–2196, 2014. 75

[124] T. M. Bieze, F. Largilliere, A. Kruszewski, Z. Zhang, R. Merzouki, and C. Duriez, "Finite Element Method-Based Kinematics and Closed-Loop Control of Soft, Continuum Manipulators," *Soft Robotics*, vol. 00, no. 00, p. soro.2017.0079, 2018. 75

[125] M. C. Yip and D. B. Camarillo, "Model-less feedback control of continuum manipulators in constrained environments," *IEEE Transactions on Robotics*, vol. 30, no. 4, pp. 880–889, 2014. 75

[126] M. Giorelli, F. Renda, G. Ferri, and C. Laschi, "A feed-forward neural network learning the inverse kinetics of a soft cable-driven manipulator moving in three-dimensional space," pp. 5033–5039, 2013. 75

[127] M. Giorelli, F. Renda, M. Calisti, A. Arienti, G. Ferri, and C. Laschi, "Neural Network and Jacobian Method for Solving the Inverse Statics of a Cable-Driven Soft Arm With Nonconstant Curvature," *IEEE Transactions on Robotics*, vol. 31, pp. 823–834, aug 2015. 75

[128] M. C. Yip and D. B. Camarillo, "Model-Less Hybrid Position/Force Control: A Minimalist Approach for Continuum Manipulators in Unknown, Constrained Environments," *IEEE Robotics and Automation Letters*, vol. 1, pp. 844–851, jul 2016. 75

[129] O. G. Grasa, E. Bernal, S. Casado, I. Gil, and J. M. M. Montiel, "Visual SLAM for hand-help monocular endoscope," *IEEE Trans. Medical Imaging*, vol. 33, no. 1, pp. 135–146, 2014. 76

[130] R. Mur-Artal, J. M. M. Montiel, and J. D. Tardos, "ORB-SLAM: A Versatile and Accurate Monocular SLAM System," *IEEE Transactions on Robotics*, vol. 31, pp. 1147–1163, oct 2015. 76, 116

[131] N. Mahmoud, I. Cirauqui, A. Hostettler, C. Doignon, L. Soler, J. Marescaux, and J. M. Montiel, "ORBSLAM-Based Endoscope Tracking and 3D Reconstruction," *Lecture Notes in Computer Science (including subseries Lecture Notes in Artificial Intelligence and Lecture Notes in Bioinformatics)*, vol. 10170 LNCS, pp. 72–83, 2017. 76, 116

[132] M. Turan, Y. Almalioglu, H. Araujo, E. Konukoglu, and M. Sitti, "A Non-Rigid Map Fusion-Based RGB-Depth SLAM Method for Endoscopic Capsule Robots," *International Journal of Intelligent Robotics and Applications*, vol. 1, no. 4, pp. 399–409, 2017. 76

[133] Z. Hawks, C. Frazelle, K. E. Green, and I. D. Walker, "Motion Planning for a Continuum Robotic Mobile Lamp: Defining and Navigating the Configuration Space," pp. 2559–2566, nov 2019. 78

[134] S. Leonard, K. L. Wu, Y. Kim, A. Krieger, and P. C. Kim, "Smart tissue anastomosis robot (STAR): A vision-guided robotics system for laparoscopic suturing," *IEEE Transactions on Biomedical Engineering*, vol. 61, no. 4, pp. 1305–1317, 2014. 93

[135] A. Krieger, J. Opfermann, and P. C. Kim, "Development and feasibility of a robotic laparoscopic clipping tool for wound closure and anastomosis," *Journal of Medical Devices, Transactions of the ASME*, vol. 12, p. 0110051, mar 2018. 93

[136] S. McKinley, A. Garg, S. Sen, D. V. Gealy, J. P. McKinley, Y. Jen, M. Guo, D. Boyd, and K. Goldberg, "An interchangeable surgical instrument system with application to supervised automation of multilateral tumor resection," in *IEEE International Conference on Automation Science and Engineering*, vol. 2016-November, pp. 821–826, IEEE Computer Society, nov 2016. 94

[137] L. Fichera, N. P. Dillon, D. Zhang, I. S. Godage, M. A. Siebold, B. I. Hartley, J. H. Noble, P. T. Russell, R. F. Labadie, and R. J. Webster, "Through the Eustachian Tube and Beyond: A New Miniature Robotic Endoscope to See into the Middle Ear," *IEEE Robotics and Automation Letters*, vol. 2, pp. 1488–1494, jul 2017. 94

[138] A. Bajo and N. Simaan, "Kinematics-based detection and localization of contacts along multisegment continuum robots," *IEEE Transactions on Robotics*, vol. 28, pp. 291–302, apr 2012. 94, 95

[139] F. Campisano, A. A. Remirez, C. A. Landewee, S. Calo, K. L. Obstein, R. J. Webster, and P. Valdastri, "Teleoperation and Contact Detection of a Waterjet-Actuated Soft Continuum Manipulator for Low-Cost Gastroscopy," *IEEE Robotics and Automation Letters*, vol. 5, pp. 6427–6434, oct 2020. 94, 110

[140] L. G. Torres, A. Kuntz, H. B. Gilbert, P. J. Swaney, R. J. Hendrick, R. J. Webster, and R. Alterovitz, "A motion planning approach to automatic obstacle avoidance during concentric tube robot teleoperation," pp. 2361–2367, may 2015. 95, 116

[141] K. Wu, L. Wu, and H. Ren, "Motion planning of continuum tubular robots based on centerlines extracted from statistical atlas," in *2015 IEEE/RSJ International Conference on Intelligent Robots and Systems (IROS)*, pp. 5512–5517, 2015. 95

[142] M. Pinzi, S. Galvan, and F. R. y Baena, "The Adaptive Hermite Fractal Tree (AHFT): a novel surgical 3D path planning approach with curvature and heading constraints," *International journal of computer assisted radiology and surgery*, vol. 14, no. 4, pp. 659–670, 2019. 95

[143] A. Kuntz, A. W. Mahoney, N. E. Peckman, P. L. Anderson, F. Maldonado, R. J. Webster, and R. Alterovitz, "Motion planning for continuum reconfigurable incisionless surgical parallel robots," in *2017 IEEE/RSJ International Conference on Intelligent Robots and Systems (IROS)*, pp. 6463–6469, 2017. 95

[144] F. Campisano, A. A. Remirez, S. Calò, J. H. Chandler, K. L. Obstein, R. J. Webster, and P. Valdastri, "Online Disturbance Estimation for Improving Kinematic Accuracy in Continuum Manipulators," *IEEE Robotics and Automation Letters*, vol. 5, pp. 2642–2649, apr 2020. 95, 115

[145] L. Qiu and H. Ren, "Endoscope Navigation and 3D Reconstruction of Oral Cavity by Visual SLAM with Mitigated Data Scarcity," pp. 2278–22787, 2018. 116